2014

Manipulating graphene's lattice to create pseudovector potentials, discover anomalous friction, and measure strain dependent thermal conductivity

https://hdl.handle.net/2144/15101

BOSTON UNIVERSITY

GRADUATE SCHOOL OF ARTS AND SCIENCES

Dissertation

MANIPULATING GRAPHENE'S LATTICE TO CREATE PSEUDOVECTOR POTENTIALS, DISCOVER ANOMALOUS FRICTION, AND MEASURE STRAIN DEPENDENT THERMAL CONDUCTIVITY

by

ALEXANDER LUKE KITT

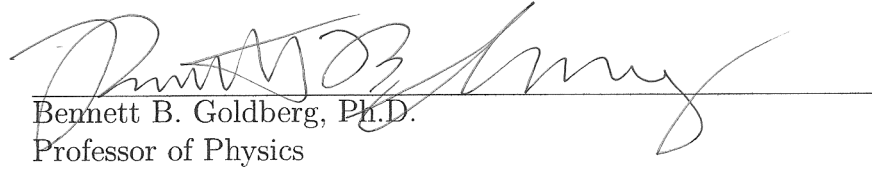B.S. and B.A., University at Buffalo, 2008
M.A., Boston University, 2012

Submitted in partial fulfillment of the

requirements for the degree of

Doctor of Philosophy

2014

Approved by

First Reader

Bennett B. Goldberg, Ph.D.
Professor of Physics

Second Reader

Anna K. Swan, Ph.D.
Associate Professor of Electrical and Computer Engineering,
Physics, Materials Science and Engineering, and Photonics

Acknowledgments

With deep gratitude I thank my advisors Bennett Goldberg and Anna Swan for crafting me into the physicist I am today. Special thanks to Bennett for giving me the freedom to follow my ideas, and to Anna for having the patience to listen to my latest experimental foible.

Many thanks to my many collaborators. Specifically I would like to thank the reputable graphene strain theorists Harold Park, Zenan Qi and Vitor Pereira, the brilliant Kekulé theorists Claudio Chamon and Tom Iadecola, the masters of helium scattering Michael El-Batanouny and Colin Howard, and the graphene growth gurus at UT Austin Rod Ruoff, Richard Piner, and Ji Won Suk. Additional thanks go to my lab mates Sebastian Remi, Xuanye Wang, and Jason Christopher and my cohort at BU, especially Alan Gabel, Elsa Abreu, John Ogren, Cory Fantasia, and Kang Liu.

Thanks to the folks at SIF, principally Heitor Mourato, Bob Fazio, and Joe Volho, who routinely made substance out of my imagination. Special thanks to the late Bob Kingsland, a great teacher who was always able to make me feel at home and at ease-onwards and upwards.

I would like to thank my parents and most loyal fans, Anne Mercier and Greg Kitt, for giving me the traits which carried me through graduate school: An expectation of myself and the confidence to work with my hands. I would also like to thank my wife's parents, Dede and Stan Colwell, for their acceptance and encouragement.

Most importantly I would like to thank my wife, Jess, for helping me get through my N+1 failures. I could never have done this without her unwavering love and support.

MANIPULATING GRAPHENE'S LATTICE TO CREATE PSEUDOVECTOR POTENTIALS, DISCOVER ANOMALOUS FRICTION, AND MEASURE STRAIN DEPENDENT THERMAL CONDUCTIVITY

(Order No.   )

ALEXANDER KITT

Boston University Graduate School of Arts and Sciences, 2014

Major Professor: Bennett B. Goldberg, Professor of Physics

ABSTRACT

Graphene is a single atomic sheet of graphite that exhibits a diverse range of unique properties. The electrons in intrinsic graphene behave like relativistic Dirac fermions; graphene has a record high Young's modulus but extremely low bending rigidity; and suspended graphene exhibits very high thermal conductivity. These properties are made more intriguing because with a thickness of only a single atomic layer, graphene is both especially affected by its environment and readily manipulated. In this dissertation the interaction between graphene and its environment as well as the exciting new physics realized by manipulating graphene's lattice are investigated.

Lattice manipulations in the form of strain cause alterations in graphene's electrical dispersion mathematically analogous to the vector potential associated with a magnetic field. We complete the standard description of the strain-induced vector potential by explicitly including the lattice deformations and find new, leading order terms. Additionally, a strain engineered device with large, localized, plasmonically enhanced pseudomagnetic fields is proposed to couple light to pseudomagnetic fields.

Accurate strain engineering requires a complete understanding of the interactions between a two dimensional material and its environment, particularly the adhesion and friction between graphene and its supporting substrate. We measure the load

dependent sliding friction between mono-, bi-, and trilayer graphene and the commonly used SiO_2 substrate by analyzing Raman spectra of circular, graphene sealed microchambers under variable external pressure. We find that the sliding friction for trilayer graphene behaves normally, scaling with the applied load, whereas the friction for monolayer and bilayer graphene is anomalous, scaling with the inverse of the strain in the graphene.

Both strain and graphene's environment are expected to affect the quadratically dispersed out of plane acoustic phonon. Although this phonon is believed to provide the majority of graphene's very high thermal conductivity, its contributions have never been isolated. By measuring strain and pressure dependent thermal conductivity, we gain insight into the mechanism of graphene's thermal transport.

Contents

List of Tables

List of Figures

List of Abbreviations

AC	Alternating Current
AFM	Atomic Force Microscopy
BZ	First Brillouin Zone
DC	Direct Current
EMI	Electro Magnetic Interference
FLG	Few Layer Graphene
K2400	Keithley 2400 source meter
SEM	Scanning Electron Microscopy
ZA	Out of Plane Accoustic Phonons

Chapter 1

Introduction

This thesis is a study of how the wonder material graphene responds when its lattice is manipulated. Graphene is a single atomic layer of graphite with lateral dimensions orders of magnitude larger than its thickness. In fact, the sheets of graphene used in this thesis have a length to thickness ratio on the order of 10^6, similar to that of a bed sheet. Graphene was first discovered in 1969 when J.W. Mays identified graphene's low energy electron diffraction pattern (May, 1969). However, it was not until Noveselov, Geim and co-workers demonstrated both an easy method of making graphene and an easy way of seeing graphene (Novoselov et al., 2004) that the field exploded in 2004. According to Web of Science, since 2004 there have been more than 29,000 academic publications with graphene in their title (Web of Sciecne, 2013).

This onslaught of research is a result of several factors. First, graphene does not require any special facilities to fabricate. All one needs is scotch tape, silicon wafers with thermal oxide, a microscope, and a little bit of patience. Second, graphene is, for the most part, theoretically accessible. The majority of its properties can be understood using a simple tight binding model (Castro Neto et al., 2009). But most importantly, graphene has been shown to be of great scientific interest. It has a range of exotic properties stemming from the relativistic nature of its electrons including the anomalous quantum hall effect (Zhang et al., 2005) and Klein tunneling (Young

and Kim, 2009). It also has impressive material properties including a record Youngs modulus (Lee et al., 2008), very high thermal conductivity (Faugeras et al., 2010), and impermeability to gases (Bunch et al., 2008).

These properties are made more intriguing because with a thickness of only one atomic layer, graphene is uncommonly affected by its environment. This allows for graphene's atomic lattice to be manipulated and its amazing properties to be altered. The focus of this thesis is on how graphene's electrical, mechanical, and thermal properties are altered when its lattice is manipulated. In Chapter 2 the tight binding description of intrinsic graphene is reviewed. In Chapter 3 this tight binding model is generalized to include long wavelength strains and the resulting pseudovector potentials and pseudomagnetic fields are discussed. The generation of these strain fields require that the interactions between graphene and its underlying bulk substrate are understood. Chapter 4 describes the measurement of the anomalous macroscopic sliding friction between graphene and a SiO_2 substrate. In Chapter 5 it is shown that the same experimentally geometry used to study friction can be used to study the mechanism behind graphene's very high thermal conductivity. Finally, in Chapter 6 the prospects of measuring the bandgap induced by a phonon which causes small wavelength modifications of graphene's lattice are discussed.

Chapter 2

Unmodified band structure

Graphene's linear electronic dispersion was first investigated by Wallace (Wallace, 1947), fifty seven years before Geim, Novoselov and co-workers spurred graphene research forward with their method of mechanical exfoliation (Novoselov et al., 2004). Thirty seven years later Semenoff formalized the equivalence between the low energy electrons in graphene and relativistic Dirac-Weyl electrons (Semenoff, 1984). Remarkably, the fairly simple nearest neighbor tight binding approach used by these authors has accurately described the majority of the low energy physics in graphene. This chapter will follow in the spirit of these derivations but include additional emphasis to guide the discussions of the strain induced pseudovector potentials and the phonon induced Kekulé transition.

2.1 Graphene's lattice and Brillouin zone

In its unperturbed state the carbon atoms in the graphene lattice are arrayed in a hexagon as shown in Figure 2.1(a). Throughout this thesis the $\hat{x}$ direction will be oriented along the zigzag direction as shown. Since a hexagonal lattice is not a Bravais lattice, the lattice must be treated as a triangular Bravais lattice with a two atom bases. In Figure 2.1(a) the A sub-lattice is colored orange and the B sub-lattice is colored blue. The lattice is created by arraying the two atoms basis using the

(a)

(b)
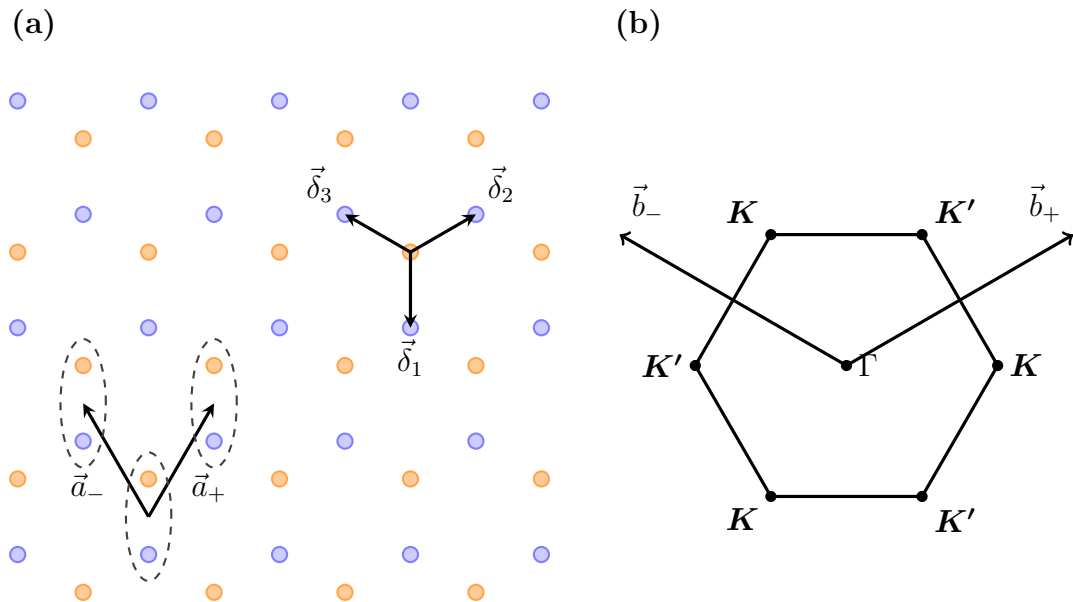
Figure 2.1: Geometry of intrinsic graphene. (a) Real space graphene lattice with the A sub-lattice in orange, the B sub-lattice in blue, nearest neighbor vectors ($\vec{\delta_1}$, $\vec{\delta_2}$, and $\vec{\delta_3}$) shown as arrows, and lattice vectors ($\vec{a}_+$ and $\vec{a}_-$) shown translating the two atom basis. (b) First Brillouin zone with labeled high symmetry points and reciprocal lattice vectors ($\vec{b}_+$ and $\vec{b}_-$).

primitive lattice vectors

$$\vec{a}_+ = \frac{\sqrt{3}a}{2}\left(+\hat{x} + \sqrt{3}\,\hat{y}\right)$$

$$\vec{a}_- = \frac{\sqrt{3}a}{2}\left(-\hat{x} + \sqrt{3}\,\hat{y}\right)\ ,$$

where $a = 1.4$ Å is the nearest neighbor distance. The three nearest neighbor vectors,

$$\vec{\delta_1} = -a\hat{y}$$

$$\vec{\delta_2} = \frac{a}{2}\left(+\sqrt{3}\,\hat{x} + \hat{y}\right)$$

$$\vec{\delta_3} = \frac{a}{2}\left(-\sqrt{3}\,\hat{x} + \hat{y}\right)\ ,$$

connect each atom in the A sub-lattice to its three nearest neighbors in the B sub-lattice.

Graphene's reciprocal lattice is shown in Figure 2.1(b). The primitive reciprocal lattice vectors,

$$b_+ = \frac{2\pi}{3}\left(+\sqrt{3}\,\hat{x} + \hat{y}\right)$$

$$b_- = \frac{2\pi}{3}\left(-\sqrt{3}\,\hat{x} + \hat{y}\right)\ ,$$

create the hexagonal first Brillouin zone (BZ). The hexagon is rotated 30 degrees relative to the real space hexagonal lattice. The Γ point is at the center of the Brillouin zone while the $\boldsymbol{K}$ and $\boldsymbol{K'}$ are at the corners. Only 2 of the 6 corners of the hexagon are unique, the others can be connected by reciprocal lattice vectors. The

two unique corners are referred to as $\boldsymbol{K}$ and $\boldsymbol{K'}$ are positioned at

$$\boldsymbol{K} = -\boldsymbol{K'} = \frac{4\pi}{3\sqrt{3}a}\hat{x}$$

$$\boldsymbol{K} = -\boldsymbol{K'} = \frac{2\pi}{3\sqrt{3}a}\left(-1\ \hat{x} + \sqrt{3}\hat{y}\right)$$

$$\boldsymbol{K} = -\boldsymbol{K'} = \frac{2\pi}{3\sqrt{3}a}\left(-1\ \hat{x} - \sqrt{3}\hat{y}\right)\ .$$

For simplicity we will often work with the first pair.

In later sections this discussion will be expanded to take into account strain and phonons which modify the graphene lattice. In both cases the changes in graphene's electronic dispersion are directly linked to geometric distortions.

2.2   Tight binding motivation

The tight binding formalism is used universally in this work. As such, it will be briefly motivated here. Afterward, the nearest neighbor tight binding formalism will be applied to graphene.

In second quantization the total electronic energy in the system is written as

$$H = \sum_{\vec{k}} c_{\vec{k}}^{\dagger} c_{\vec{k}} \epsilon_{\vec{k}}\ ,$$

where $c_{\vec{k}}^{\dagger}$ and $c_{\vec{k}}$ are the creation and annihilation operators for an electron with wavevector $\vec{k}$ and energy $\epsilon_{\vec{k}}$. The product $c_{\vec{k}}^{\dagger}c_{\vec{k}}$ is the number operator which counts the number of electrons with the given wavevector. Thus, the energy is found by simply summing the energy of each electron.

When the atomic wave functions of the atoms in the material do not overlap considerably it is reasonable to work with real space creation and annihilation operators.

These operators create or annihilate electrons at specific lattice points. The reciprocal space operators are related to the real space operators through a Fourier transform

$$c_{\vec{k}}^{\dagger} = \frac{1}{\sqrt{N}} \sum_{\vec{R}_i} e^{i\vec{k}\cdot\vec{R}_i} c_i^{\dagger}$$

$$c_{\vec{k}} = \frac{1}{\sqrt{N}} \sum_{\vec{R}_j} e^{-i\vec{k}\cdot\vec{R}_j} c_j \ ,$$

where the sum is over the lattice vectors. This Fourier transform can only eliminate spatial dependencies with the periodicity of the lattice. As such, if there are more than one atom per unit cell distinct creation and annihilation operators must be used for each atom in the basis.

Applying the Fourier transform to the systems Hamiltonian yields the tight binding Hamiltonian

$$H = -\sum_{\vec{R}_i, \vec{R}_j} (-) \sum_{\vec{k}} \frac{1}{N} e^{i\vec{k}\cdot(\vec{R}_i - \vec{R}_j)} \epsilon_{\vec{k}} c_i^{\dagger} c_j$$

$$\approx -\sum_{<i,j>} t_{i,j} c_i^{\dagger} c_j + \text{H.C} \ .$$

By limiting the sums to the $< i, j >$ nearest neighbor pairs we are limiting ourselves to a nearest neighbor tight binding formalism. The hopping energy, $t_{i,j} = -\sum_{\vec{k}} \frac{1}{N} e^{i\vec{k}\cdot(\vec{R}_i - \vec{R}_j)} \epsilon_{\vec{k}}$, is the energy associated with removing an electron from atom j and putting it on atom i. It is usually determined empirically or calculated by matching the tight binding model to other more powerful methods such as density functional theory. In graphene, it is around 2.8 eV (Castro Neto et al., 2009).

By using real space creation and annihilation operators the reciprocal space Hamiltonian has been recast into real space. As will be shown for graphene, this proves to be a powerful starting point.

2.3   Tight binding in graphene

2.3.1   Nearest neighbor tight binding

The physics relevant for this work is captured by the nearest neighbor tight binding formalism. In graphene, when an electron hops between nearest neighbor it changes sub-lattice. This is reflected in the nearest neighbor tight binding Hamiltonian,

$$H = -t_0 \sum_{<i,j>} (a_i^\dagger b_j + \text{H.C.}) \ . \tag{2.1}$$

Here the hopping energy, t_0, gives the energy required to remove an electron from the jth atom in the B sub-lattice using the B sub-lattice annihilation operator, b_j, and put that electron on it nearest neighbor, the ith atom in the A sub-lattice using the A sub-lattice creation operator, a_i. The hopping from the A sub-lattice back to the B sub-lattice is taken into account by the the Hermitian conjugate, H.C..

The Hamiltonian is simplified by writing the creation and annihilation operators in Fourier space using a Fourier expansion. There is some freedom in choosing the phase factors in the Fourier expansion. The operators can be expanded around the atomic positions or, alternatively, they can be expanded around the position of the basis occupied by the atom. Both approaches yield the same result if one is consistent (Bena and Montambaux, 2009). Throughout this thesis we will expand about the atomic basis. This will make the correspondence with the Dirac-Weyl equation more clear. The expanded operators are

$$a_i^\dagger = \frac{1}{\sqrt{N}} \sum_{\vec{k}} e^{i\vec{k}\cdot\vec{R}_i} a_{\vec{k}}^\dagger$$

$$b_j = \frac{1}{\sqrt{N}} \sum_{\vec{k'}} e^{-i\vec{k'}\cdot\vec{R}_j} b_{\vec{k'}} \ , \tag{2.2}$$

where R_i and R_j are the position of the ith and jth atomic basis respectfully. The nearest neighbor is either in the same atomic basis or in one of the neighboring atomic bases. Thus, $\vec{R}_j$ is restricted to $\vec{R}_j \in \{\vec{R}_i, \vec{R}_i + \vec{a}_+, \vec{R}_i + \vec{a}_-\}$ and the difference $\vec{\Delta}_j = \vec{R}_j - \vec{R}_i$ is independent of i. In reciprocal space the Hamiltonian becomes

$$
\begin{aligned}
H &= -t_0 \frac{1}{N} \sum_{\vec{k},\vec{k}'} \sum_i \sum_j \left(e^{i(\vec{k}-\vec{k}')\cdot\vec{R}_i} e^{-i\vec{k}'\cdot\vec{\Delta}_j} a_{\vec{k}}^\dagger b_{\vec{k}'} + \text{H.C.} \right) \\
&= -t_0 \frac{1}{N} \sum_{\vec{k},\vec{k}'} \sum_j \left(N\delta_{\vec{k},\vec{k}'}\, e^{-i\vec{k}'\cdot\vec{\Delta}_j} a_{\vec{k}}^\dagger b_{\vec{k}'} + \text{H.C.} \right) \\
&= -t_0 \sum_{\vec{k}} \left(\sum_j e^{-i\vec{k}\cdot\vec{\Delta}_j} a_{\vec{k}}^\dagger b_{\vec{k}} + \text{H.C.} \right) ,
\end{aligned}
\tag{2.3}
$$

where $\delta_{\vec{k},\vec{k}'}$ is the Kronecker delta function. In matrix notation this reads

$$
H = \sum_{\vec{k}} \left(\begin{array}{cc} a_{\vec{k}}^\dagger & b_{\vec{k}}^\dagger \end{array} \right) \left(\begin{array}{cc} 0 & -t_0 \sum_j e^{-i\vec{k}\cdot\vec{\Delta}_j} \\ -t_0 \sum_j e^{-i\vec{k}\cdot\vec{\Delta}_j} & 0 \end{array} \right) \left(\begin{array}{c} a_{\vec{k}} \\ b_{\vec{k}} \end{array} \right) .
\tag{2.4}
$$

The two atom basis yields a two by two matrix which will give two energy bands.

A straightforward calculation provides the electron dispersion,

$$
E(\vec{k}) = \pm t_0 |h(\vec{k})| = t_0 \sqrt{1 + 4\cos^2\left(\frac{\sqrt{3}}{2}ak_x\right) + 4\cos\left(\frac{\sqrt{3}}{2}ak_x\right)\cos\left(\frac{3}{2}ak_y\right)} ,
$$

which is plotted in Figure 2.2. As shown, the two energy bands touch at the corners of the Brillouin zone. For pristine graphene there is one electron per carbon atom leaving the low energy band completely filled and the high energy band empty. The points where the bands meet are referred to as the Dirac points or as the charge neutrality points. The Fermi energy can be shifted by charge transfer from contaminates or it can be purposely modified by adding or removing charges through capacitive coupling.

The resulting shifts in Fermi energy are relatively small and, thus, the low energy excitations happen in a narrow energy window around these points. This happens to be the energy window for which the nearest neighbor tight binding approach is most accurate. A higher order model is required to account for things such as trigonal warping which alter the dispersion at higher energies.

2.3.2 Low energy approximation

The two points of convergence between the high and low energy bands are referred to as the Dirac points because of the characteristic energy dispersion in their vicinity. This interesting low energy physics is best captured by expanding the Hamiltonian in Equation 2.4 about these points. The wavevectors are approximated as $\vec{k} = \boldsymbol{K} + \vec{q}$ and $\vec{k} = \boldsymbol{K'} + \vec{q}$. For small qa the sum in Equation 2.4 is approximately

$$
\sum_j e^{-i\vec{k}\cdot\vec{\Delta}_j} =
$$

$$
\boldsymbol{K}: \; \simeq \sum_j (1 - i\vec{q}\cdot\vec{\Delta}_j)e^{-i\boldsymbol{K}\cdot\vec{\Delta}_j}
$$

$$
= -\frac{3}{2}a\,(q_x - iq_y)
$$

$$
\boldsymbol{K'}: \; \simeq \sum_j (1 - i\vec{q}\cdot\vec{\Delta}_j)e^{-i\boldsymbol{K'}\cdot\vec{\Delta}_j}
$$

$$
= -\frac{3}{2}a\,(-q_x - iq_y) \; . \tag{2.5}
$$

These expansions are independent of which of the three identical $\boldsymbol{K}$ or $\boldsymbol{K'}$ points are selected. The approximate low energy Hamiltonians near the $\boldsymbol{K}$ and $\boldsymbol{K'}$ points can
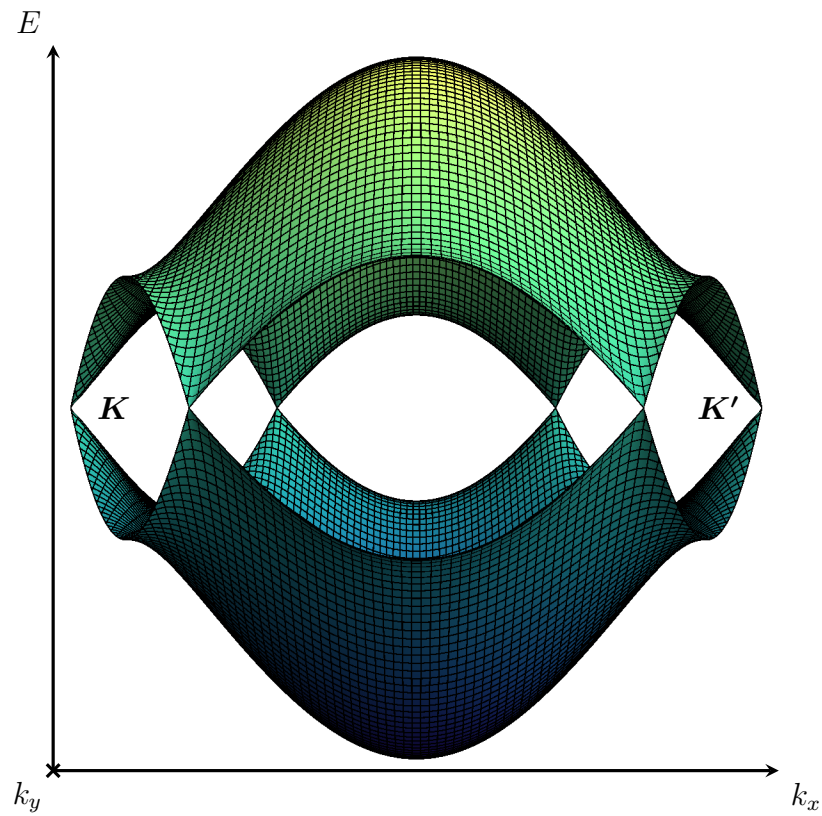
Figure 2.2: The electronic dispersion of intrinsic graphene in the BZ calculated with a nearest neighbor tight binding model. The two energy bands meet at the **K** and **K′** points.

be combined into a single Hamiltonian

$$H = \hbar v_f \sum_{\vec{q}, \vec{q}} \psi^\dagger \begin{pmatrix} 0 & q_x - iq_y & 0 & 0 \\ q_x + iq_y & 0 & 0 & 0 \\ 0 & 0 & 0 & -q_x + iq_y \\ 0 & 0 & -q_x - iq_y & 0 \end{pmatrix} \psi$$

$$H = \sum_{\vec{q}, \vec{q}} \psi^\dagger \begin{pmatrix} v_f \vec{p} \cdot \vec{\sigma} & 0 \\ 0 & -v_f \vec{p} \cdot \vec{\sigma} \end{pmatrix} \psi \ , \tag{2.6}$$

where

$$\psi^\dagger = (a_{\vec{q}}^\dagger, b_{\vec{q}}^\dagger, b_{\vec{q}}^\dagger, a_{\vec{q}}^\dagger) \tag{2.7}$$

is the combined wave function, $\vec{\sigma} = \begin{pmatrix} 0 & 1 \\ 1 & 0 \end{pmatrix} \hat{x} + \begin{pmatrix} 0 & -i \\ i & 0 \end{pmatrix} \hat{y}$ is the vector of Pauli matrices, and v_f is the Fermi velocity given by $\frac{3}{2}\frac{at}{\hbar} \sim .9 \times 10^6 \ m/s$. In order to express the Hamiltonian near the $\boldsymbol{K'}$ point in terms of Pauli matrices, the order of the second pair of raising and lowering operators in ψ had to be switched. The approximate low energy Hamiltonian will be central for the discussion of electron physics in manipulated graphene.

At both $\boldsymbol{K}$ and $\boldsymbol{K'}$ the low energy electronic dispersion is identical

$$E = \pm \hbar v_f |\vec{q}| \ .$$

This linear canonical energy dispersion is reminiscent of the linear dispersion exhibited by photons.

The density of electronic states can be calculated from the low energy dispersion. Taking account the two fold spin and two fold valley degeneracy, the density of states

is

$$\rho(\epsilon) = \frac{2}{\pi} \left(\frac{\hbar v_f}{L} \right)^2 \epsilon \,, \tag{2.8}$$

where L^2 is the area of the graphene and ϵ is the energy measured from the charge neutrality point. The density of states at a given energy goes as the circumference of the Dirac cone resulting in a linear energy dependence.

2.4 Dirac-Weyl electrons

Graphene's linear electrical dispersion is peculiar. According to the usual, non-relativistic expression for the effective mass of an electron in an electric field, $m^* = \frac{\hbar^2}{\left(\frac{d^2 E}{dk^2} \right)}$ (Kittel, 2005), the electrons in graphene have an infinite effective mass. In a classical sense, this interpretation makes sense. The electron's group velocity, $d\omega/dk$, is independent of momentum, and thus, as if it had an infinite mass, an electron's velocity cannot be changed by applying a force. However, a relativistic interpretation is more enlightening. In this scenario, the electrons are treated as massless relativist particles moving at the systems-effective light speed. Like a photon, these electrons cannot be accelerated. This analogy is deeper than the classical analogy. In 1984 Semenoff demonstrated the exact correspondence between the low energy nearest neighbor tight binding Hamiltonian of graphene and the two dimensional Dirac-Weyl Hamiltonian which governs massless, relativistic, spin 1/2, Fermions (Semenoff, 1984). In this section we will briefly discuss this correspondence.

The Hamiltonian of relativistic, spin 1/2, fermions is known as the Dirac equation. This matrix equation is covariant, obeys the relativistic energy expression, and is first order in time. The only difference between the Dirac equation for massless particles

in two spatial dimensions,

$$H = \begin{pmatrix} c\vec{p} \cdot \vec{\sigma} & 0 \\ 0 & -c\vec{p} \cdot \vec{\sigma} \end{pmatrix} , \qquad (2.9)$$

and the Hamiltonian governing graphene (Equation 2.6) is the speed of light for the system. Thus, even though the Fermi velocity of the electrons in graphene is a factor of 300 slower than the speed of light, the electrons behave as relativistic massless particles.

The decoupled nature of both the Dirac equation and graphene's Hamiltonian can be interpreted from a high energy point of view. The wave function for these Hamiltonians can be written as the combination of two, two-element spinors

$$\psi = \begin{pmatrix} \chi_+ \\ \chi_- \end{pmatrix} .$$

Using these spinors and the relativistic dispersion, $E = \pm pc$, in Equation 2.9 gives Weyl's equations,

$$(1 \mp \vec{\sigma} \cdot \hat{p})\chi_+ = 0$$

$$(1 \pm \vec{\sigma} \cdot \hat{p})\chi_- = 0 ,$$

where $\hat{p}$ is the unit vector in the direction of the momentum. In this form it is clear that the spinors are eigenvectors of the helicity operator, $\hat{h} = \frac{1}{2}\vec{\sigma} \cdot \hat{p}$, with eigenvectors $\hat{h}\chi_+ = \pm 1/2$ and $\hat{h}\chi_- = \mp 1/2$. The χ_+ spinor is said to be right handed; for particles with positive energy the spin and momentum are in the same direction whereas for particles with negative energy they are in the opposite direction. The χ_- spinor then

is left handed. Since the helicity operator commutes with the Hamiltonian, helicity is conserved in this system. Gottfried and Yan provide a more detailed discussion of the Dirac equation and its consequences (Gottfried and Yan, 2003).

In graphene, the elements of the spinors have additional geometric interpretations. Identifying graphene's wave function in Equation 2.7 with the relativistic spinors yields $\chi_+ \equiv \begin{pmatrix} \psi_A^{\boldsymbol{K}} \\ \psi_B^{\boldsymbol{K}} \end{pmatrix}$ and $\chi_- \equiv \begin{pmatrix} \psi_B^{\boldsymbol{K'}} \\ \psi_A^{\boldsymbol{K'}} \end{pmatrix}$. This indicates that the wave function for electrons at the $\boldsymbol{K}$ point are right handed and the electrons at the $\boldsymbol{K'}$ point are left handed. Further, the components of the spinors represent the probability amplitudes that an electron occupies the A or B sub-lattice. This connection between geometry and abstract spinors motivates the identification of sub-lattice with pseudospin.

Since graphene's Hamiltonian is identical to that of massless, relativistic, spin 1/2 Fermions, the electrons should exhibit the same odd properties that have been predicted by high energy physicists. These unique properties include the Klein paradox, which is the unimpeded penetration of relativistic particles through potential barriers (Young and Kim, 2009); Zitterbewegung, which is the jittery motion of relativistic particles (Castro Neto et al., 2009); and the anomalous quantum Hall effect, with a zero energy Landau level and square root magnetic field dependence (Novoselov et al., 2005; Zhang et al., 2005).

2.5   Summary

In this chapter we laid the theoretical framework for how we will treat the geometric alterations of graphene's lattice in Chapters 3 and 6. In each case we will first consider how the lattice described in Section 2.1 is altered by the perturbation. Then, following the calculation in Section 2.3, we will determine how graphene's electrical properties are effected. This framework is extremely powerful and will reveal exciting physics.

Chapter 3

Strain-induced vector potentials: Lattice-corrections and engineered pseudomagnetic fields

Graphene's most exciting physics may sit at the intersection between its mechanical and electrical properties where strain can cause electrons to behave as if they were in gigantic magnetic fields. This takes place because strain-induced distortions of the real space lattice can cause distortions of reciprocal space analogous to a magnetic field. In other words, strain shifts the crystal momentum of the Dirac points much like the the canonical momentum is shifted in the presence of a magnetic field. Graphene's extreme elasticity and two dimensional nature suggests that this effect can be creatively crafted to generate exotic physics.

A dazzling glimpse of the feasibility and potential of strain-engineered graphene (Pereira and Castro Neto, 2009; Guinea et al., 2010) has recently emerged with experiments reporting that certain strain profiles can induce Landau quantization and effective pseudomagnetic fields in excess of 300 T (Levy et al., 2010; Yan et al., 2012; Yeh et al., 2011). This strongly encourages the prospect of harnessing this unconventional interplay between electronic and mechanical properties to control electronic transport in graphene devices (Pereira and Castro Neto, 2009; Fogler et al., 2008).

This chapter starts by discussing the theory of the strain-induced vector potentials with an emphasis on the lattice-corrections first introduced by the author (Kitt et al.,

2012; Kitt et al., 2013a). This is followed by an examination of the importance of these lattice-corrections in different physical scenarios. Finally, methods of strain engineering graphene devices are examined with an emphasis on the over pressured hour glass shaped microchamber. This device cleverly takes advantage of plasmonics to enhance signals from high pseudomagnetic field regions.

3.1 Derivation of the pseudovector potentials

By distorting the graphene lattice, strain changes the electrical dispersion in three distinct ways (Pereira et al., 2009). Any finite strain shifts the Dirac points away from their original positions: The corners of the unstrained BZ. This shift in the Dirac point positions does not necessarily coincide with the strain-induced distortion of the BZ. Strain also continuously deforms the constant energy contours from isotropic circles into elliptical shapes. As a result, it is best to define two different Fermi velocities along the principal directions (Pereira et al., 2009; Pereira et al., 2010; Choi et al., 2010). Finally, for very large strains (probably near 20% where the tight-binding description is no longer reliable) the deformation is so strong that the two inequivalent Dirac points merge in a Lifshitz transition and the gapless and conical nature of the energy dispersion breaks down. All of these modifications are significant and happen concurrently.

From the theoretical as well as technical point of view, the effects of strain are frequently considered independently. One usually isolates the dominant effect for the physical observable of interest. For example, the strain-induced corrections to optical absorption arising from inter-band transitions are insensitive to the absolute position of the Dirac point in the BZ, but strongly depend on the velocity anisotropy (Pereira et al., 2010; Pellegrino et al., 2010). On the other hand, the local shift of the

Dirac point can hinder or completely suppress electronic propagation across regions of different strain states (Pereira and Castro Neto, 2009; Fogler et al., 2008). In a first approach the anisotropy is usually neglected in these situations(Fogler et al., 2008; Pereira and Castro Neto, 2009).

When the strain-induced shift of the Dirac points is considered independently of other strain effects, it can be thought of as a pseudovector potential (ichi Sasaki et al., 2005; Ando, 2006; Mañes, 2007; Castro Neto et al., 2009; Vozmediano et al., 2010). This can be done because of the peculiar form of the strain corrections to the electronic dispersion in graphene. Electrons in strained graphene are still governed by a Dirac equation, but one in which the strain modifications can be completely absorbed in the replacement $\hbar\vec{k} \to \hbar\vec{k} - e\vec{\mathcal{A}}$ where $\vec{\mathcal{A}}$ is the pseudovector potential. This matches the conventional minimal coupling scenario used to describe electronics in a magnetic field. The strain response maps onto the response to a magnetic field, and thus, electrons in strained graphene can behave as if they were in a magnetic field. The pseudovector potential is related to the shift in the Dirac point, $\Delta\vec{k}_D$, through $\Delta\vec{k}_D = -\frac{e}{\hbar}\vec{\mathcal{A}}$.

An omission in earlier work in the context of these pseudovector potentials is the explicit consideration of the deformation of the lattice when computing the position of the new Dirac points. Here this effect is included and its importance in determining the pseudovector potentials is shown. The inclusion of the lattice deformation yields new leading order terms in the strain-induced pseudovector potential which are different at the three inequivalent Dirac points. The discussion is restricted to planar deformations, and hence ignore effects that might arise in the presence of curvature (Castro Neto et al., 2009; Vozmediano et al., 2010). A detailed derivation of the pseudovector potential will be presented. It will begin with a geometric motivation of the strain-induced perturbations, continue by determining the strain dependencies

of these perturbations, and finish with the derivation of the pseudovector potentials.

3.1.1 Qualitative argument

The key elements underlying strain-induced pseudovector potentials are captured by generalizing the tight binding Hamiltonian discussed in Chapter 2 to the geometry of strained graphene. Figure 3.1 illustrates the changes in the lattice geometry due to strain by comparing the unstrained graphene lattice (top row) to the lattice under 20% uniaxial strain (bottom row). The large, 20% strain was chosen to better illustrate the deformation of the lattice and the BZ. Strain does not need to be this large; all of the effects discussed here are linear in strain. The method of calculating the distortion of the real and reciprocal space lattices is discussed in detail later in this chapter. Figure 3.1 will provide a qualitative geometric picture for how strain modifies the unstrained nearest neighbor tight binding approach discussed in Chapter 2.

The noticeable geometric distortion of both the nearest neighbor vectors and the lattice vectors corresponds to two distinct changes in the tight binding description. By making the lengths of the nearest neighbor vectors anisotropic, strain also makes the length-dependent nearest neighbor hopping amplitudes anisotropic. This introduces a bond dependent hopping energy into the the unstrained real space Hamiltonian (Equation 2.1) (Hasegawa et al., 2006),

$$H = - \sum_{<i,j>} \left(t_{i,j} a_i^\dagger b_j + t_{j,i} b_j^\dagger a_i \right) , \qquad (3.1)$$

where $t_{i,j}$ is the bond-specific hopping energy.

The second, and oft neglected alteration is a result of the distortion of the lattice vectors. Their alteration necessitates a change in the phase factors in the Fourier

(a)

$$\boldsymbol{\nabla u} = \begin{pmatrix} 0 & 0 \\ 0 & 0 \end{pmatrix}$$

$\vec{a}_-$ $\vec{a}_+$

$\vec{\delta}_3$ $\vec{\delta}_2$

$\vec{\delta}_1$

(b)

K K'

K' $\cdot\,\Gamma$ K

K K'

(c)

$$\boldsymbol{\nabla u} = \begin{pmatrix} -\nu\epsilon & 0 \\ 0 & \epsilon \end{pmatrix}$$

(d)

K_2 K_3'

K_1' $\cdot\,\Gamma$ K_1

K_3 K_2'
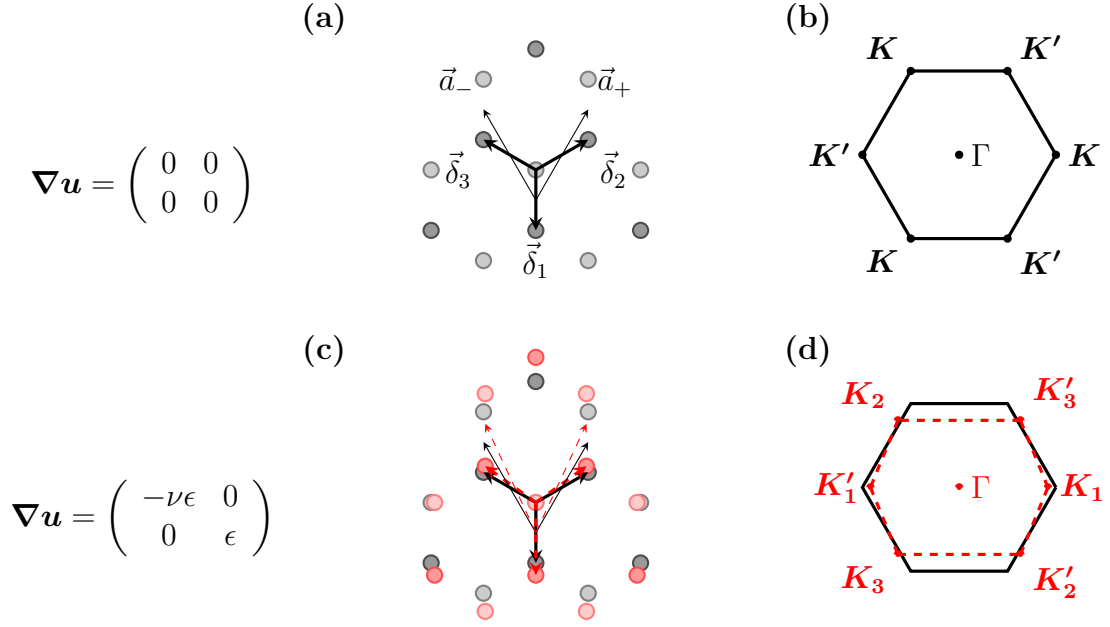
Figure 3.1: Geometry of strained graphene. (a) Unstrained graphene's real space lattice with labeled nearest neighbor vectors ($\vec{\delta}_i$), labeled lattice vectors, $\vec{a}_+$ and $\vec{a}_-$, and with light and dark dots representing the A and B sub-lattices, respectively. (b) The BZ of unstrained graphene with labeled high symmetry points. (c) The real space lattice for 20% uniaxial strain in the $\hat{y}$ direction. Red dots represent the position of the strained atoms while the strained nearest neighbor vector, $\vec{\delta}_i'$, and the strained lattice vectors, $\vec{a}_i''$, are represented with red dashed lines. (d) The unstrained (black, solid) and 20% armchair uniaxial strained (red, dashed) BZ with the now inequivalent Dirac points labeled. $\boldsymbol{\nabla u}$ is the displacement gradient tensor describing the distortion for each row.

expansion of the creation and annihilation operators in Equation 2.2,

$$a_i^\dagger = \frac{1}{\sqrt{N}} \sum_{\vec{k}} e^{i\vec{k}\cdot\vec{R}_i'} a_{\vec{k}}^\dagger$$

$$b_j = \frac{1}{\sqrt{N}} \sum_{\vec{k}'} e^{-i\vec{k}'\cdot\vec{R}_j'} b_{\vec{k}'} \ . \tag{3.2}$$

where $\vec{R}_i'$ and $\vec{R}_j'$ are the positions of the atoms in the strained A and B sub-lattices respectively. These two effects are dependent on one another in an actual physical system. Kitt *et al.* was the first to introduce the modification of the relative positions of the atoms (Kitt et al., 2012).

3.1.2 Strain-altered lattice vectors

A necessary and non-trivial first step toward the inclusion of these modifications is the determination of how the lattice vectors and nearest neighbor vectors are altered by strain. This directly determines how strain modifies the Fourier transforms in Equation 2.2 as well as the hopping energies in Equation 2.1.

In general, the strain is not uniform and the distortion of these vectors has a spatial dependence. In macroscopic continuum mechanics this distortion field is quantified by the elastic deformation field, $\vec{u}(\vec{r})$, which gives the position dependent deformation. Here we follow the Cauchy-Born rule which projects these macroscopic quantities onto the atomic lattice. In this approximation, the position of the i-th atom in the deformed configuration, $\vec{R}_i'$, is given with reference to the undeformed one, $\vec{R}_i$, in terms of the deformation field

$$\vec{R}_i' = \vec{R}_i + \vec{u}(\vec{R}_i) \ .$$

Although it is feasible that the A and B sublattices behave differently at the atomic scale but still yield the same macroscopic response, the Cauchy-Born rule provides a simple and reasonable starting point for the discussion of strain effects.

The strained lattice vector at the i-th lattice site, $\vec{a}'_{i,\pm}$, is then given approximately by

$$
\begin{aligned}
\vec{a}'_{i,\pm}(\vec{r}) &= \vec{R}'_j - \vec{R}'_i \\
&= (\vec{R}_j - \vec{R}_i) + \vec{u}(\vec{R}_j) - \vec{u}(\vec{R}_i) \\
&\simeq \vec{a}_{i,\pm} + (\vec{a}_{i,\pm} \cdot \vec{\nabla})\vec{u}(\vec{R}_i) \\
&= \left(\mathbf{1} + \boldsymbol{\nabla}\boldsymbol{u}(\vec{R}_i)\right) \cdot \vec{a}_{i,\pm} \ ,
\end{aligned}
\tag{3.3}
$$

where $\mathbf{1}$ is the two dimensional identity matrix and the dyadic product $\boldsymbol{\nabla}\boldsymbol{u}(\vec{R}_i)$ is known as the displacement gradient tensor,

$$
\begin{aligned}
[\boldsymbol{\nabla}\boldsymbol{u}]_{ij} = u_{i,j} &= \frac{u_{i,j} + u_{j,i}}{2} + \frac{u_{i,j} - u_{j,i}}{2} \\
&\equiv \tilde{\epsilon}_{ij} + \tilde{\omega}_{ij} \\
\rightarrow \quad \boldsymbol{\nabla}\boldsymbol{u} &= \tilde{\boldsymbol{\epsilon}} + \tilde{\boldsymbol{\omega}} \ ,
\end{aligned}
$$

where $\tilde{\boldsymbol{\omega}}$ is the rotation tensor and $\tilde{\boldsymbol{\epsilon}}$ is the *linear* strain tensor. It is only one part of the full (Lagrange) strain tensor given by $\boldsymbol{\epsilon} = \frac{1}{2}(\boldsymbol{\nabla}\boldsymbol{u} + \boldsymbol{\nabla}\boldsymbol{u}^\top + \boldsymbol{\nabla}\boldsymbol{u}^\top\boldsymbol{\nabla}\boldsymbol{u}) = \tilde{\boldsymbol{\epsilon}} + \frac{1}{2}(\boldsymbol{\nabla}\boldsymbol{u}^\top\boldsymbol{\nabla}\boldsymbol{u})$. It is important to stress that the often used approximating $\vec{a}'_{i,\pm}(\boldsymbol{r}) \simeq (\mathbf{1} + \tilde{\boldsymbol{\epsilon}}) \cdot \vec{a}'_{i,\pm}$ is only valid if the deformation does not involve local rotation ($\tilde{\boldsymbol{\omega}} = 0$). To simplify the notation, the position dependence has been left off of $\boldsymbol{\nabla}\boldsymbol{u}$. Similarly, the strain modified nearest neighbor vectors are $\vec{\delta}'_{i,j}(\vec{r}) = (\mathbf{1} + \boldsymbol{\nabla}\boldsymbol{u}) \cdot \vec{\delta}_j(\vec{r})$ (Kitt et al., 2013a) where i keeps track of the spatial dependence by indicating the unit cell and $j \in 1, 2, 3$ indicates the nearest neighbor vector.

3.1.3   Strain-altered hopping energies

The distortion of the nearest neighbor vectors causes a bond-specific alteration of the hopping energy. By comparing a tight binding treatment of strained graphene to density functional calculations of the same system, Ribeiro and coworkers showed that the dependence of the hopping energy on the distance between carbon atoms can be parameterized as

$$t(|\vec{\delta}_{i,j}|) = t_0 e^{-\beta(|\vec{\delta}_{i,j}|-a)/a} \approx t_0 - \beta t_0 \frac{|\vec{\delta}_{i,j}| - a}{a} \ , \tag{3.4}$$

with $\beta \approx 3$ (Ribeiro et al., 2009). An exponential decay is chosen because it correctly predicts both the nearest neighbor and next nearest neighbor hopping energies (Pereira et al., 2009). The fact that the hopping energy is mostly insensitive to the bond angle greatly simplifies the calculation.

Having already established the form for the strained nearest neighbor vectors, their lengths can be easily computed for small strains

$$|\delta'_{i,j}|^2 = \left(\vec{\delta}_j^\intercal + \vec{\delta}_j^\intercal \ \nabla \mathbf{u}^\intercal \right) \cdot \left(\vec{\delta}_j + \nabla \mathbf{u} \ \tilde{\delta}_\mathbf{j} \right)$$

$$= \vec{\delta}_j^\intercal \cdot \vec{\delta}_j + \vec{\delta}_j^\intercal \cdot (\nabla \mathbf{u} + \nabla \mathbf{u}^\intercal + \nabla \mathbf{u}^\intercal \nabla \mathbf{u}) \cdot \vec{\delta}_j$$

$$\rightarrow |\delta'_{i,j}| \simeq a + \frac{1}{a} \vec{\delta}_j \cdot \boldsymbol{\epsilon} \cdot \vec{\delta}_j \ .$$

Here $\epsilon = \frac{1}{2} \left(\nabla \mathbf{u} + \nabla \mathbf{u}^\intercal + \nabla \mathbf{u}^\intercal \nabla \mathbf{u} \right)$ is the full Lagrangian strain tensor. As was done for the displacement gradient tensor, the spatial dependence of the strain tensor is dropped from the notation for simplicity. As expected, the length of these vectors are dependent only on the the symmetric part of the displacement gradient tensor, the strain.

Thus, to first order the bond-specific nearest neighbor hopping can be written as

$$t_{i,j} = t_0 + \delta t_{i,j} = t_0 - \beta t_0 \frac{1}{a^2} \vec{\delta}_j \cdot \boldsymbol{\epsilon} \cdot \vec{\delta}_j,$$

or

$$\delta t_{i,1} = -\beta t_0 \epsilon_{yy}$$

$$\delta t_{i,2} = -\beta t_0 \left(\frac{3}{4} \epsilon_{xx} + \frac{1}{4} \epsilon_{yy} + \frac{\sqrt{3}}{2} \epsilon_{xy} \right)$$

$$\delta t_{i,3} = -\beta t_0 \left(\frac{3}{4} \epsilon_{xx} + \frac{1}{4} \epsilon_{yy} - \frac{\sqrt{3}}{2} \epsilon_{xy} \right) . \tag{3.5}$$

This fully defines the strain dependences of the modifications in Equations 3.1 and 3.2.

3.1.4 Hamiltonian of strained graphene

All the pieces necessary to modify the nearest neighbor tight binding approach from Chapter 2 are now in place. The first modification to include the approximated hopping energy in Equation 3.1,

$$H = -\sum_{<i,j>} \left((t_0 + \delta t_{i,j}) a_i^\dagger b_j + (t_0 + \delta t_{j,i}) b_j^\dagger a_i \right) .$$

In situations such as the deformation of graphene around a sharp scanning tunneling microscopy tip, it is not necessarily true that $\delta t_{i,j} = \delta t_{j,i}$. In these extreme strain situations the continuum approximation can break down, the sub-lattice symmetry can be broken, and it is possible that $\delta t_{i,j} \neq \delta t_{j,i}$. However, for strains that vary slowly with respect to the lattice spacing, the continuum approximation holds and $\delta t_{i,j} \simeq \delta t_{j,i}$ (Sloan et al., 2013). This assumption will be made throughout the

discussion below. As a result, the real space Hamiltonian in Equation 3.1 can be approximated to first order in strain as

$$H \simeq - \sum_{<i,j>} (t_0 + \delta t_{i,j}) \, a_i^\dagger b_j + \text{H.C.} \, ,$$

with the strain dependence of $\delta t_{i,j}$ given by Equation 3.5.

Using the Fourier transforms of the creation and annihilation operators in Equation 3.2, the Hamiltonian is written in reciprocal space as

$$H = -\frac{1}{N} \sum_{<i,j>} \sum_{\vec{k},\vec{k}'} (t_0 + \delta t_{i,j}) \, e^{i(\vec{k}-\vec{k}')\cdot\vec{R}_i'} e^{-i\vec{k}'\cdot\vec{\Delta}_{i,j}'} a_{\vec{k}}^\dagger b_{\vec{k}'} + \text{H.C.} \, , \qquad (3.6)$$

where $\vec{\Delta}_{i,j}' = \vec{R}_j' - \vec{R}_i'$. Comparing this Hamiltonian to the unstrained Hamiltonian in Equation 2.3 highlights the effects of strain. The modifications of the hopping energy and the lattice positions are evident. Additionally, the $\vec{R}_i'$ term is no longer the only i dependent term. Instead, the strain can vary throughout the lattice resulting in the i dependence of both $\delta t_{i,j}$ and $\vec{\Delta}_{i,j}'$. In Appendix B it is shown that the i dependences can be neglected to first order in small parameters the as long as $\delta t_{i,j}$ and $\boldsymbol{\nabla u}$ do not have Fourier components with frequencies $\boldsymbol{K} - \boldsymbol{K}'$. This slowly varying approximation will be applied in the dicussion that follows. The i dependence is then eliminated through the substitutions $\delta t_{i,j} \to \delta t_j =< \delta t_{i,j} >$ and $\boldsymbol{\nabla u}_i \to< \boldsymbol{\nabla u} >$ where the averages are over i.

After making the slowly varying approximation, the Hamiltonian simplifies to

$$H = - \sum_{\vec{k}} \sum_{j} (t_0 + \delta t_j) \, e^{-i\vec{k}\cdot\vec{\Delta}_{i,j}'} a_{\vec{k}}^\dagger b_{\vec{k}} + \text{H.C.}$$

By applying the low energy approximation and using the form for the strained vectors

in Equation 3.3, the Hamiltonian can be approximated in terms of the three small parameters: qa, $\boldsymbol{\epsilon}$, $\boldsymbol{\nabla u}$. Near $\boldsymbol{K}_i$ the Hamiltonian becomes

$$
\begin{aligned}
H &\simeq -\sum_{\vec{q}}\sum_{j}\left(t_0+\delta t_j\right)e^{-i(\boldsymbol{K}_i+\vec{q})\cdot(\mathbf{1}+\boldsymbol{\nabla u})\cdot\vec{\Delta}_j}a_{\vec{k}}^{\dagger}b_{\vec{k}}+\text{H.C.} \\
&\simeq -\sum_{\vec{q}}\sum_{j}\left(t_0+\delta t_j\right)e^{-i\boldsymbol{K}\cdot\vec{\Delta}_j}(1-i\vec{q}\cdot\vec{\Delta}_j)(1-i\boldsymbol{K}_i\cdot\boldsymbol{\nabla u}\cdot\vec{\Delta}_j)a_{\vec{k}}^{\dagger}b_{\vec{k}}+\text{H.C.} \\
&\simeq \underbrace{-t_0\sum_{\vec{q}}\sum_{j}(1-i\vec{q}\cdot\vec{\Delta}_j)e^{-i\boldsymbol{K}\cdot\vec{\Delta}_j}a_{\vec{k}}^{\dagger}b_{\vec{k}}}_{H_0}-\underbrace{\sum_{\vec{q}}\sum_{j}\delta t_j e^{-i\boldsymbol{K}\cdot\vec{\Delta}_j}a_{\vec{k}}^{\dagger}b_{\vec{k}}}_{H_{hopping}} \\
&\quad +\underbrace{it_0\boldsymbol{K}_i\cdot\boldsymbol{\nabla u}\sum_{\vec{q}}\cdot\sum_{j}\vec{\Delta}_j e^{-i\boldsymbol{K}\cdot\vec{\Delta}_j}a_{\vec{k}}^{\dagger}b_{\vec{k}}}_{H_{lattice}}+\text{H.C.} ~,
\end{aligned}
$$

with a similar form near $\boldsymbol{K'}$ except with $\boldsymbol{K}$ replaced with $\boldsymbol{K'}$. The full Hamiltonian nicely breaks up into three parts. The first part, H_0, exactly matches the low energy Hamiltonian of unstrained graphene from Equations 2.5 and 2.3. Strain, then, acts to perturb the unstrained Hamiltonian through $H_{hopping}$ and $H_{lattice}$. Returning to the geometry in Figure 3.1, $H_{hopping}$ originates from the deformation of the nearest neighbor vectors and the corresponding bond-specific hopping energy. $H_{lattice}$ is a result of the deformation of the lattice vectors. Before it was originally introduced by Kitt *et al.* (Kitt et al., 2012), the second term was neglected by the research community. The lattice was treated as if it were undeformed and strain only acted to alter the interactions between nearest neighbors. However, both of the perturbations are first order in small parameters; $H_{hopping}$ is $\mathcal{O}(\boldsymbol{\epsilon})$ while $H_{lattice}$ is $\mathcal{O}(\boldsymbol{\nabla u})$. Consequently, they contribute on equal footing and $H_{lattice}$ should be included.

3.1.5 Pseudovector potentials

The perturbations $H_{hopping}$ and $H_{lattice}$ mimic the effects of a magnetic field. In the minimum coupling scenario the presence of a magnetic field is included using the substitution $\vec{p} \rightarrow \vec{p} - e\vec{A}$ where $\vec{A}$ is the vector potential related to the magnetic field through $\vec{B} = \nabla \times \vec{A}$. The perturbations $H_{hopping}$ and $H_{lattice}$ contribute a similar shift to graphene's crystal momentum: $\hbar\vec{k} \rightarrow \hbar\vec{k} - e\vec{\mathcal{A}}$ where $\vec{\mathcal{A}}$ is the pseudovector potential. In this formalism the crystal momentum shifts are referenced to the *undeformed* BZ. This identification can be made because like the matrix elements of H_0, the perturbations are off diagonal and do not couple the $\boldsymbol{K}$ and $\boldsymbol{K'}$ points. Further, they provide only a strain-dependent complex offset that is independent of the crystal momentum.

The form of H_0 shown in Equation 2.6 allows the isolation of the x and y components of $\vec{\mathcal{A}}$ from the real and imaginary parts of the perturbations

$$
\mathcal{A}_{x,\boldsymbol{K}} = -\vec{\mathcal{A}}_{x,\boldsymbol{K'}} = -\frac{1}{v_f e} Re[h_{hopping} + h_{lattice}]
$$
$$
\mathcal{A}_{y,\boldsymbol{K}} = \vec{\mathcal{A}}_{y,\boldsymbol{K'}} = \frac{1}{v_f e} Im[h_{hopping} + h_{lattice}] \ , \tag{3.7}
$$

where

$$
h_{hopping} = -\sum_j \delta t_j e^{-i\boldsymbol{K}\cdot\vec{\Delta}_j} = v_f e \frac{\phi_0}{2a} \left(-\frac{\beta}{2\pi}(\epsilon_{xx} - \epsilon_{yy}) \mp \frac{\beta}{\pi}\epsilon_{xy} \right)
$$
$$
h_{lattice} = it_0 \boldsymbol{K}_i^{(')} \cdot \boldsymbol{\nabla u} \cdot \sum_j \vec{\Delta}_j e^{-i\boldsymbol{K}_i^{(')}\cdot\vec{\Delta}_j} = \hbar v_f \boldsymbol{K}_i^{(')} \cdot \boldsymbol{\nabla u} \cdot (\pm\hat{x} - i\hat{y}) \ . \tag{3.8}
$$

with the top sign in the $\pm$ for $\boldsymbol{K}$ the bottom sign for $\boldsymbol{K'}$, and $\boldsymbol{K}^{(')}$ indicating the

appropriate $\boldsymbol{K}$ or $\boldsymbol{K'}$. The resulting pseudovector potentials are

$$\vec{\mathcal{A}}_{\boldsymbol{K_1}} = -\vec{\mathcal{A}}_{\boldsymbol{K_1'}} = \vec{\mathcal{A}}_p + \frac{\phi_0}{2a} \begin{pmatrix} -\frac{4}{3\sqrt{3}}[\boldsymbol{\nabla u}]_{xx} \\ -\frac{4}{3\sqrt{3}}[\boldsymbol{\nabla u}]_{xy} \end{pmatrix}$$

$$\vec{\mathcal{A}}_{\boldsymbol{K_2}} = -\vec{\mathcal{A}}_{\boldsymbol{K_2'}} = \vec{\mathcal{A}}_p + \frac{\phi_0}{2a} \begin{pmatrix} \frac{2}{3\sqrt{3}}[\boldsymbol{\nabla u}]_{xx} - \frac{2}{3}[\boldsymbol{\nabla u}]_{yx} \\ -\frac{2}{3}[\boldsymbol{\nabla u}]_{yy} + \frac{2}{3\sqrt{3}}[\boldsymbol{\nabla u}]_{xy} \end{pmatrix}$$

$$\vec{\mathcal{A}}_{\boldsymbol{K_3}} = -\vec{\mathcal{A}}_{\boldsymbol{K_3'}} = \vec{\mathcal{A}}_p + \frac{\phi_0}{2a} \begin{pmatrix} \frac{2}{3\sqrt{3}}[\boldsymbol{\nabla u}]_{xx} + \frac{2}{3}[\boldsymbol{\nabla u}]_{yx} \\ \frac{2}{3}[\boldsymbol{\nabla u}]_{yy} + \frac{2}{3\sqrt{3}}[\boldsymbol{\nabla u}]_{xy} \end{pmatrix},$$

$$\text{with } \vec{\mathcal{A}}_p = \frac{\phi_0}{2a} \begin{pmatrix} \frac{\beta}{2\pi}(\epsilon_{xx} - \epsilon_{yy}) \\ -\frac{\beta}{\pi}\epsilon_{xy} \end{pmatrix}, \tag{3.9}$$

with $\phi_0 = \frac{h}{e}$ and the various $\boldsymbol{K}_i$ points defined in Figure 3.1(d). The common term $\vec{\mathcal{A}}_p$ is proportional to the logarithmic derivative of the hopping, β, and arises from the hopping perturbations, δt_j, alone. It agrees with past derivations (Castro Neto et al., 2009; Vozmediano et al., 2010). The additional terms are the corrections due to lattice deformations completing the derivation of the strain-induced pseudovector potential.

3.2 Pseudovector potential discussion

The pseudovector potential in Equation 3.9 was found using an analogy between the minimal substitution formalism and the shift in crystal momentum caused by strain. Even though this analogy is very strong, there are several discrepancies. First, unlike a magnetic field, a spatial deformation can not break time reversal symmetry. This limitation manifests itself in Equation 3.9 through the sign difference between pseudovector potentials at time reversed points: $\vec{\mathcal{A}}_{\boldsymbol{K}_i} = -\vec{\mathcal{A}}_{\boldsymbol{K}_i'}$. Second, strictly

speaking the pseudovector potential does not have gauge freedom. It is true that there are a class of pseudovector potentials which all have the same curl. However, each element of this class corresponds to a measurably different physical realization of the system. Each element has a different strain distribution and correspondingly different strain-induced shifts in the momentum. A real vector potential is determined only by its curl whereas a pseudovector potential has a concrete interpretation beyond its curl. Finally, in the minimal substitution formalism the gauge independent momentum is replaced with the gauge-dependent canonical momentum. This does not occur for strain-induced pseudovector potentials. The definition of the crystal momentum is not changed by strain. To recognize these differences, the strain-induced momentum shifts are referred to as pseudovector potentials.

Another important subtlety is the dependence of the pseudovector potential on the orientation of the strain relative to the crystal. Uniaxial strain of the same macroscopic value but at a different crystallographic orientation will result in different pseudovector potentials. The form for the pseudovector potentials in Equations 3.9 assume that the tensors are written with the x axis aligned with a zigzag direction. They can be rewritten for different orientations by rotating the tensors so that their x axis is aligned with the zig zag direction, calculating the pseudovector potential using Equations 3.9, and then rotate the resulting pseudovector potential back into the original reference frame.

Calculations preceding Kitt *et al.* (Kitt et al., 2012) included only the term arising from hopping alterations ($\vec{\mathcal{A}}_p$ in Equation 3.9) in the pseudovector potential. In this so called brick-wall model, strain only modified hopping energies. The positions of the atoms were left fixed like bricks. Since $\beta \approx 3$, the new terms resulting from the deformation of the lattice contributes equally to hopping alterations. These terms are not only the same order in strain, but they have similar numerical coefficients. It is

also worth emphasizing that taking explicit consideration of the lattice deformations leads to a vector potential that is different for all the corners of the BZ. This is expected because under an arbitrary deformation the equivalence among the three $\boldsymbol{K}$ and $\boldsymbol{K'}$ points is lost.

When the lattice terms are neglected, the pseudovector potential does not properly account for the shift in the Dirac points. Consider, for example, the seemingly trivial case of tensile isotropic strain. The brick-wall form of the pseudovector potential, $\vec{\mathcal{A}}_p$, predicts that there should be no shift in the Dirac points ($\epsilon_{xx} = \epsilon_{yy}$ and $\epsilon_{xy} = 0$ in equation 3.9). Physically however, the BZ must shrink isotropically under tensile isotropic strain, and, because the lattice symmetry is unchanged, the Dirac points should follow the corners of the shrinking BZ. The pseudovector potential should correspond to a shift of each Dirac point toward the Γ point. Further, the direction of this shift is different for $\boldsymbol{K}_1$ then it is for $\boldsymbol{K}_2$ then it is for $\boldsymbol{K}_3$. This illustrate two points: Prior calculations were incomplete and the pseudovector potential is not necessarily the same for each $\boldsymbol{K}$ point.

In Figure 3.2, the reciprocal space shifts of the Dirac points predicted by the brick-wall and the lattice-corrected forms of the pseudovector potential are compared. The contours represent the dispersion of strained graphene calculated using a nearest neighbor tight binding model which accounts for both the strain-induced changes in hopping amplitudes and the lattice deformation (Pereira et al., 2009). The calculation of the shape of the strained BZ is described in Appendix A. For isotropic tensile strain, the lattice-corrected pseudovector potential in Equation 3.9 properly predicts the displacement of each Dirac point due to strain. The less trivial cases of uniaxial or shear strain are also shown in Figure 3.2. The differences between the red (brick-wall) and orange (lattice-corrected) arrows make it clear that the lattice-corrections are needed to determine the absolute position of the Dirac points in reciprocal space.
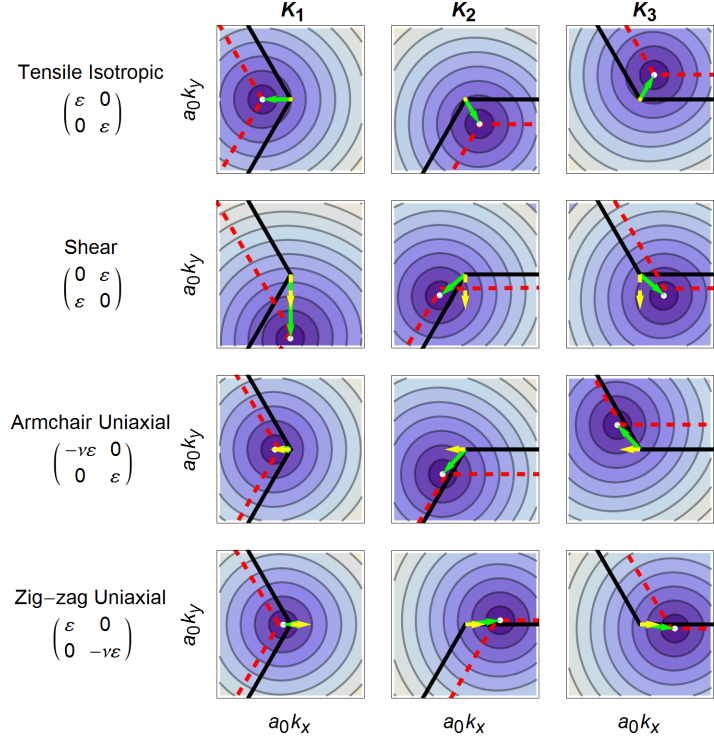
Figure 3.2: A geometric depiction of the importance of the lattice-corrections to the strain-induced pseudovector potentials. Contours of the band structure of graphene under tensile isotropic strain, shear strain, armchair uniaxial strain, and zig-zag uniaxial strain (rows), for $\epsilon = 1\%$ near the three $\boldsymbol{K}$ points (columns) are overlaid with the BZ of unstrained (solid, black) and strained (dashed, red) graphene. Vectors mark the displacement of the Dirac points predicted by the brick-wall ($\vec{\mathcal{A}}_p$, dashed, yellow arrow) and the lattice-corrected ($\vec{\mathcal{A}}_{\boldsymbol{K}_i}$, solid, green arrow) models, with the white dots marking the positions of the Dirac points for strained graphene. The lattice-corrected vectors appropriately predict the shift in the Dirac point. The yellow vectors appears as a dot for isotropic strain because the brick-wall model of the vector potential does not predict a shift in the Dirac points. Each plot is square with an area of 0.12^2.

3.3   Pseudomagnetic fields

Having discussed the strain-induced analog of a real vector potential, the so called pseudovector potential, it is natural to extend the analogy to pseudomagnetic fields. In graphene, Landau level quantization can occur without the application of a magnetic field. This is because Landau level quantization requires only that there is a momentum shift which can be expressed as $\vec{p} - e\vec{A}$ where $\vec{p}$ is the momentum operator which obeys the canonical commutation relationship with the position operator x, $[x, p_x] = i\hbar$ (Goerbig, 2011). It does not require a specific origin of $\vec{A}$. Thus, strain alone can quantize electrons into Landau levels as if they were in a magnetic field given by $\vec{B} = \vec{\nabla} \times \vec{\mathcal{A}}$. This effect has recently been observed using scanning tunneling microscopy of accidentally strained graphene (Levy et al., 2010; Yan et al., 2012; Yeh et al., 2011) and of engineered graphene analogs (Gomes et al., 2012).

This phenomenology is very powerful but has several subtleties. First, it should be reiterated that despite the fact that the electrons quantize into Landau levels, there is no magnetic field. Strain does not somehow generate a magnetic field in a region near the graphene. Second, strain can not break time reversal symmetry. This symmetry is preserved via the relationship $\vec{\mathcal{A}}_{\boldsymbol{K}_i} = -\vec{\mathcal{A}}_{\boldsymbol{K}_i'}$ in Equation 3.9 which causes the pseudomagnetic field to point in opposite direction at time reversed $\boldsymbol{K}_i$ points. As a result, pseudomagnetic fields cannot be used to create fractional quantum Hall states or to differentiate between right and left circularly polarized light. An additional subtlety is the lack of spatial dependence in the pseudovector potential derived here. If these calculations are treated as a local computation in the vicinity of position $\vec{r}$ then the spatial dependence of $\boldsymbol{\epsilon}$ and $\boldsymbol{\nabla u}$ provide the spatial dependence for $\vec{\mathcal{A}}(\vec{r})$ as long as this pseudomagnetic field is relatively constant on the scale of the magnetic length (Castro Neto et al., 2009).

The discussion of the pseudomagnetic field in the following sections begins with a discussion of the unimportance of the lattice-corrections when calculating pseudomagnetic fields. Next, a pressurized triangular graphene sealed microchamber (Guinea et al., 2010) is used as an example to illustrate how pseudomagnetic fields might be engineered and measured. This is followed by the prediction of a particularly interesting device, the hourglass-shaped graphene sealed microchamber. This device should have large localized pseudomagnetic fields which can be accessed using plasmonic field enhancement. Finally, the importance of proper continuum modeling will be demonstrated by considering circular graphene sealed microchambers.

3.3.1   Contribution of lattice-corrections to the pseudomagnetic field

Although the lattice-corrections in Equation 3.9 are finite and, in general, have a position dependence, it happens that the lattice-corrections to the pseudovector potential do not effect the pseudomagnetic field. This has been pointed out recently by de Juan *et al.* (de Juan et al., 2013). Using Equations 3.7 and 3.8 the pseudovector potential from lattice-corrections can be recast as

$$\vec{\mathcal{A}} = -\frac{\hbar}{e} \boldsymbol{K}_i^{(')} \cdot \boldsymbol{\nabla u} = -\frac{\hbar}{e} \vec{\nabla} \left(\boldsymbol{K_i^{(')}} \cdot \vec{u} \right) \ ,$$

where the order was changed using $K_j u_j \nabla_i = \nabla_i K_j u_j$. Since the above is a total derivative, it cannot contribute to the pseudomagnetic field because $\nabla \times \nabla \phi \equiv 0$. Thus, the only term in Equation 3.9 which contributes to the pseudomagnetic field is $\vec{\mathcal{A}}_p$. As a result, even though the pseudovector potential is different at the three $\boldsymbol{K}$ points, the pseudomagnetic field is the same at each $\boldsymbol{K}$ point and opposite in sign at the $\boldsymbol{K'}$ points.

The lattice-corrections are still needed to correctly describe the shift in the po-

sitions of the Dirac points due to strain relative to a global frame of reference. This includes the momentum-sensitive electronic tunneling to/from strained graphene from/to another system, probe, or contact (Fogler et al., 2008).

3.3.2 Pressurized graphene sealed microchambers: pseudomagnetic field test bed

It is tantalizing to consider the possibility of replicating very high magnetic field physics without resorting to expensive and destructive pulsed field techniques. Experimental measurements of pseudomagnetic fields (Levy et al., 2010; Yan et al., 2012; Yeh et al., 2011; Gomes et al., 2012) have validated the theory and generated excitement in the possibility of strain engineering. However, to date no strain device has been predicted, fabricated, and then shown to have the desired properties. The challenge now is to design and build devices which use this new science to enable unique device functionality such as devices which use the Quantum Hall effect at room temperature with no magnetic field.

This process of strain engineering pseudomagnetic field devices is non-trivial from almost any standpoint. There are no established techniques for generating spatially varying strains in atomically thin materials, and thus, no there are no constrains for the theorists who model these systems. Strain engineering to date has been limited to spatially uniform strains created using strain transfer from an underlying polymer (Yu et al., 2008; Ni et al., 2008; Tsoukleri et al., 2009; Huang et al., 2009; Mohiuddin et al., 2009; Frank et al., 2010; Yoon et al., 2011), an underlying piezoelectric material, (Ding et al., 2010; Jie et al., 2013) or through the application of hydrostatic pressure (Proctor et al., 2009; Clark et al., 2013). Generating specifically designed spatially varying strains, however, is a whole other ball game. Beyond this challenge is the theoretical difficulty of the inverse problem. The desired property, the

pseudomagnetic field, is a function of the curl of the strain which is itself a function of the surrounding environment through continuum mechanics. To complicate these non trivial mathematics is a general lack of understanding in how an atomically thin material, like graphene, responds to its surroundings. All in all, there are several challenges which must be overcome before new strain engineered devices can be designed and realized.

One early, experimentally accessible design which is predicted to yield fairly uniform pseudomagnetic fields is a pressurized triangular graphene sealed microchamber (Guinea et al., 2010). To make the Landau levels as narrow and well defined as possible Guinea *et al.* proposed a variety of designs for nearly uniform pseudomagnetic fields. They noticed that strain profiles with symmetries similar to graphene's lattice tend to generate smooth effective pseudomagnetic fields. The triangular pressurized graphene sealed microchamber represents the most experimentally realizable of their designs. In this system equilateral triangle microchambers are etched into the underlying substrate and graphene is put across the top, sealing the gas inside. When external pressure is applied the graphene is pushed into the microchamber generating a spatially varying strain which yields fairly uniform pseudomagnetic fields.

Shown in Figure 3.3 is the spatial distribution of the pseudomagnetic field for a graphene sealed equilateral triangle microchamber with 50 nm legs oriented along the zigzag direction pressurized to 14 MPa. The pictured pseudomagnetic field is for the $\boldsymbol{K}$ points, the pseudomagnetic field for $\boldsymbol{K'}$ points would have the same magnitude but the opposite sign. However, Landau level quantization is insensitive to this sign difference. At the pressure shown, the graphene sheet is under less than 0.26% strain. Such small strains can generate such large pseudomagnetic fields because the small spatial extent of the device yields large curls and correspondingly large pseudomagnetic fields.
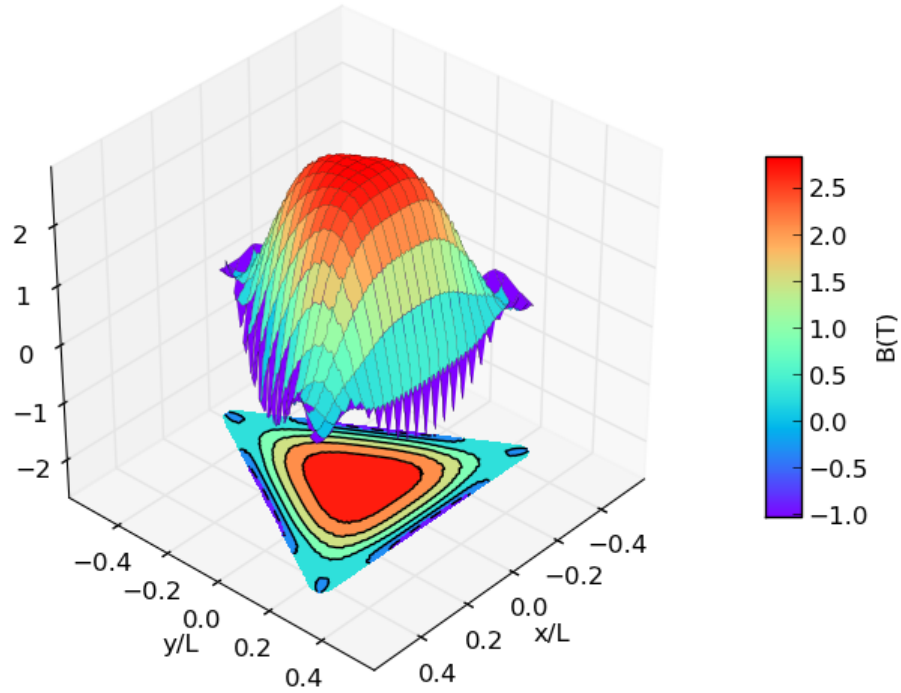
Figure 3.3: Pseudomagnetic fields in a pressurized, triangular, graphene sealed mi-crochamber. A surface plot of the predicted spatial distribution of the pseudomagnetic field is shown above a contour plot with the same color scale. The equilateral triangular microchamber has edge lengths of 50 nm and a 2 nm fillets is is under 14 MPa of pressure. The graphene zigzag crystallographic orientation is in the $\hat{x}$ direction. The pseudomagnetic field is fairly uniform near the center of the microchamber.

To generate this figure, the strain fields calculated using finite element analysis were used to calculate the spatial distribution of the pseudovector potential from $\vec{\mathcal{A}}_p$ in Equation 3.9. Although $\vec{\mathcal{A}}_p$ was derived for the special case of in-plane strains, it applies to out of plane strains as well. This is because it is a function of the full Lagrangian strain tensor which properly references the deformation back to the undeformed coordinates. Finally, the curl of $\vec{\mathcal{A}}_p$ is taken numerically to get the pseudomagnetic field.

Finite element analysis was performed using Comsol Multiphysics with a two-dimensional thin plate model including geometric non-linearity. The edges were fixed and the pressure was applied using a face load. Graphene's Young's Modulus of 1 TPa and thickness of 3.5 Å(Lee et al., 2008) were used along with the Poisson ratio of graphite of 0.165 (Blakslee et al., 1970). To make the triangles more realistic 2 nm radius fillets were included on the corners to smooth the sharp boundaries. The surface was meshed with triangles with a maximum element size of 1 nm and strain fields were evaluated in the mid-plane of the plate.

The importance of crystalographic orientation is illustrated by this triangular graphene sealed microchamber. If the graphene is fixed while the microchamber is rotated underneath it, the pseudomagnetic field changes drastically. Figure 3.4 compares the two extreme cases: The Zigzag edge along the legs of the triangle and the armchair edge along the legs of the triangle. This 30 degree rotation ruins the large uniform pseudomagnetic field. Thus, when fabricating these devices care need to be taken to orient the graphene in the appropriate direction. One possible method to accomplish this is placing the graphene on an elastic polymer as an intermediate step. This would allow the determination of the crystallographic orientation using the polarization dependence of the Raman strain response (Huang et al., 2009). The graphene on polymer could be incorporated pick and place transfer technique which

(a) Zigzag oriented   **(b)** Armchair oriented
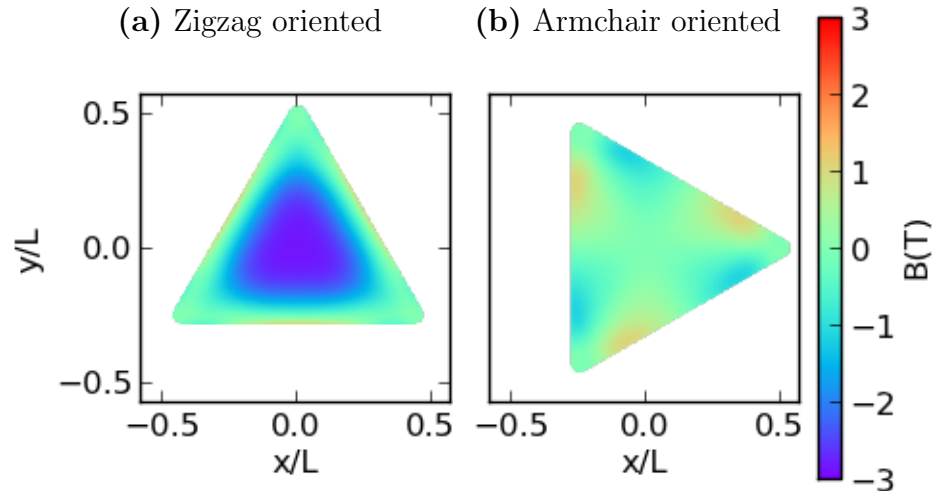
Figure 3.4: The effects of crystallographic orientation on the pseudomagnetic field for equilateral triangle graphene sealed microchambers with 50 nm legs and 2 nm fillets under 14 MPa of applied pressure. The zigzag crystallographic orientation is along the $\hat{x}$ direction for both plots and both plots are referenced to the same color bar. In (a) and (b) the underlying microchamber is rotated such that the legs of the triangle are along the zigzag and armchair directions respectively. The pseudomagnetic field changes drastically when the substrate is rotated.

often use an intermediate polymer layer (Dean et al., 2010; Zomer et al., 2011). Since different orientations can result in such different physics one should consider all crystal orientations when theoretically modeling a device.

Graphene sealed microchambers define a class of strain engineered devices which could provide a test-bed for strain engineering. Even though graphene sealed microchambers do not possess the well-defined electrical current path needed for electronic devices, they should still be useful as a strain engineering test-bed. They

represent an experimentally realizable method of generating measurable pseudomagnetic fields. Such devices have been made in the past. Micron sized graphene sealed microchambers are used in the study of how graphene slides presented in Chapter 4. Additionally, the Landau levels should be measurable using optical probes or local probes such as scanning tunneling spectroscopy. In particular, due to electron-phonon coupling the phonon energy measured by Raman spectroscopy is renormalized when this energy matches specific Landau level transitions (Goerbig, 2011). These magneto-phonon resonances have been observed on multilayer epitaxial graphene (Faugeras et al., 2009), on single layer graphene like regions on the surface of graphite crystals (Faugeras et al., 2011), and for CVD graphene on SiO_2 (Kim et al., 2013). Thus, it is easy to envision an experiment where a graphene sealed microchamber is pressurized while the Raman spectrum is measured *in situ*. Monitoring these energy fluctuations as the pseudomagnetic field is tuned by changing the applied pressure would provide an experimental test of the predicted pseudomagnetic fields.

In summary, pressurized graphene sealed microchambers represent a unique testbed for studying pseudomagnetic field effects. The strain distributions can be easily treated theoretically using finite element analysis, the predicted devices are experimentally realizable, and the resulting pseudomagnetic fields could be measured with optical techniques such as Raman spectroscopy.

3.3.3 Large, localized, plasmonically enhanced pseudomagnetic fields

Microchambers with different shapes were simulated using the same technique as for equilateral triangles. The predicted pseudomagnetic field distributions for simple convex shapes including circles, squares, rectangles, hexagons, and acute triangles were not compelling. Concave devices, however, proved much more interesting. When the graphene bends around a tip, the strain fields change rapidly causing large but

localized pseudomagnetic fields. Usually such a localized effect would be difficult to measure optically. However, the tip has a second, special function. It can enhance an optical field making the local effects measurable. If the optical field enhancement region and the region of large pseudomagnetic field were to overlap, Raman spectroscopy could be used to directly probe the high field regions.

An hourglass shaped device yields a near perfect agreement between the location of the plasmonic field enhancement and the regions of large pseudomagnetic fields. The hourglass device and plasmonic response is illustrated in Figure 3.5. The field enhancement, modeled by Arif Çetin, was modeled using a 3-dimensional finite difference time domain technique. Devices would consist of a periodic, two dimensional array of the unit cell shown in (a) and (b). In this way, any graphene sheet would cover multiple devices, increasing the signal. The unwanted signal from the supported graphene between hourglasses is minimized by destructive interference of the incident and emitted light upon reflection off the gold substrate. Device geometry, detailed in (a) and (b), was chosen so that the plasmon resonance wavelength, shown in (c), was in an experimentally accessible region. The dielectric function of the metallic layers are obtained from Palik (Palik, 1985). The predicted reflectivity in (c) was found using a power monitor located 1 μm from the structure. In (d) the field enhancement of the device for light polarized in the x direction is shown. It is calculated using a field monitor located at the top surface of the top gold layer. The Raman enhancement goes as the square of the intensity enhancement since the intensity of the incident light and the intensity of the inelastically scattered light are both enhanced. The resulting Raman enhancement is greater than 5×10^5 in the region extending roughly 2 nm away from the tips. As a result, the signal measured from these tiny regions should be 3 orders of magnitude stronger than the signal from the rest of the hourglass.
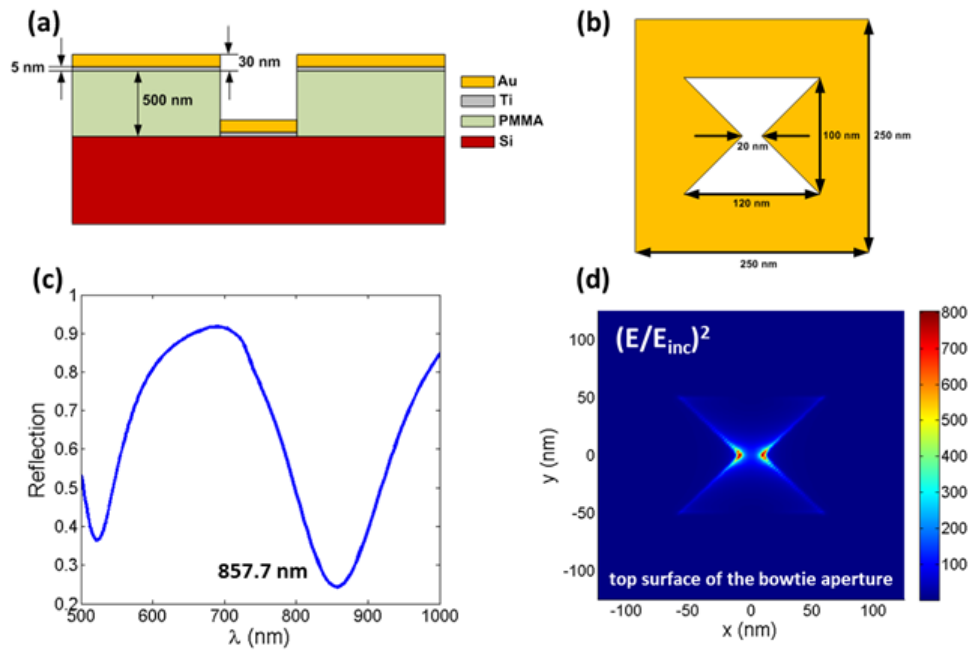
Figure 3.5: The plasmonic enhancement in an hourglass microchamber. The drawings in (a), the side view, and (b), the top view, detail the geometry of one unit cell of the plasmonic device. In (c) the predicted spectral reflectivity of the device is plotted. The large intensity enhancement at the top surface near the tips is plotted in (d).

The pseudomagnetic field distribution resulting from sealing the microchambers shown in Figure 3.5 with graphene and applying 14 MPa of pressure is shown in Figure 3.6. The pseudomagnetic fields reach the impressive value of 60 Tesla near the tip. This small region of large pseudomagnetic field is made experimentally accessible by the plasmonic field enhancement. When compared, the region of high pseudomagnetic field and the regions of large field enhancement are almost indistinguishable. This should allow for the measurement of pressure tunable, very large pseudomagnetic fields using Raman spectroscopy.

3.3.4 The necessity of proper continuum modeling

The first step toward modeling pseudomagnetic fields is the difficult task of determining the expected strains. This is complicated for several reasons. First, the large deflection of thin plates is often a difficult nonlinear problem. Second, many well-accepted approximate continuum models are not valid for pseudomagnetic fields. Historically, most works sought approximations that accurately determined aspects of the deflection profile, sacrificing the accuracy of the strain profile in the process. Models that do not correctly predict the strain distribution can not be used to predict pseudomagnetic fields. Finally, the form of the interactions between atomically thin sheets and their surrounding environment is not yet completely understood. As a result, calculating strains can be a tricky task.

Chapter 4 is a discussion of new discoveries dealing with the interaction between graphene and its supporting substrates. These discoveries result in more exact strain distributions that are modeled with continuum and atomstic modeling and confirmed experimentally. In this section we will demonstrate how these advances in strain modeling drastically alter the predicted pseudomagnetic fields.

The symmetry of circular sealed microchambers makes analytic solutions for the
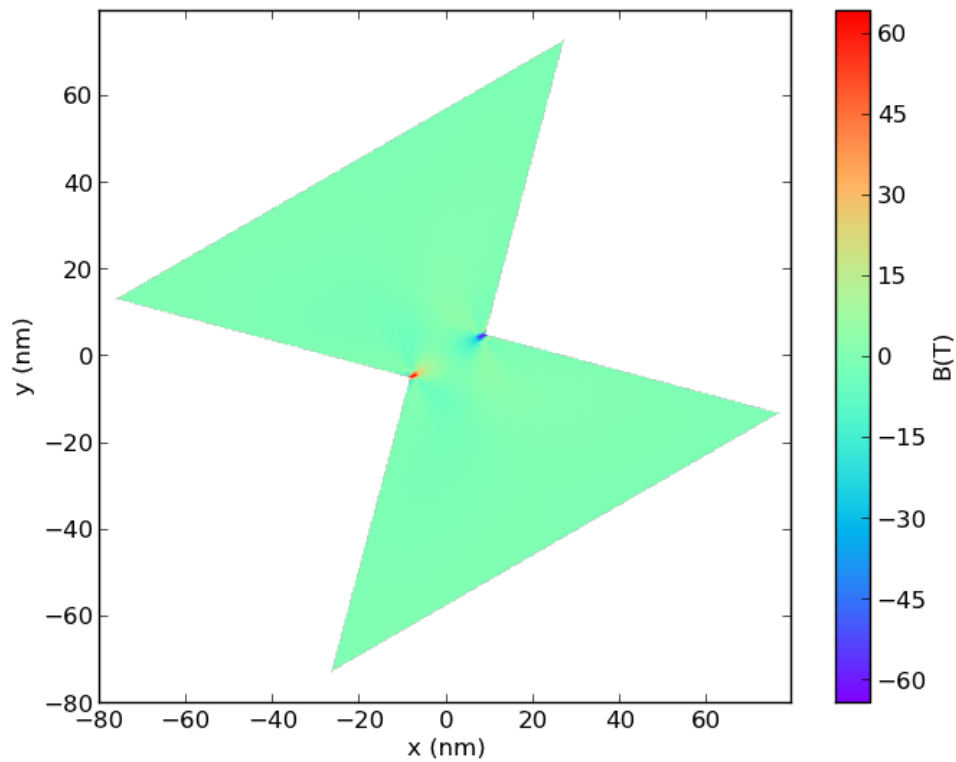
Figure 3.6: Large pseudomagnetic fields near the corners of a pressurized hourglass graphene sealed microchamber are visible in the image plot of the predicted pseudo-magnetic fields. The microchamber is formed by the union of two right triangles. This leaves two 90 degree tips separated by 20 nm. The device is pressurized to 14 MPa of pressure. The graphene zigzag crystallographic orientation is in the $\hat{x}$ direction. The pseudomagnetic fields are localized to the plasmonically enhanced regions of Figure 3.5

strain possible. In fact, there are several different models of increasing accuracy which can be compared. The pseudomagnetic field for each is calculated from the curl of the vector potential which contributes to the pseudomagnetic field, $\vec{\mathcal{A}}_p$ in Equation 3.9,

$$\vec{\mathcal{A}}_{p,cyl} = \frac{\phi_0}{2a}\frac{\beta}{2\pi} \begin{pmatrix} (\epsilon_{\rho\rho} - \epsilon_{\phi,\phi})cos(3\phi) - 2\epsilon_{\rho,\phi}sin(3\phi) \\ -(\epsilon_{\rho\rho} - \epsilon_{\phi,\phi})sin(3\phi) - 2\epsilon_{\rho,\phi}cos(3\phi) \end{pmatrix} ,$$

where $\vec{\mathcal{A}}_{p,cyl}$ is in cylindrical coordinates. Since the strains in cylindrical graphene sealed microchambers have no ϕ dependence and no shear terms, the ϕ dependence in the pseudomagnetic field,

$$\vec{B} = \frac{\phi_0}{2a}\frac{\beta}{2\pi} \sin(3\phi) \left[3\frac{1}{r}(\epsilon_{\rho\rho} - \epsilon_{\phi\phi}) - \frac{1}{r}\frac{\partial}{\partial r}\left[r(\epsilon_{\rho\rho} - \epsilon_{\phi\phi})\right]\right] \hat{z} ,$$

is a reflection of the lattice symmetry.

The spatial distributions of pseudomagnetic fields predicted using three different continuum models are shown in Figure 3.7. For each continuum model a surface plot of the pseudomagnetic field is plotted above a contour plot. The boundary of each plot is positioned at the point where the strains, and thus the pseudomagnetic fields, go to zero. In Figures 3.7a and 3.7b the plots terminates at the edge of the circular microchamber whereas in 3.7c the plot extends further because in this case the strain is allowed to spread to the supported graphene. From left to right the strain distributions used as input become more accurate. In each model the microchamber has a radius of 100 nm and is put under 70 MPa of pressure.

The strain distribution used in Figure 3.7a is based on an approximate solution useful for interpreting bulge tests. In this popular approximation the large deflection lateral displacement is assumed to have the same form as that of the small deflection limit (Timoshenko and Woinowsky-Krieger, 1959). This simple model provides
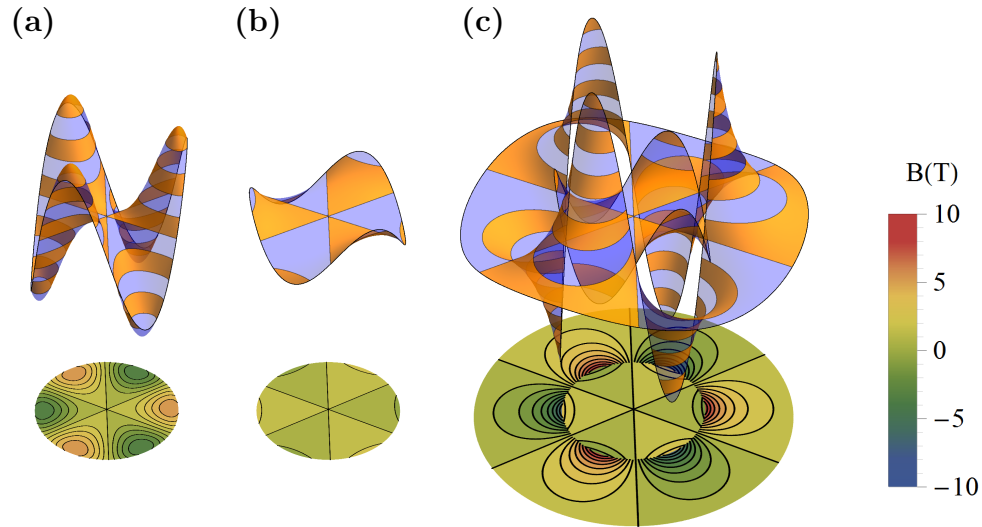
Figure 3.7: Pseudomagnetic fields of a 100 nm radius circular graphene sealed microchamber pressurized to 70 MPA predicted using three different continuum models. The differences in the spatial distribution of the pseudomagnetic field for each model is illustrated using a surface plot with 1 Tesla bands plotted above a contour plot referenced to the color bar on the right. The z scale and the in plane scale are the same for each plot. For each model the pseudomagnetic field at the center is zero. In (a) the strains are determined using a small strain continuation model (Timoshenko and Woinowsky-Krieger, 1959), in (b) Hencky's model (Hencky, 1915) is used, and in (c) the extended Hencky model derived in Chapter 4 is used with a sliding friction of 31.5 MPa. The radial extent of (c) is larger because the extended Hencky model allows the strain to be distributed to the supported graphene.

everything needed to determine the Young's modulus of a thin film based on the pressure induced deflection at the center: A relationship between pressure, Young's modulus, and the center deflection. However, this approximation does not accurately describe the strain profiles and so is not applicable for studying pseudomagnetic fields. Nonetheless, Kyung-Joong Kim *et al.* use a similar model to predict exotic physical phenomena in pressurized circular graphene sealed microchambers (Kim et al., 2011). As shown in Figure 3.7a, when this model is naively used three distinct global maximum and three distinct global minimum are visible with pseudomagnetic fields of nearly 5 Tesla.

In Figure 3.7b Hencky's model is used to predict the pseudomagnetic field. This model is an exact series solution for the large deflection of a circular plate under a uniform vertical load with fixed boundaries. Although more complicated, this model should accurately describe the strains in the system as long as the boundaries are held fixed. The resulting pseudomagnetic fields are noticeably reduced, barely exceeding 1 Tesla. In this case the peaks occur at the boundary of the microchamber.

Finally, in 3.7c the pseudomagnetic fields are calculated using the extended Hencky model that is derived and experimentally confirmed in Chapter 4. In this model the fixed boundary conditions at the edge of the microchamber are relaxed and the supported graphene is allowed to slide against a resistive frictional force. The frictional force for this small of a device at this large of a pressure have not yet been measured experimentally. To get a qualitative idea of the changes resulting from sliding, the dimensionless frictional force found in Chapter 4 by comparison to atomistic modeling of a 6 nm radius microchamber was used. The strain distribution of the suspended graphene is similar to the strains predicted by the Hencky model. The supported graphene, however, is allowed to slide resulting in interesting pseudomagnetic fields. The strain in the supported graphene quickly to decay to zero creating fairly large

9 Tesla pseudomagnetic fields just outside the edge of the microchamber. Further, because the derivative of the strain is not continuous at the edge of the microchamber, neither is the pseudomagnetic field.

Figure 3.8 shows that the pseudomagnetic field predicted by the extended Hencky model agrees well with atomistic simulations. The atomistic simulation was similar to the one described in Section 4.4.2 except it was a smaller, 4 nm radius microchamber modeled over a 10 nm square region at a pressure of 1.2 GPa. The pseudomagnetic field was determined by taking the curl of the strain distribution. To extract the radial dependence of the pseudomagnetic fields the results of the atomistic model were binned into radial elements containing at least 10 atoms and the standard deviation in elements in the bin were taken as the uncertainty in the average. The ϕ dependence was then projected out by fitting each radius to the expected $sin(3\phi)$ form. Finally, the amplitude of these fits was compared to the extended continuum model with the sliding friction chosen to best match the strain profiles of the atomistic model. Considering there are two numeric derivatives involved in determining the pseudomagnetic field from the atomistic simulations, the agreement is impressive.

The example of cylindrical graphene sealed microchambers clearly shows that the validity of predicted pseudomagnetic fields is directly tied to the validity of the strain distribution predicted by the continuum model. One needs to be careful to ensure that the approximations made in solving for the large deflection of the plate do not make the resulting strain distributions inaccurate. Further, one has to be careful to accurately account for how the graphene interacts with its environment.
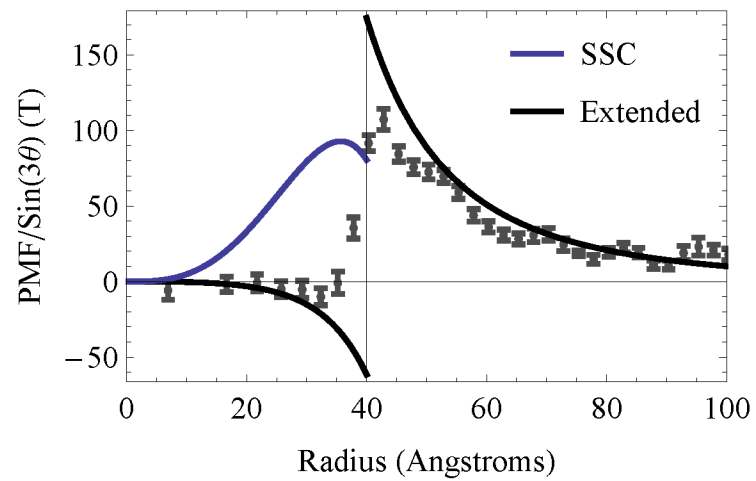
Figure 3.8: Comparison of the radial dependence of the pseudomagnetic field calculated based on an atomistic model (points), extended Hencky model (black line), and the small strain continuation model (blue line) when a pressure of 1.2 GPa is applied to a 6 nm radius cylindrical graphene sealed microchamber. The ϕ dependence was removed by fitting the atomistic data to the expected $sin(3\phi)$ form. There is good agreement between the extended Hencky model and the continuum model.

3.4   Conclusion

The pseudovector potential was derived in full and new, $\boldsymbol{K}_i$ point dependent correc-
tions to the pseudovector potential were found. Even though these correction do not
contribute to the pseudomagnetic field, they are necessary to complete the analogy
between strain-induced momentum shifts and a real vector potential. Additionally,
these shifts are required to accurately determine the position of the Dirac points
and should be taken into account when considering electrical transport over a strain
boundary.

Sealed microchambers were discussed as a test bed for predicting and measuring
pseudomagnetic fields. It was shown that an hour glass microchamber should gener-
ate very large pseudomagnetic fields while also enabling their measurement through
plasmonic enhancement. Finally, the need for accurate continuum modeling was
demonstrated using cylindrical microchambers as an example.

Chapter 4

How graphene slides: Graphene's anomalous macroscopic friction

Graphene is an amazing mechanical system with extreme elasticity (Lee et al., 2008), ultrastrong adhesion (Koenig et al., 2011), and impermeability to gases (Bunch et al., 2008). As a pure two-dimensional material, graphene's interactions with its supporting substrate are unique. Amontons' first law states that macroscopic friction is proportional to the applied load, justified by arguing that increasing the load increases the microscopic contact area between two surfaces (Krim, 1996). Graphene, however, because of its ultrastrong adhesion (Koenig et al., 2011) and low bending rigidity requires no load to achieve nearly perfect conformation to the nanoscale topography of its substrate, especially the commonly used SiO_2 (Stolyarova et al., 2007; Lui et al., 2009; Cullen et al., 2010). Hence, the friction between graphene and SiO_2 might be expected to exhibit an atypical load dependence. The ability to control the thickness of few layer graphene (FLG) at an atomic scale makes it an excellent model system to study the role of thickness and load on friction, which has not previously been quantified or elucidated in detail. To date, most tribological studies of FLG and graphitic materials have measured the interaction between graphene and a scanning probe tip using frictional force microscopy (Dienwiebel et al., 2004; Deng et al., 2012; Lee et al., 2010; Li et al., 2010b; Filleter et al., 2009; Filleter and Bennewitz, 2010; Zhang et al., 2012). These nanoscale measurements have shown interesting effects

such as superlubricity in graphite (Dienwiebel et al., 2004), negative frictional coefficient for chemically modified graphite (Deng et al., 2012), and increasing friction with decreasing FLG thickness (Lee et al., 2010; Li et al., 2010b; Filleter et al., 2009; Filleter and Bennewitz, 2010). Both the negative frictional coefficient and the increasing friction with decreasing thickness have been attributed to the puckering of graphene about the scanning probe tip (Lee et al., 2010; Li et al., 2010b; Deng et al., 2012).

Based on work by the author (Kitt et al., 2013b), this chapter discusses direct measurements of the intrinsic sliding of graphene over a SiO_2 substrate at the macroscopic device scale. Both the load and atomic layer dependence of sliding friction, or the substrate's resistance to graphene sliding are extracted from the data. The system is studied by using variable gas pressure applied to an FLG sealed microchamber as shown in Figure 4.1. The pressure acts as a tunable load, simultaneously pressing the graphene supported around the microchamber hole into the substrate while also forcing the suspended FLG into the microchamber. *In situ* Raman measurements, which can easily measure FLG extensions of 1 nm over 1 μm, show that an annulus of the supported FLG reproducibly slides toward the center of the microchamber. By analyzing the strain response with a newly derived extension of the continuum Hencky model, the load-dependent sliding frictions for mono-, bi-, and tri-layer graphene is extracted. The observed layer dependence exhibits a crossover between bilayer and trilayer; the trilayer sliding friction obeys Amontons' first law, whereas the monolayer and bilayer sliding friction uniquely scales with the inverse of the strain in the graphene. These interesting results are attributed to the interplay between adhesion, in-plane strain and bending rigidity in this two dimensional tribological system. Unlike prior experiments, this technique does not use a scanning probe tip and, thus, the measured sliding friction is intrinsic and not due to the graphene-tip interaction.
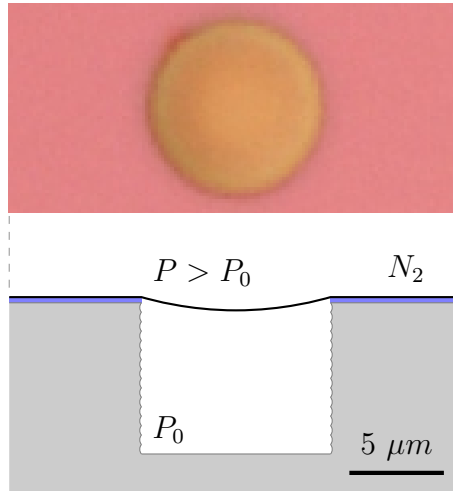
Figure 4.1: Top: An optical image of a trilayer graphene-sealed microchamber. Bottom: Device cross-section schematic showing the microchamber etched 8 μm into the underlying Si substrate and the supported graphene atop the 300 nm of thermal oxide. Pictured to scale is the largest pressure induced deflection of the graphene achieved in any of the analyzed experiments.

A firm understanding of graphene's sliding friction is necessary for a variety of exciting graphene devices such as flexible bistable displays (Bonaccorso et al., 2010), graphene electro-mechanical switches (Milaninia et al., 2009), high quality factor graphene mechanical resonators (Kim and Park, 2009; Bunch et al., 2007; Chen et al., 2009; Barton et al., 2011), and strain engineered devices (Pereira and Castro Neto, 2009) which take advantage of strain induced vector-potentials and pseudomagnetic fields (Castro Neto et al., 2009; Guinea et al., 2010; Kitt et al., 2012; Kitt et al., 2013a) as discussed in Chapter 3. Specifically, as demonstrated in Section 3.3.4, you can not predict pseudomagnetic fields without understanding the unique mechanics of how a floppy, two dimensional system interacts with a rigid three dimensional body.

4.1   Raman G band strain response

Micro-Raman spectroscopy is a powerful tool to measure strain distributions in graphene. The Raman G band measures the zone center, in-plane optical phonons that are degenerate at zero strain (Tuinstra and Koenig, 1970; Ferrari et al., 2006). In the absence of shear strain, the G band shifts according to (Huang et al., 2009)

$$\Delta\omega_G = -\omega_0\gamma(\epsilon_r + \epsilon_t) \pm \frac{1}{2}\beta(\epsilon_r - \epsilon_t) \ , \tag{4.1}$$

where ϵ_r and ϵ_t are the strain in the radial and tangential directions, γ is the Grüneisen parameter and β is the shear deformation potential which details the amount of splitting between the G^+ and G^- bands.

Light scattered by the G^+ and G^- bands has orthogonal linear polarizations (Huang et al., 2009). To isolate the individual peaks, spectra are often measured using linearly polarized light. Here, however, spectra are measured with circularly polarized light unless otherwise noted. This allows more data to be acquired because the G^+ and G^- bands are measured simultaneously. Figure 4.2 shows experimental verification that the spectra taken using circular polarized light matches the sum of the G^+ and G^- bands. Measurements were taken at various $\rho = r/R$, where r is the distance from the center of the microchamber and R is the radius of the microchamber. The G^+ and G^- bands were measured in the usual way by setting the incident excitation along the radial strain direction and measuring the emitted spectra as a function of emission polarization. By summing over the spectra taken with emitted polarization varied from -90 to 90 degrees in 20 degree steps, a spectra with equal contributions from G^+ and G^- is created. As shown in Figure 4.2, these derived spectra match the single spectra taken with circularly polarized light. This verifies

that spectra measured with circularly polarized represent both the G^+ and G^- bands.

The local Raman response is measured inside an optically accessible pressure chamber with a focused laser beam while variable pressures up to 0.80 MPa are used to push the FLG into the microchamber. Raman spectra are excited using the 514 nm line of an argon ion laser and collected using a Renishaw spectrometer with an 1800 lines/mm grating and a 63X, 0.7 NA, cover slip corrected objective. The laser power in the pressure chamber was kept below 0.5 mW to avoid sample heating. Optical access into the pressure chamber is through a 1 mm BK7 window. The beam waist of the focused laser was measured to be 0.81 ± 0.01 μm by scanning a gold pad under the laser as shown in Figure 4.3.

4.2   Experimental Design

A cross-section of one of the microchambers sealed with mechanically exfoliated FLG is depicted in Figure 4.1. Microchambers are fabricated using standard optical lithographic methods to define holes ranging from 1 to 5 μm in radii, reactive ion etching to etch through the 300 nm thermal oxide layer, and deep reactive ion etching to etch roughly 8 μm into the underlying silicon layer. Before the graphene is mechanically exfoliated to seal the microchambers, the substrate is oxygen plasma ashed for 10 minutes at 300 sccm and 500 Watts to ensure the substrate is cleaned of any residues. It is important to note that different surface treatments may yield different sliding frictions providing a new degree of freedom in device engineering. The number of graphene layers sealing each device was determined using Raman spectroscopy (Ferrari et al., 2006) and optical contrast (Blake et al., 2007; Casiraghi et al., 2007).

The large microchamber depth of $\sim$ 8 μm is 10 times the largest FLG deflection of 700 nm. This allows for the changes in internal pressure as the microchamber shrinks
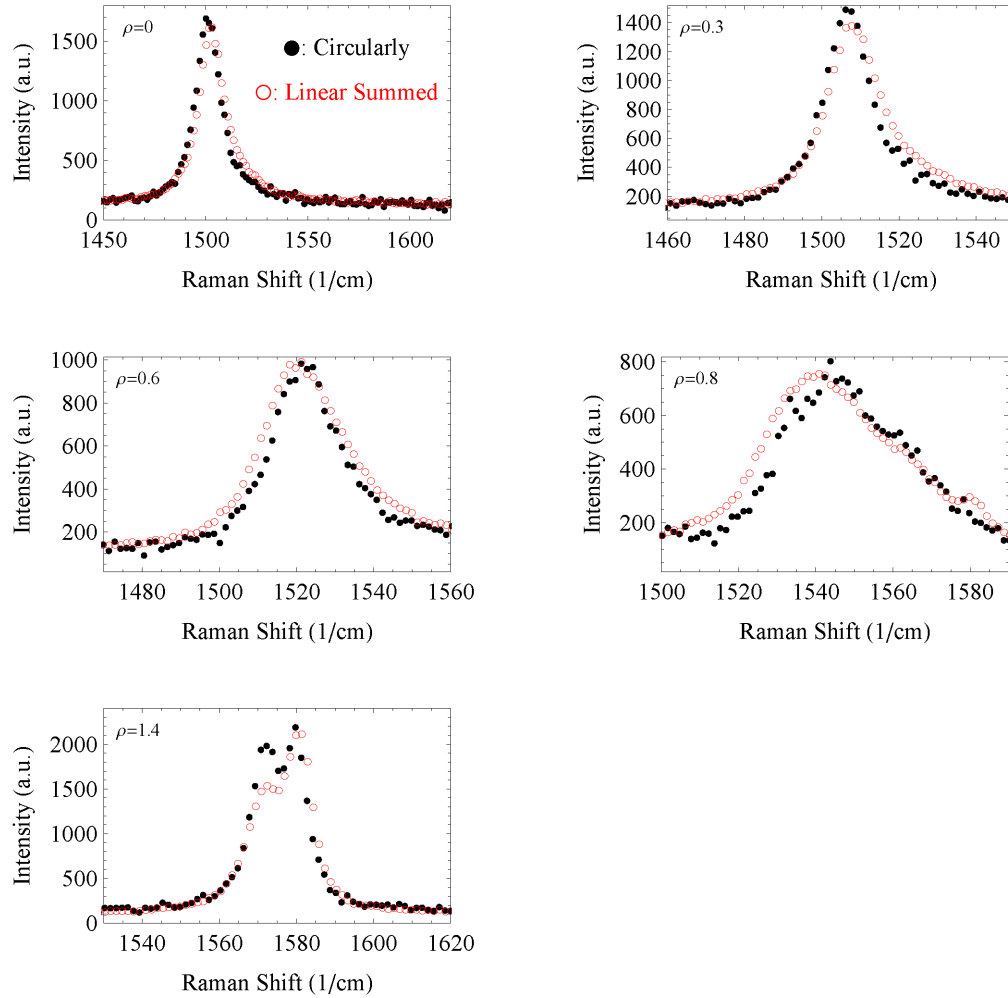
Figure 4.2: Comparison of Raman spectra measured using circularly and linearly polarized light. Measurements were taken at the labeled values of ρ on a R=5 μm graphene sealed microchamber under 0.80 MPa of applied absolute pressure. The red dots are the sum of spectra taken with outgoing polarizations varied between -90 to 90 degrees in 20 degree steps while the excitation is held in the $\hat{x}$ direction. The spectra taken with circularly polarized light (black dots) reproduces the summed polarization data. Spectra are scaled to match intensities.
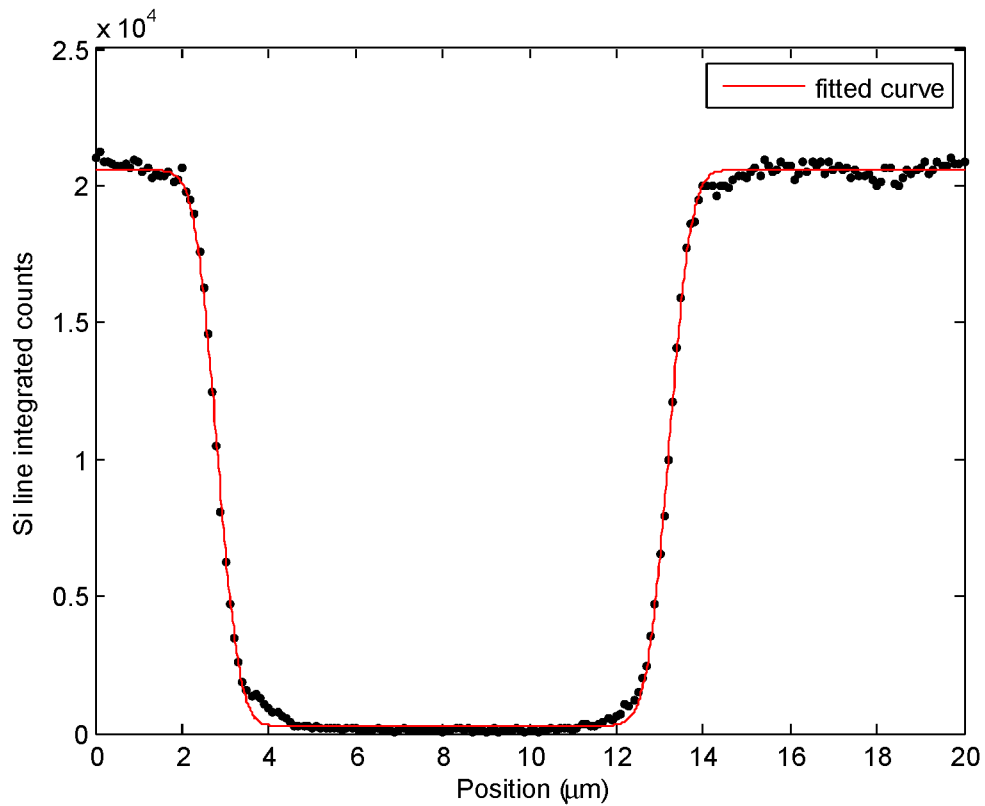
Figure 4.3: Determination of the beam waist of the focused laser in the pressure chamber by scanning a sample with a gold pad under the focused beam while measuring the Si Raman line intensity. As the sharp edge of the gold pad moves under the laser, the Si line is blocked giving a measure of the beam size. Fitting the signal to an error function gives a beam waist of $0.81 \pm 0.01 \ \mu m$.

with pressure to be ignored. It also enables longer measurement times because of slower leak-out rates through the silicon substrate.

Two complementary Raman measurements are performed *in situ* to fully characterize the strain distributions. First, as the absolute applied pressure is varied between atmospheric pressure (0.10 MPa) and 0.80 MPa, Raman spectra at the center of the microchamber are recorded. Also, at selected pressures, Raman G band line scans with 0.5 μm point spacing are taken across the microchamber and the supported graphene on the surrounding substrate. The former is used to determine the pressure trapped inside the microchamber while the latter is used to determine the spatial distribution of the strain. In conjunction with low force ($\approx 1\ nN$) contact mode atomic force microscopy (AFM), the Raman spectra taken at the center of the microchamber reveal interesting ambient pressure behavior exhibited by the graphene sealed microchambers.

4.2.1   Pressure trapped in microchambers

After exfoliating graphene over our microchambers, we observe two different behaviors. For roughly half of the devices the pressure inside of the microchamber was greater than one atmosphere, as shown in the left side (a) of Figure 4.4. Here, both the ambient pressure AFM and pressure dependent Raman measurements indicate that the pressure inside of the microchamber is greater than ambient. The topographic image shows the graphene bulging out and the Raman G band response demonstrates that a non-zero gauge pressure is necessary for the G band to reach its greatest, or least strained, value. The Raman data can be fit using the $p^{2/3}$ dependence predicted by the Hencky model, a continuum model which describes a circular thin plate with fixed boundaries (Hencky, 1915). This model is discussed in more detail in Section 4.4. Fitting to the $p^{2/3}$ dependence provides the internal pressure

and unstrained G band position.

In the second half of the devices, the pressure inside the microchamber was an atmosphere, within measurement uncertainty, as shown on the right side (b) of Figure 4.4. The AFM topography shows that the graphene is flat across the aperture indicating the internal pressure matches the ambient pressure. The topography also shows that graphene is stuck to the walls of the microchamber for an AFM determined distance of roughly 7 nm. Additionally, the Raman G band response in these devices shows interesting small strain behavior with increasing pressure. At atmospheric pressure the G band is already red shifted due to pre-strain. Increasing the gauge pressure to ~ 0.1 MPa causes a slower than expected downshift in the G band position. However, when the gauge pressure is increased beyond 0.1 MPa, the shift rate converges to the expected trend, $P^{2/3}$, and remains on this trend when the pressure is reduced back to atmospheric pressure. This is consistent with the FLG unsticking from the walls as pressure is applied and remaining unstuck when the pressure returns to ambient pressure. Values for friction are extracted from data taken at 0.17 MPa and above, well beyond the pressure domain where side wall sticking effects are observed. For devices that behave in this way, the internal pressure is taken to be an atmosphere and the unstrained G band position is set as the G band position upon completing the pressure cycle.

Other groups have observed similar snap-to-sidewall behavior (Lee et al., 2008; Bunch et al., 2008). Bunch and Dunn noted that the AFM measured distance over which FLG snaps to sidewalls may be overestimated (Bunch and Dunn, 2012). This position is supported by our measurements where we see that strain measured with AFM topography is a factor of 2.5 greater than strain measured with Raman: For a 3 μm hole, a change in radius of 7 nm should generate 0.2% strain whereas a Raman shift of -5 cm^{-1} indicates a strain of 0.08%. Additionally, side wall sticking may explain

(a) $P_0 > P_a$ **(b)** Snapped to side wall
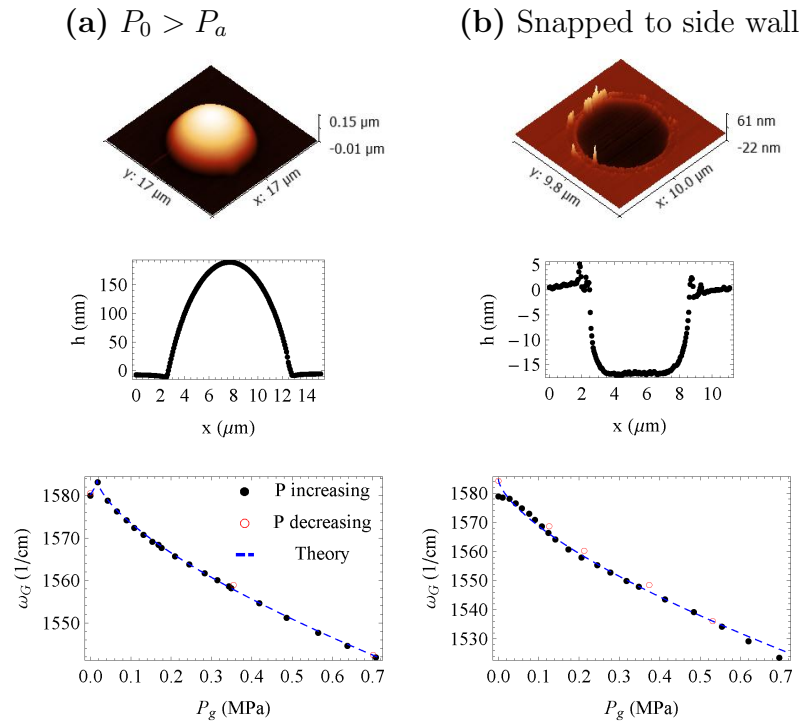
Figure 4.4: The two characteristic ambient pressure behaviors of FLG sealed microchambers: Bubbled out (a) and snapped to the sidewall (b) measured on a 5 μm radius trilayer sealed microchamber and 3 μm radius monolayer sealed microchamber respectively. The first row shows low contact force ($\approx$ 1 nN), ambient pressure AFM topographies and line cuts. The second row shows the pressure dependence of the single frequency Lorentzian fits to Raman spectra taken at the center of the microchamber.

the small Young's Modulus measured by Lee *et al.* using a similar measurement over the a 0.1 MPa pressure range (Lee et al., 2012).

4.3 Qualitative results

Raman line scans over pressurized microchambers show that the supported graphene around the microchamber has slid inward toward the center. Figure 4.5 shows the center frequency of single Lorentzian fits to the G band as a function of position across a 6 μm diameter monolayer covered graphene sealed microchamber with applied absolute pressures of 0.45 and 0.80 MPa during three separate pressure cycles from atmospheric to 0.80 MPa. As expected, as the suspended graphene is pushed down into the microchamber, the G band red shifts or softens from its unstrained value. Unexpectedly, the G band of the supported graphene *outside* the edge of the microchamber also shows softening, and thus significant strain. The observed softening decreases with the distance from the edge of the microchamber until the G band returns to its unstrained energy. This strain is real; the G band red shift cannot be attributed to the averaging over the finite spot size of the beam because the measured downshifts persist much further from the edge of the microchamber than the 0.83 μm beam waist. As the applied pressure increases, more strain is distributed outside of the microchamber causing both a larger redshift and a larger region over which the strain is distributed. The strain distributed outside of the microchamber's edge is a clear indicator that the graphene is not rigidly fixed to the substrate outside of the microchamber. Instead of a line force acting at the circumference of the microchamber to fix the graphene at the edge, there must be a distributed sliding frictional force, f, acting between the graphene and the substrate.

The strain distribution both inside and outside the microchamber is reproducible,

stable, and azimuthally symmetric. The four 0.45 MPa line scans in Figure 4.5 include one line scan in the x direction for each of the first two pressure cycles and a line scan from both the x and y direction during the third pressure cycle. The five 0.80 MPa line scans include one line scan in the x direction from the first pressure cycle, two sequential line scans in the x direction which took 35 minutes each from the second pressure cycle, and a line scan from both the x and y direction during the third pressure cycle. Other than the development of a dimple at the center of the microchamber, the spectra and G band shifts are nearly identical. This dimple is the result of laser deposition of dirt at the center of microchamber due to tens of hours of high pressure resolution, single point measurements. An SEM image of the schmutz dimple is shown in the inset. This dirt seems to stabilize the graphene underneath, reducing the strain in its local vicinity. Similar reproducibility is observed in each of the eight measured microchambers which have radii between 1.2 and 5 μm and are covered with from one to three layers.

To determine the nature of the strain outside of the microchamber, Raman spectra in a region 2 μm outside the edge of a 5 μm radius monolayer covered microchamber were analyzed in detail using linearly polarized light. As shown in Figure 4.6, there are two discrete peaks in the spectra at 1570.9 cm^{-1} and 1581.3 cm^{-1} which are tuned on and off by rotating the analyzer on the outgoing light. The polarization dependence of the integrated peak areas is consistent with the orthogonality of the G^+ and G^- peaks (Huang et al., 2009). The peak positions indicate a tensile radial strain of 0.6% and a compressive tangential strain of -0.3% at this location. The compressive tangential strain is expected: When an annulus of the supported FLG is pulled inward, its circumference shrinks and, if the adhesion energy between FLG and its substrate is large enough to suppress out-of-plane wrinkling, this shrinkage causes compressive tangential strain.
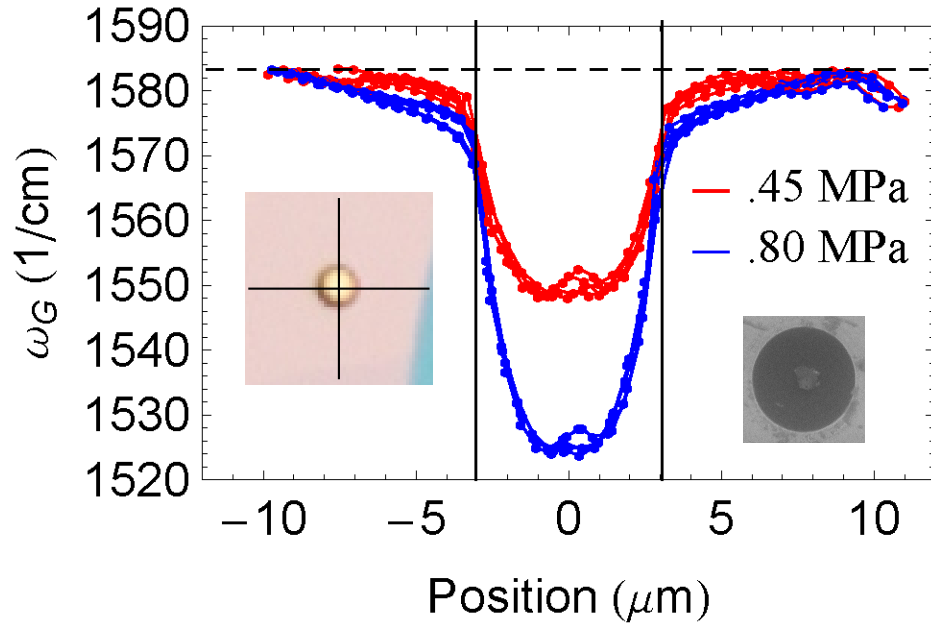
Figure 4.5: Qualitative observations of graphene sliding. The frequency shift of the Raman G band is shown as a function of position for four line scans taken at 0.45 MPa and five line scans taken at 0.80 MPa from 3 separate pressure cycles scanned across a single 6 μm diameter monolayer sealed microchamber. Each point represents the position of the center of a single Lorentzian fit to the Raman spectra at that position. The solid vertical black lines are positioned at the edges of the microchamber and the dashed horizontal line indicate the zero strain position. Data points are separated by 0.5 μm; the focused beam has a waist of 0.81 μm. Inset left is an optical image of the microchamber with line scan direction indicated. The bottom right inset is an SEM image of the device taken after all of the data was acquired.
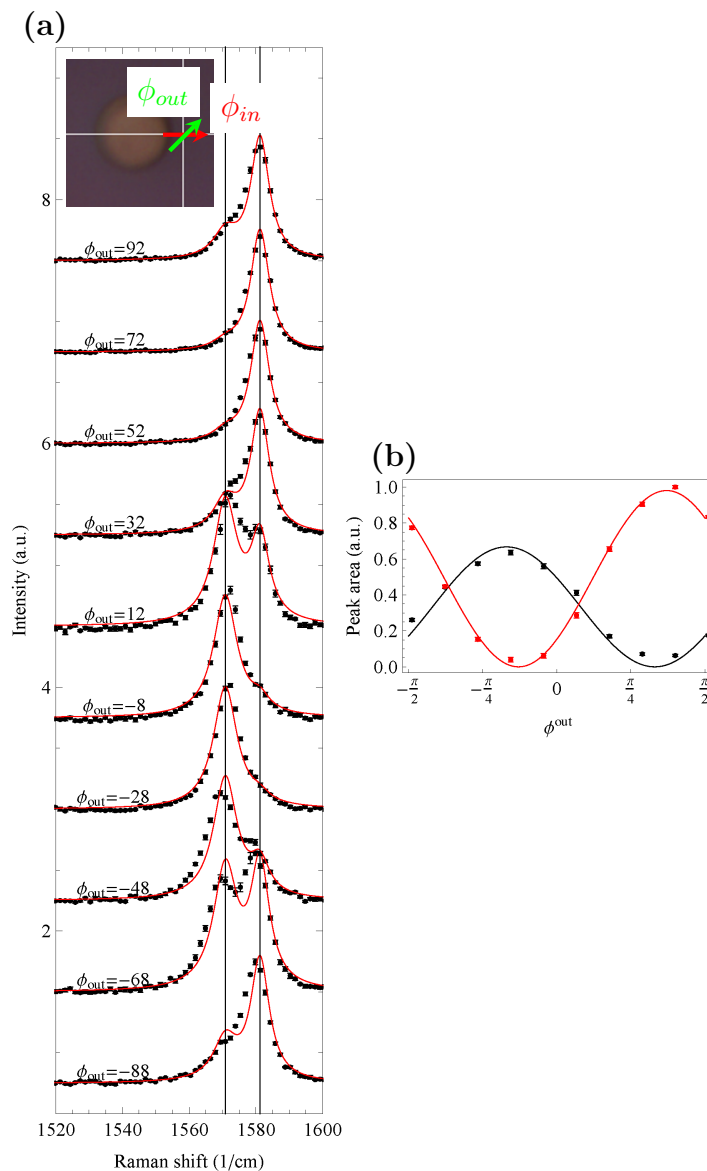
Figure 4.6: (a) Linearly polarized Raman spectra of supported graphene taken 2 μm outside a 5 μm radius graphene sealed microchamber pressurized to 0.80 MPa absolute pressure with the incident light polarized in the $\hat{x}$ direction ($\phi = 0$) and the outgoing light linearly analyzed at the labeled angle. The areas under the strain split 1570.9 cm^{-1} and 1581.3 cm^{-1} peaks are tuned on and off as a function of outgoing analyzer and are fit with π out-of-phase sine squared functions in (b).

In the Raman and AFM experiments there is no evidence of the FLG wrinkling to relieve compressive tangential strain. Shown in Figure 4.7 is a partial Raman map of this 5 μm radius monolayer covered microchamber at 0.80 MPa of applied pressure. To generate the Raman maps Raman spectra were taken at each spatial location on the map. Each spectra was fit with Lorentzians of energies ω^+ and ω^- and the best fit energies were plotted as a function of the spatial location where the spectra was taken. This two Lorentzian fit matches the characteristic two peak shape of the supported graphene shown in Figure 4.2 for $\rho = 1.4$. Both maps in Figure 4.7 were scaled to emphasize the shifts in the supported graphene peak positions. As a result, the more highly strained suspended graphene appears black in the maps. The ω^- Raman map, (a), shows very high radial symmetry while the ω^+ map, (b), has slightly reduced symmetry. At the highest point on the microchamber, there is a variation of around four wavenumbers in the ω^+ map which could be due to small variations in local adhesion or could be due to nonuniform doping. The degree of radial symmetry exhibited by both of these Raman maps is a strong indicator that the supported graphene is not wrinkling. Since these Raman maps are for the microchamber with the largest diameter and thinnest graphene thickness at the highest applied pressure, the compressive strains are the highest of any of the measured FLG sealed microchambers. Thus, wrinkling in all other measured microchambers which have lower compressive strain can be precluded.

4.4 Continuum model of strain distributions

In this section, a continuum model to extract the sliding friction, f, from the Raman determined strain distributions is developed. In 1915, Hencky proposed a continuum model for the non-linear pressure induced deflection of a thin circular plate with fixed
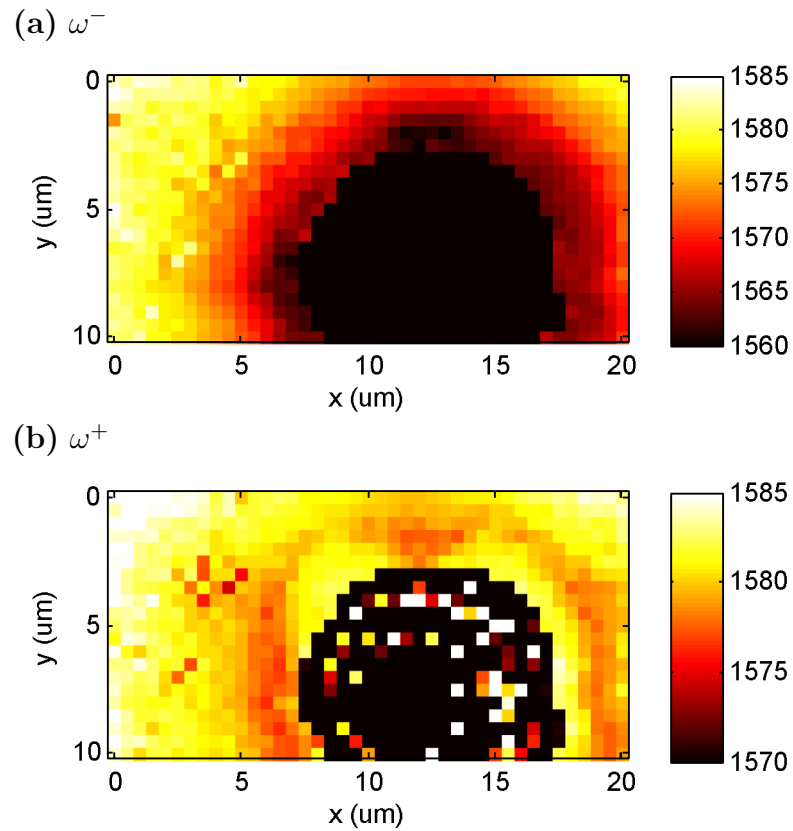
Figure 4.7: Two frequency fit Raman map of a pressurized graphene sealed microchamber. The position of the the ω^+ peak (a) and ω^- peak (b) are plotted for a 5 μm radius graphene sealed microchamber pressurized to 0.80 MPa. Color scale are set to emphasize the peak shifts experienced by the supported graphene. The speckles in (b) appear because the suspended graphene spectra are not fit well by two Lorentzians. Both maps show a high degree of radial symmetry inconsistent with the formation of wrinkles.

boundary conditions (Hencky, 1915; Fichter, 1997). This model has been successfully used to describe a variety of systems including inflatable membrane mirrors (Meinel and Meinel, 2000), electrostatic actuators for micro gas pumps (Zhang and Wang, 2011), and the topography of FLG bulging from sealed microchambers (Koenig et al., 2011). However, the fixed boundary conditions assumed by this model preclude its application to the strain distributions observed here. The fixed boundary conditions can be relaxed by matching the radial and tangential stresses inside the hole, derived from Hencky's model before the application of boundary conditions, to the radial and tangential stresses of the supported material outside of the hole found by including a sliding friction, f, acting against the radial displacement. The stresses and, using Hooke's law, the strains, are then fully determined as a function of $\frac{\Delta P^2 E_{2D}}{f^3 R}$ where R is the radius of the microchamber measured by AFM, ΔP is the differential pressure, and E_{2D} is the 2D Young's modulus of FLG taken to be $n \times 340 \ N/m$ where n is the number of layers (Lee et al., 2008; Koenig et al., 2011).

Figure 4.8 compares the radial and tangential strains from the standard Hencky solution, the extended Hencky model derived here, and an atomistic, molecular dynamics model. The solid lines of the extended model demonstrate the desired features; strain is distributed *outside* of the hole with compressive tangential and tensile radial strain. The strain distribution depends on the friction as expected: At constant pressure and radius, a greater sliding friction holds the graphene more firmly to the substrate surrounding the microchamber, and thereby increases ϵ_c, the strain in the center of the microchamber, while also reducing ρ_0, the largest radial distance that the strain acts outside of the hole. The extended model, with f=520 MPa, is in good agreement with the dots in Figure 4.8 that are the results of an atomistic molecular dynamics simulation of a 6 nm radius microchamber under 500 MPa of pressure performed using the open source simulation package LAMMPS (Lammps,
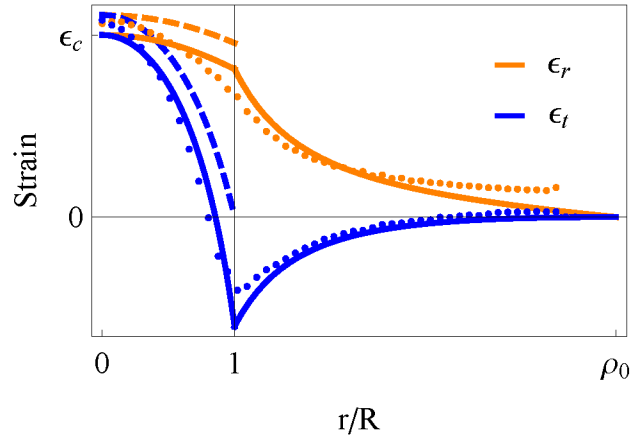
Figure 4.8: Theoretical strains in FLG sealed microchambers. Comparisons of the radial and tangential strains predicted by Hencky's model (dashed), the extended Hencky model that includes strain outside the microchamber for a sliding friction of f=520 MPa (solid), and atomistic simulations of a 6 nm radius microchamber with 500 MPa of applied pressure (dots). The extended Hencky model used to extract friction agrees very well with the atomistic model.

2012; Plimpton, 1995) developed at Sandia National Labs.

This work represents the first time that Hencky's model has been generalized to allow strain to be distributed outside of the microchamber's edge. The derivations provides a framework for including the sliding of graphene over a rigid substrate in a continuum model. This should be useful in applications such as the strain engineering of pseudomagnetic fields. For those interested, a full derivation of the extended Hencky model as well as a detailed description of the atomistic modeling is included in the next sections.

4.4.1 Detailed derivation of the extended Hencky model

To derive the extended Hencky model the general forms of the stress inside and outside of the hole will be derived, and then the boundary condition will be determined and applied. The resulting solution will be a function of the dimensionless loading parameter, $q = \frac{\Delta PR}{E_{2D}}$, and the dimensionless friction coefficient $F = Rf/E_{2D}$ in the combination $q^{2/3}/F$. This means that large dimensionless loading, $q^{2/3}$, causes the same effects as small friction, F; pushing hard has the same effect as sliding easily. A simple analytic relationship does not exist between $q^{2/3}/F$ and the two parameters which define the shape of the strain profile: the distance over which the strain spreads outside of the hole, ρ_0, and the coefficient of stress at the center of the hole, b_0. However, these can be easily solved for analytically.

Throughout this section graphene is treated in the continuum limit as a thin plate: A solid which is much thinner in one dimension than the other two. Assuming that there is no shear, the stress-strain relationship for the thin plate is the same inside and outside the hole (Landau and Lifshitz, 1986)

$$\epsilon_r = \sigma_r - \nu\sigma_t \tag{4.2}$$

$$\epsilon_t = \sigma_t - \nu\sigma_r \ , \tag{4.3}$$

where ν is the Poisson Ratio and σ_r and σ_t are the dimensionless radial and tangential stresses given by the stress divided by the effective 3D Young's modulus ($E_{3D} = E_{2D}/t$ where t is the thickness).

Both the strain-displacement and the governing equations, however, depend on the region of interest. For the suspended material, the plate flexes down into the hole

as pressure is applied. The resulting strain-displacement relationships are

$$\epsilon_r^i = \frac{dU}{d\rho} + \frac{1}{2}(\frac{dW}{d\rho})^2 \tag{4.4}$$

$$\epsilon_t^i = \frac{U}{\rho} \ , \tag{4.5}$$

where U is the dimensionless radial deflection, W is the dimensionless out of plane deflection, and ρ is the dimensionless radius, all of which are made dimensionless by dividing by the radius of the hole. The governing equations inside the hole are calculated by balancing the forces on a radial element. The stresses and pressure acting on such an element are shown in Figure 4.9. Using the area of the radial element $(rdrd\theta)$ to convert the pressure to a force, and the cross sectional area to convert the strains into forces results in the two governing equations

$$\sigma_t^i = \frac{d}{d\rho}(\rho\sigma_r^i) \tag{4.6}$$

$$\sigma_r^i \frac{dW}{d\rho} = -\rho\frac{q}{2} \ . \tag{4.7}$$

the first from radial equilibrium and the second from lateral equilibrium. These six equations can be combined to form a single differential equation for σ_r

$$\frac{1}{8}\rho q^2 + (\sigma_r^i)^2 \frac{d}{d\rho}[\sigma_r^i + \frac{d}{d\rho}(\rho\sigma_r^i)] = 0 \ . \tag{4.8}$$

This is most easily found by using Equation 4.6 and then Equation 4.7 in the combination of Equations: $[(4.4) \rightarrow (4.2)] - \frac{d}{d\rho}\rho[(4.5) \rightarrow (4.3)]$. Once this equation is used to solve for σ_r, Equations 4.6, 4.2, and 4.3 allow the easy determination of σ_t, ϵ_r, and ϵ_t. Since there is no analytic solution to this differential equation, so, following Hencky's solution, a series expansion of the radial stress even in powers of ρ to match

Figure 4.9: Forces acting on a suspended section ($\rho < 1$) of a pressurized graphene sealed microchamber. Depicted are the stresses, $N_r = E_{3D}\sigma_r$ and $N_t = E_{3D}\sigma_t$, and pressure, P, which act on a radial area element as viewed from the top and side.

symmetry is assumed

$$\sigma_r^i = \frac{1}{4}q^{2/3}\sum_{n=0}^{\infty}b_{2n}\rho^{2n} \ . \tag{4.9}$$

When used in eqn. 4.8 all of the higher order coefficients are determined in terms of one free parameter, b_0, the stress coefficient at the center of the hole. To this point the derivation has not deviated from Hencky's original work. However, instead of continuing forward to determine the value of b_0 by requiring that there is no radial deflection at the edge of the hole, b_0 will be left as a free parameter to match to the strain outside of the hole, which is now derive.

Outside of the hole, the plate is constrained to move in the x-y plane, radial symmetry is preserved, and friction is present. The stress-strain relationships (eqns. 4.2 and 4.3) are for a thin plate with no shear, and thus, apply equally well outside the hole as inside. The strain displacement relationships are based on the geometry of a general radially symmetric differential element. The only change that needs to

be made to these is the elimination of the out of plane motion,

$$\epsilon_r^o = \frac{dU}{d\rho} \tag{4.10}$$

$$\epsilon_t^o = \frac{U}{\rho} \ . \tag{4.11}$$

For sufficiently negative ϵ_t, the plate is expected to buckle out-of-plane, forming wrinkles. However, in the experimental regime there is no evidence for these effects. The forces acting on the plate are different inside and outside the hole, and thus, so are the governing equations. The stresses and forces acting on the graphene outside of the hole are shown in Figure 4.10. The interaction between the plate and its underlying substrate is included via the frictional force per unit area, f, which is pointed to oppose the radial stresses outside of the hole. If there were a component of friction acting against the tangential strain, it would go as $d\theta^2$ rendering it negligible. One power of $d\theta$ from the resultant and the other from the area element. Care needs to be taken in this mathematical treatment because this friction term does not turn off when the stress goes to zero. Instead, it works in positive feedback amplifying the stress. As a result, the stresses are only physical until they decay to zero at a position ρ_0. The governing equation outside the hole is then

$$\sigma_t^o = \frac{d}{d\rho}(\rho\sigma_r^o) + F\rho \ . \tag{4.12}$$

Again these equations can be combined to form a single differential equation for σ_r. The easiest way to do this is by using Equation 4.12 twice in the combination of Equations: $[(4.10) \rightarrow (4.2)] - \frac{d}{d\rho}\rho[(4.11) \rightarrow (4.3)]$. The result is

$$\frac{d}{d\rho}[\sigma_r^o + \frac{d}{d\rho}(\rho\sigma_r^o)] = -(2+\nu)F \ . \tag{4.13}$$
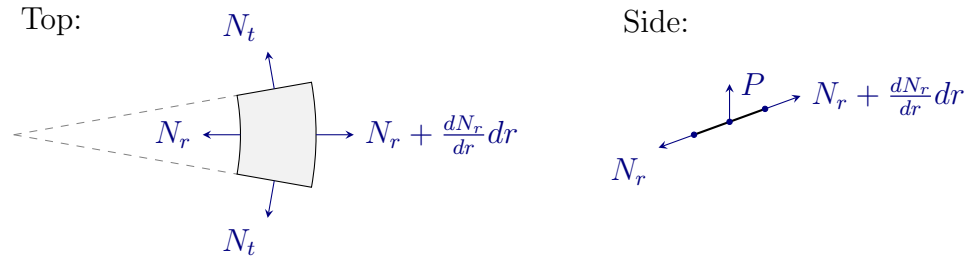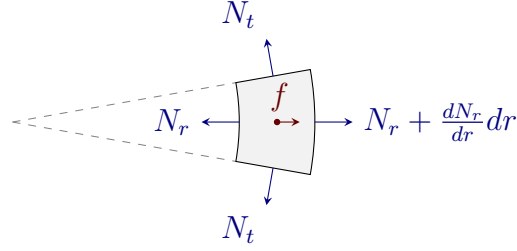
Figure 4.10: Force acting on a supported section ($\rho > 1$) of a pressurized graphene sealed microchamber. Depicted are the stresses, $N_r = E_{3D}\sigma_r$ and $N_t = E_{3D}\sigma_t$, and friction, f, which act on a radial area element.

Unlike the situation for $\rho < 1$, this equation can be solved exactly. The general result for the radial and tangential stresses are

$$\sigma_r^o = (2+\nu)F(-\frac{\rho}{3} - \frac{c_2}{2\rho^2}) + c_1 \tag{4.14}$$

$$\sigma_t^o = (2+\nu)F(-\rho\frac{1+2\nu}{3(2+\nu)} + \frac{c_2}{2\rho^2}) + c_1 \, , \tag{4.15}$$

where the tangential stress was solved for using Equation 4.12. To reduce the number of free coefficients, the radial and tangential strains are both forced to come to zero at the position ρ_0. This natural restriction imposes a limit on the region where the theory gives physical results. For $\rho > \rho_0$, the mathematical friction persists even though there is no stress, yielding unphysical results. For these regions, the stresses are taken to be zero. Applying this restriction gives $c_2 = \rho_0^3\frac{\nu-1}{3(2+\nu)}$ and $c_1 = \rho_0\frac{1+\nu}{2}F$. This defines in closed form the strains for $\rho > 1$ as a function of one free parameter, ρ_0.

Next, the boundary condition for the stresses at the edge of the hole will be determined so that the stresses can be matched across the boundary. The stress is

related to the force per unit area through a divergence operation

$$F_i = \frac{\partial N_{ik}}{\partial x_k} \ , \tag{4.16}$$

where F_i is the applied force per unit volume in the i direction, N_{ik} is the strain tensor, and repeated indices are summed over. Integrating the equations and using the divergence theorem gives

$$\int_V F_i \ dV = \oint_S \sigma_{ik} \ df_k \ . \tag{4.17}$$

Hence, the total force acting on a volume entity is given by the surface integral of the stress. A symmeterized volume element that spans the edge of the hole is shown in Figure 4.11. In the limit that the width of the volume element, ϵ, goes to zero the contributions from the surface forces, f and P, also go to zero and so must the surface integral of the stresses. This would not be the case if these were 1D edge forces. The undrawn, tangential stresses also go to zero since the cross section that they act on, ϵt where t is the thickness, goes to zero as well. Thus, the remaining stresses must be equal,

$$N_r^i = N_r^o \ . \tag{4.18}$$

The boundary condition on the tangential stress is found by the requirement that the radial displacement, U, must be continuous. If it were not, the material on one side of the discontinuity would separate from the material on the other side leaving a gap. If U is continuous, so must ϵ_t be by eqns. 4.5 and 4.11. Finally, if ϵ_t and N_r are continuous, so must N_t be by equation 4.3. This proves that the radial and tangential stresses must be continuous over the edge of the hole.

All of the necessary relationships have now been derived. The series solution for
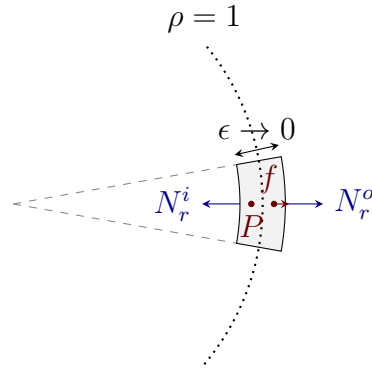
Figure 4.11: The boundary condition at the edge of the microchamber is determined by the stresses and forces acting on a thin, symmetrized volume element which spans the edge of the hole. The tangential strains inside and outside are ignored because their contribution goes to zero as the width of the element, ϵ, goes to zero. P is the pressure which acts out of plane.

the stresses for $\rho < 1$ as a function of the dimensionless loading, q, are known with b_0, the stress at the center, a free parameter. Similarly, the closed form solution for the stresses for $\rho > 1$ as a function of the dimensionless friction, F, have been found, with ρ_0, the furthest distance the stress spreads, as a free parameter. The derived boundary conditions at $\rho = 1$ can now be applied

$$\sigma_r^i(\rho = 1) = \sigma_r^o(\rho = 1)$$
$$\sigma_t^i(\rho = 1) = \sigma_t^o(\rho = 1) \ . \tag{4.19}$$

This sets the value of ρ_0 and b_0 in terms of $q^{2/3}/F$. Regrettably, the series form of the solution inside of the hole makes the presentation of an exact expression for ρ_0 and b_0 impossible. Numerical solutions for the values of ρ_0 and b_0 are presented in Figures 4.12 for graphite's Poisson ratio of 0.165 (Blakslee et al., 1970). As the

friction increases or the dimensionless loading coefficient decreases, $q^{2/3}/F$ decreases, and ρ_0 decreases toward unity, indicating that no strain distribution outside of the hole. At the same time b_0 increases toward the limiting value of 1.66, the result for the original Hencky model which assumes perfectly fixed boundary conditions at the edge of the hole.

This completes the derivation of the extended Hencky model. The shape of the strain distributions shown in Figure 4.8 has been determined along with the pressure, friction, radius, and layer thickness dependencies shown in Figure 4.12.

4.4.2   Detailed description of the Atomistic model

In this section the atomistic model used to verify the extended Hencky continuum model is discussed. Classical molecular dynamics simulations (MD) were performed using open source simulation package LAMMPS (Lammps, 2012; Plimpton, 1995) developed at Sandia National Labs. The model used argon gas to compress a graphene monolayer that lies atop an amorphous silicon dioxide substrate, as illustrated in Figure 4.13. The substrate had dimensions 46 x 46 x 3 nm with a 6 nm radius hole in the center. A circular graphene monolayer with radius 22 nm was placed on top of the hole in the substrate and argon atoms were randomly distributed within the simulation box after relaxation of the graphene-substrate system. There were 562,110 atoms in total, with the simulation run in parallel for maximum computational efficiency.

The covalent carbon bonds were modeled using the AIREBO (Stuart et al., 2000) potential, which has been shown to have good accuracy in describing hydrocarbon systems (Qi et al., 2010; Zhao and Aluru, 2010). The Tersoff (Tersoff, 1988) potential was utilized for the Si-Si, Si-O and O-O interactions, while a Lenard-Jones potential was used for all other interactions with a cutoff distance of 8 Å and the corresponding interaction parameters chosen as follows: ϵ_{Ar-Ar}=0.0104 eV, σ_{Ar-Ar}=3.405
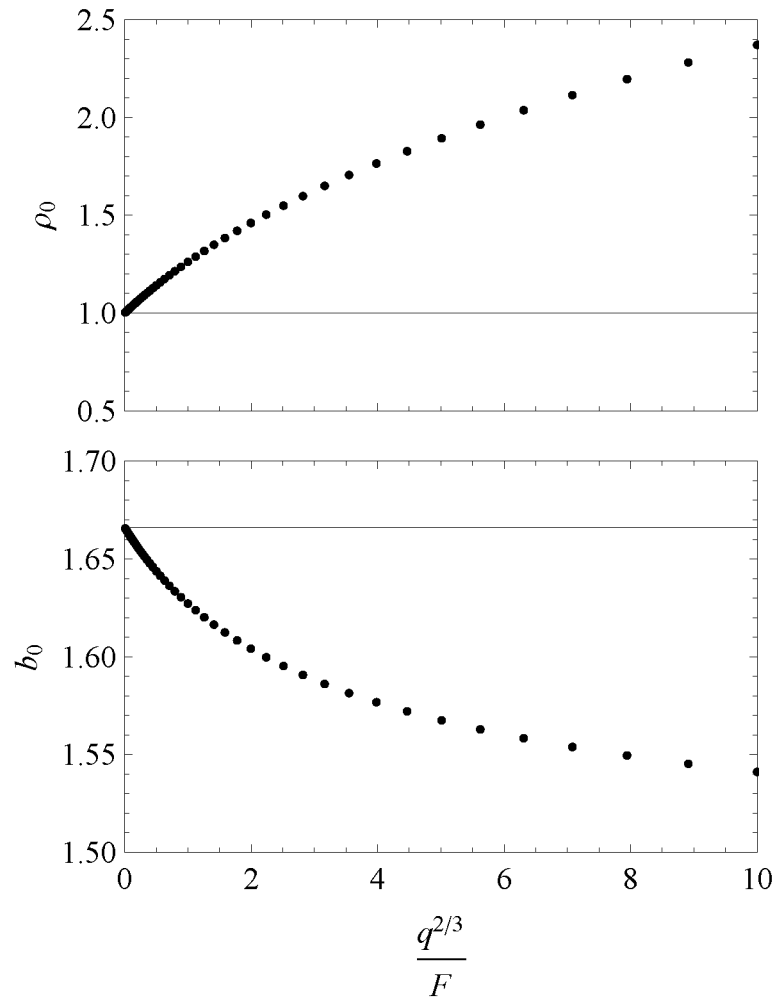
Figure 4.12: Numerical solutions for the values of ρ_0 and b_0, the furthest normalized radii that the strain reaches and the coefficient for the strain at the center of the hole, respectively. Note the large friction convergence to the values of the original Hencky model, $\rho_0 = 1$ and $b_0 = 1.66$.
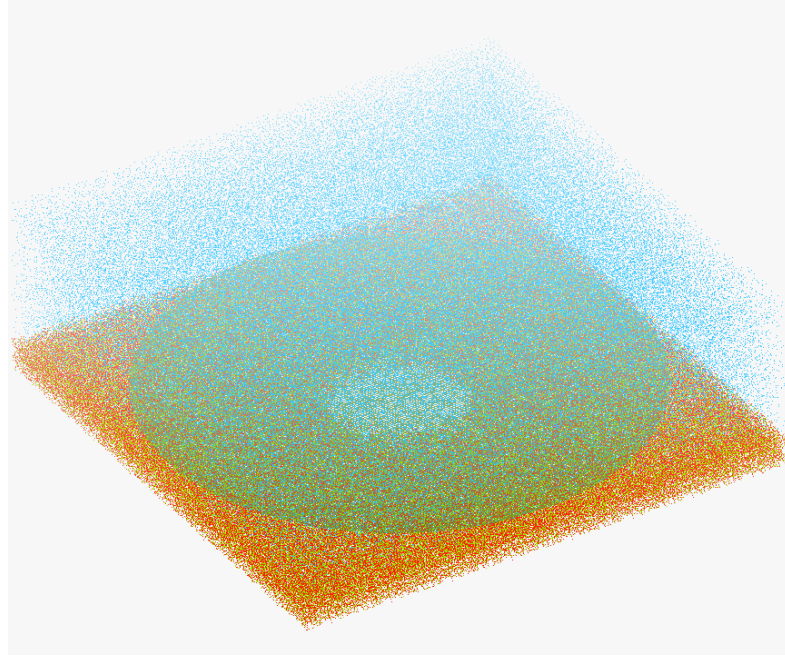
Figure 4.13:   Schematic diagram of the atomistic simulation of the pressurized graphene sealed microchamber including (from bottom to top amorphous SiO_2 substrate (red and orange atoms), circular graphene monolayer (brown atoms) and argon gas (cyan atoms).Visualization was performed using Visual Molecular Dynamics (Humphrey et al., 1996).

Å(Rytkonen et al., 1998); ϵ_{Ar-C}=0.0123 eV, σ_{Ar-C}=3.573 Å(Tuzun et al., 1996); ϵ_{Ar-Si}=0.0028 eV, σ_{Ar-Si}=3.778 Å(Li et al., 2010a); ϵ_{Ar-O}=0.0058 eV, σ_{Ar-O}=3.3075 Å(Everitt and Skinner, 1999); ϵ_{Si-C}=0.008909 eV, σ_{Si-C}=3.326 Å(Ong and Pop, 2010); ϵ_{O-C}=0.003442 eV, σ_{O-C}=3.001 Å(Ong and Pop, 2010). The Ar-Si and Ar-O interaction parameters were obtained using the standard Lorentz-Berthelot mixing rule.

The system was first relaxed at room temperature (300K) with a pressure of 0.03 MPa, at which point the gas density and pressure was slowly increased by reducing the volume of gas. When the desired deflection of graphene was reached, the gas

density was then kept fixed, and the system was allowed to relax at that pressure for 10 ps. The final equilibrium configuration of graphene was computed by averaging over all of the atomic positions of graphene during the relaxation period with constant gas density. The substrate was assumed to be rigid and fixed during the simulation. As a boundary condition on the graphene, the atoms in the outer 1 nm annulus of the supported graphene were fixed during the simulation matching the experimental observation that the supported graphene only slides in a local region around the hole, remaining fixed at large radii. A canonical ensemble (NVT) at room temperature (300K) was used for the entire simulation and reflection boundary conditions were used to ensure that gas atoms remained inside the simulation box.

To calculate the strain in the deformed graphene sheet, the atomistic displacement field was first found (Zimmerman et al., 2009) by calculating the difference between the reference (initial) configuration and the final, deformed configuration. The strain tensor from continuum mechanics was then calculated as

$$\epsilon_{ij} = \frac{1}{2} \left(\frac{\partial u_i}{\partial X_j} + \frac{\partial u_j}{\partial X_i} + \frac{\partial u_k \partial u_k}{\partial X_i \partial X_j} \right), \tag{4.20}$$

where ϵ_{ij} are the components of the strain, u is the displacement, and X denotes the position of a point in the reference configuration.

The displacement field $\mathbf{U}$ for each atom was computed by linearly interpolating, using standard finite element method shape functions for triangular elements (Hughes, 1987). The displacements of its three nearest neighbors is calculated as $\mathbf{U} = \mathbf{N} \bullet \mathbf{u_N}$, where $\mathbf{N}$ are the finite element shape functions and $\mathbf{u}_N$ are the displacements for each atom. From the displacement field $\mathbf{U}$, the strain was calculated by taking derivative of $\mathbf{U}$ as $\epsilon = \mathbf{B} \bullet \mathbf{u_N}$, where $\mathbf{B} = \frac{\partial \mathbf{N}}{\partial \mathbf{X}}$. The atomistic data plotted in the paper was obtained from the MD simulation results by the method above, and was expressed in

polar coordinates.

4.5 Fitting Raman spectra to the continuum model

In conjunction with the measured Raman spectra, the extended continuum model can be used to determine the sliding friction, the Grüneisen parameter, and the shear deformation potential. A simple comparison of the strains predicted by the extended Hencky model to strains found by directly inverting the positions of the G^+ and G^- peaks is not possible because of the finite size of the focused laser beam. Instead, model spectra are predicted by integrating against the system point spread function. A set of model spectra created for each point in the line scan can then be compared to the measured line scan spectra. The best fit is found by creating model spectra for a series of different fitting parameters and choosing the one that best matches the measured spectra. This is done quantitatively by choosing the modeled spectra with the smallest χ^2. A detailed description of the fitting algorithm used as well as the determination of fitting error is presented in Appendix C.

Unlike the sliding friction, the Grüneisen parameter and shear deformation potential should be the same for every line scan. As such, they were included as fitting parameters in only the two lines scans which best defined β based on the splitting of the supported graphene's G band just outside the edge of the microchamber: the $\sim 5\mu m$ radius monolayer and the $\sim 5\mu m$ radius trilayer at 0.80 MPa of applied pressure. Figure 4.14 shows reduced dimensionality plots of the χ^2 per degree of freedom space. As described in Appendix C, each data point in this type of plot represents the best case for the given value of the plotted fitting parameters. The other, not plotted, fitting parameters (β and F for the γ plot, and γ and F for the β plot) are chosen to minimize χ^2 at each data point. The sharp minimum and the agreement between
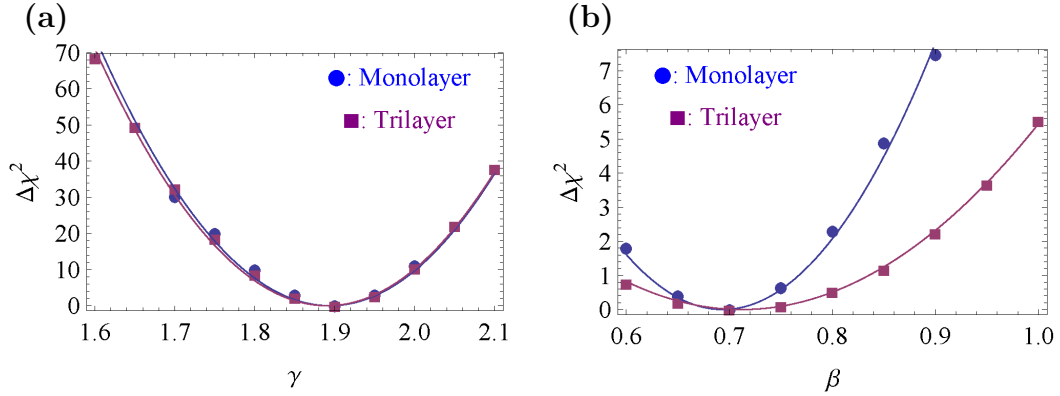
Figure 4.14: Determination of the Grüneisen parameter and shear deformation potential based on global fits to a monolayer covered (blue, circles) and a trilayer covered (purple, squares) $\sim 5\ \mu m$ radius sealed microchamber at 0.80 MPa of applied absolute pressure. All three fitting parameters (F, γ, and β) were included in the fits. In (a) and (b) the reduced dimensionality plots of the deviation of χ^2 per degree of freedom from the minimum are plotted for the Grüneisen parameter and shear deformation potential respectively. The parabolic fits show sharp minimum indicating strongly determined parameters.

monolayer and trilayer indicates a good determination of γ and β. Using an increase in χ^2 per degree of freedom of 0.25 to define uncertainties gives $\gamma_{mono} = 1.89 \pm 0.02$, $\gamma_{tri} = 1.89 \pm 0.02$, $\beta_{mono} = 0.69 \pm 0.04$, and $\beta_{tri} = 0.71 \pm 0.06$. The averages of the monolayer and the trilayer, $\gamma = 1.89 \pm 0.01$ and $\beta = 0.70 \pm 0.04$, were treated as known material parameters when fitting the remaining twenty Raman line scans.

Table 4.1 compares the measurements of the Grüneisen parameter and shear deformation potentials to previous measurements. The substrate on which the parameters were measured is also included. Our measured γ is commensurate with most of the other measured values and agrees particularly well with the *ab initio* calculations of

	γ	β
This work	1.89	0.70
SiO$_2$ depression (Metzger et al., 2010)	2.4	
On PDMS (Huang et al., 2009)	0.69	0.38
On SU8 (Mohiuddin et al., 2009)	1.99	0.99
Embedded (Frank et al., 2010)	2.01	1.01
On Acrylic (Yoon et al., 2011)	2.2	0.93
Bubble (Zabel et al., 2012)	1.8	
Ab initio (Thomsen et al., 2002)	2.0	0.66
Ab initio (Cheng et al., 2011)	1.86	0.96

Table 4.1: Summary of the Grüneisen parameter, γ, and shear deformation potential, β, as measured on different substrates.

Cheng *et al.* (Cheng et al., 2011). On the other hand, the measured shear deformation potential is lower than most other measurements. These other measurements may have been influenced by unaccounted for transverse-sliding of the FLG over the substrate. Out-of-plane buckling in our measurements would cause inaccurate shear deformation potential, but this explanation is inconsistent with our measurements. Monolayer and trilayer graphene would buckle differently for a microchamber with the same pressure and radius yielding different measured shear deformation potentials. As shown in Figure 4.14(b), this difference is not observed. Thus, we believe our measurements of the Grüneisen parameter and shear deformation potentials to be the most accurate yet.

The extended Hencky model agrees extremely well with the measured spectra. Figure 4.15 shows a global data fit for a $\sim 5~\mu m$ radius monolayer covered graphene sealed microchamber at 0.80 MPa of applied pressure. The spectra and fits from each position along the line scan are stacked vertically in the direction of the line scan. The extended continuum model successfully fits the softening and splitting of the G band of the supported graphene and successfully predicts the downshift and

sharpening of the G band of the suspended graphene as the center of the microchaber is approached. In comparison, without the theoretical extension the standard Hencky model would fail to reproduce the supported graphene spectra.

4.6   Measured frictional dependencies

The sliding friction extracted for eight microchambers with radii between 1.2 and 5 μm and with applied absolute pressures from 0.10 to 0.80 MPa exhibits fundamentally different behavior for trilayer graphene than for monolayer and bilayer. In Figure 4.16a (left) the friction is plotted as a function of absolute applied pressure. The data for trilayer graphene (black dots) shows a linearly dependent sliding friction in accordance with Amontons' law with a coefficient of friction of 0.11 ± 0.01. For reference, Teflon on Teflon has $\mu = 0.04$ while clean steel on clean steel has $\mu = 0.6$ (Resnick et al., 2002). A zoom in of the trilayer data is shown in Figure 4.17. The sliding friction for monolayer and bilayer graphene behave much differently. They decrease generally with applied pressure and the wide scatter of the points for different radii and layer number suggesting that the sliding friction is dependent on the geometry of the microchamber and, therefore, does not depend on pressure like a material property should. However, as shown in Figure 4.16b (right) when the sliding friction is replotted as a function of the radial strain at the edge of the microchamber, the monolayer and bilayer data for all different radii microchambers *collapse* to a single curve versus radial strain, well described by $1/\epsilon_{r,edge}$ behavior (dashed line). In effect, the data in Figure 4.16a (right) is scattered because the dependence of friction is not properly isolated. When the correct dependent variable is chosen, the geometric dependencies are eliminated revealing the underlying material property. The best fit to the strain dependence is $0.002 MPa/\epsilon_{r,edge}$.
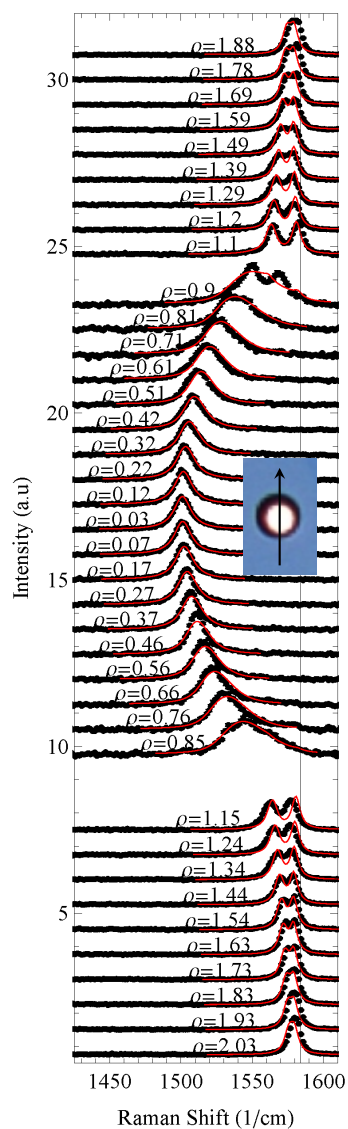
Figure 4.15: Raman spectra from a line scan over a $\sim 5 \ \mu m$ radius monolayer graphene sealed microchamber with 0.80 MPa of applied pressure fit successfully using the extended Hencky model (red lines). The spectra taken along the path shown in the inset are arrayed vertically with spectra taken too close to the edge of the microchamber omitted (see text). The black vertical line is positioned at the supported graphene's unstrained G band energy.
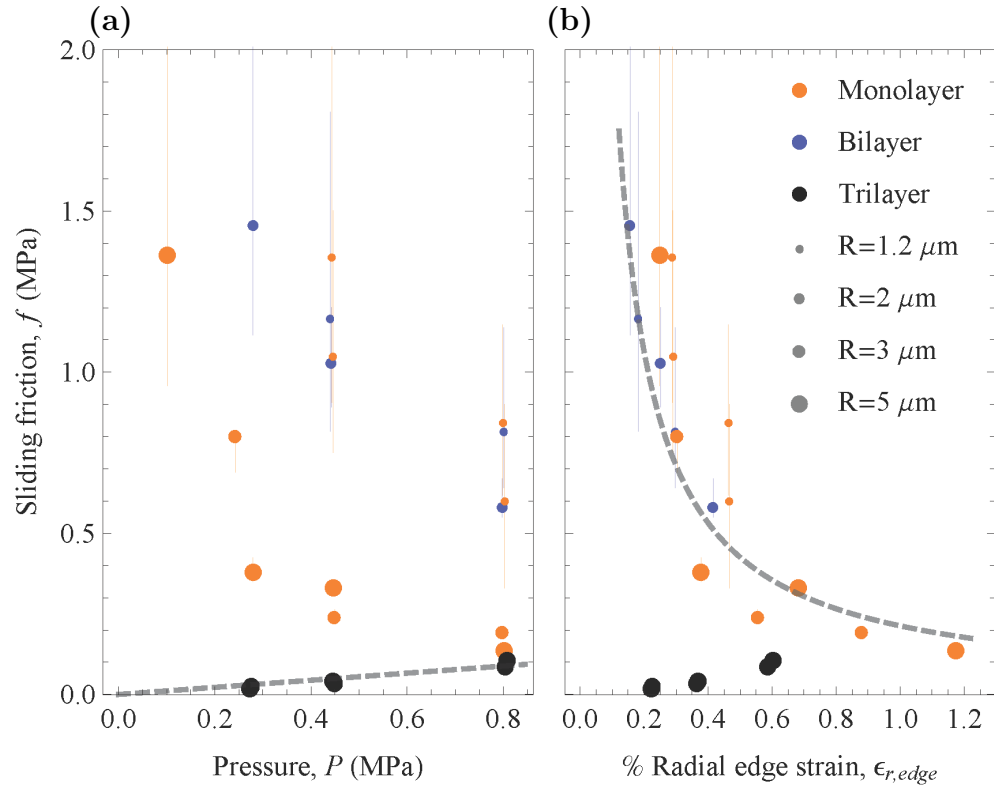
Figure 4.16: The dependencies of sliding friction for FLG extracted by analyzing Raman line scans with the extended Hencky model. In panel (a) (left) friction is plotted as a function of absolute applied pressure where in panel (b) (left) it is plotted as a function of the radial strain at the edge of the microchamber. The size of each data point represents the radius of the FLG-sealed microchamber corresponding to that point. The error bars are given by an increase in global fit χ^2 per degree of freedom of 0.25. The sliding friction of trilayer graphene depends linearly on the absolute applied pressure in agreement with Amontons' law. The sliding friction of monolayer and bilayer graphene, however, go as the inverse of the radial strain at the edge of the microchamber. Gray dashed lines are the best fits to these trends.
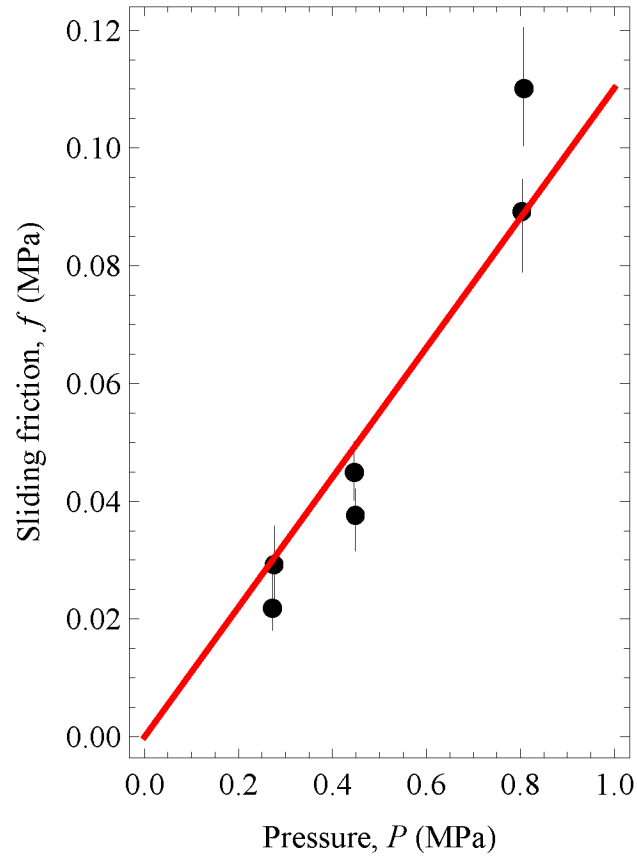
Figure 4.17: The sliding friction for trilayer graphene as a function of the absolute applied pressure extracted from Raman lines scans over two 5 μm radii trilayer sealed microchambers. The datat is fit with Amonton's law, $f = \mu P_{abs}$, giving a coefficient of friction between trilayer graphene and SiO$_2$ of $\mu = 0.11 \pm 0.01$.

The gross difference in behavior between trilayer on one hand, and mono-and bilayer on the other, illustrates the two roles of the applied pressure. The pressure load pushes the graphene more firmly onto the substrate so that sliding friction should increase (Amontons' law), yielding a positive coefficient of friction. This is the case for the trilayer graphene. On the other hand, as the pressure pushes the graphene into the microchamber, it creates a radial tension in the supported graphene outside the microchamber. The data collapse to a single $1/\epsilon_{r,edge}$ dependence in Figure 4.16b for monolayer and bilayer graphene demonstrate that the pressure dependence of the sliding friction is not due to loading the supported graphene but is instead dominated by the graphene being pulled and stretched by the applied pressure. This is the only mechanism that would depend on the geometric parameters of the microchamber while also being consistent with the data. It is not surprising that the sliding friction for mono- and bilayer graphene is dependent on the strain and not the load because thin graphene conforms nearly perfectly to a SiO_2 substrate (Stolyarova et al., 2007; Lui et al., 2009; Cullen et al., 2010). Increasing the load cannot further increase the contact area, but increasing the radial strain beyond the edge of the microchamber may act to smooth out the graphene sheet, decreasing the contact between the graphene and the substrate, and thus decreasing the sliding friction. The bending rigidity, which goes as thickness cubed, of trilayer graphene must be high enough to counteract the adhesion energy, causing lower conformation and allowing for a traditional pressure and load response. The existence of a bilayer to trilayer crossover in FLG-substrate interactions is also observed in GPa range pressure measurements of silicon dioxide supported graphene (Proctor et al., 2009; Nicolle et al., 2011). Nicolle *et al.* observed a decrease in the pressure response of the G band between bilayer and trilayer graphene which was attributed to the transition from biaxial compression mediated by the substrate to hydrostatic compression mediated by the pressure

transmitting medium (Nicolle et al., 2011).

4.7 Summary

In summary, it has been demonstrated that few layer graphene slides along the substrate when pulled. Furthermore, using a newly developed extension of the continuum Hencky model, the sliding friction as a function of the number of atomic layers and the load was extracted. Trilayer graphene shows a typical load response whereas the sliding friction for monolayer and bilayer graphene goes as the inverse of strain. The data collapse of the friction for mono- and bilayer graphene when plotted versus strain is strong experimental evidence for a reduction in surface conformation when graphene is pulled as the fundamental origin of the negative coefficient of friction. These results will be important for the design of strain engineered devices (Pereira and Castro Neto, 2009), while the sliding of a flexible surface along a bulk object should be of fundamental, tribological interest. Finally, the method used in generalizing Hencky's solution should be useful for including distributed strains in other continuum models for use in designing strain-engineered graphene devices and in understanding other, few-layer material systems.

Chapter 5

The thermal conductivity of strained graphene

The atypical thermal conductivity of graphene has been attributed to the out of plane acoustic (ZA) phonons. These phonons are believed to contribute in two ways that conflict so much that if the ZA phonons were a person, they might be characterized as productive egomaniacs. On one hand, they are believed to productively enable graphene's very high thermal conductivity by contributing more than 70% of the thermal conductivity of suspended graphene (Lindsay et al., 2010). On the other hand, they are thought to suppress the potentially divergent thermal conductivity contributions from the in-plane acoustic phonons (Pereira and Donadio, 2013; Bonini et al., 2012). Both of these opposing contributions are linked to the abnormal quadratic dispersion of the ZA phonons. Currently, the theoretical understanding of this interesting and unique system is based solely on the observation that the thermal conductivity of supported graphene is smaller than suspended graphene (Lindsay et al., 2010). Here we further test the theoretical understanding by measuring how the thermal conductivity is altered when strain and pressure modify the ZA phonons. We observe no absolute indications that either strain or pressure affect the thermal transport in the atypical ways which might be expected for ZA phonon dominated transport. This information should help us understand the importance of the ZA phonons and further test our understanding of graphene's high thermal conductivity.

We begin be describing past experimental measurements of graphene's thermal conducting with emphasis on the diminished thermal conductivity of supported graphene. Next, we review the theoretical explanation of this observation and summarize the predicted effect of strain. Finally, we discuss our experimental measurements starting with a description of the measurement, followed by an explanation of the data analysis, and finishing with a discussion of our results.

5.1   Experimental background

In the first measurements of graphene's thermal conductivity, Balandin and coworkers reported a record high thermal conductivity of roughly 5000 W/m-K (Balandin et al., 2008) in suspended graphene. Shortly thereafter measurements of supported graphene showed a more modest thermal conductivity of roughly one sixth of the original value (Seol et al., 2010). This discrepancy has been the source of several studies in the years since.

The original measurements were performed on suspended graphene samples using an optical technique. This creative technique uses a laser excitation to heat the sample and the temperature induced energy shift of the Raman scattered light to measure temperature. The laser excitation provides both a heat source and a thermometer. When used in conjunction with a heat transfer model, this is enough to determine the thermal conductivity. This technique has advantages and disadvantages. The required samples are very simple to fabricate and the measurement is fairly standard. However, the measured thermal conductivity depends on a variety of hard to measure parameters including the optical absorption of the graphene, the laser spot size, and the temperature dependence of the phonon modes. What's more, the results depend on the accuracy of diffusive thermal transport models which cannot account

for ballistic transport phenomena.

The simplicity of the optical technique has spurred its use in studying aspects of thermal transport in suspended FLG and the Raman measurement technique has since been advanced in a series of publications (Balandin et al., 2008; Faugeras et al., 2010; Cai et al., 2010; Ghosh et al., 2010; Lee et al., 2011; Chen et al., 2011; Chen et al., 2012). Faugeras *et al.* showed that the symmetry of graphene over a circular microchamber simplifies the heat transfer model. Additionally, they validated the use of phonon energy shifts as a temperature measurement by using the Raman Stokes to anti-Stokes ratio as an independent measurement (Faugeras et al., 2010). Cai *et al.* advanced the thermal transport model by including the heat transfer to the substrate instead of treating the edge of the microchamber as a heat sync. Chen *et al.* included thermal conductivity to the surrounding gas but not the substrate (Chen et al., 2011). As described in Appendix D, the thermal model used to interpret our results combines the models in these works.

The more modest value for the thermal conductivity of supported graphene was measured with a different technique (Seol et al., 2010). The measurement was direct; it used resistive heaters to create temperature gradients and solid state thermometers to measure the temperature. The thermal conductivity was then determined directly from the thermal resistance of the graphene. Although this technique has less error sources, the measurements and sample fabrication are much more difficult. As a result, there has been only one other measurement of the thermal conductivity of graphene using this technique (Jang et al., 2010).

Figure 5.1 summarizes all of the reported room temperature thermal conductivity measurements of single layer graphene. It is clear that graphene's thermal conductivity is negatively effected by the presence of a supporting or encasing bulk material. The thermal conductivity decrease from a value of roughly 2000 W/m-K for suspended

graphene, to a value close to 500 W/m-K for graphene supported on one side, to a value of less than 160 W/m-K for graphene encased in SiO_2 (Jang et al., 2010). The different thermal conductivities cannot be attributed to the different measurement techniques. A nanoscale thermal conductivity measurement also observed suppressed thermal conductivity in supported FLG (Pumarol et al., 2012). The observation of suppressed conductivity has driven the theoretical work described in the next section.

5.2 Theoretical background

Lindsay and coworkers argue that ZA phonon dominated thermal conductivity in suspended graphene explains the observed environmental dependence of the thermal conductivity. They argue that the large, 70 %, contribution of the ZA phonons comes about for two reasons. First, the quadratic dispersion of the ZA phonons gives them a higher density of states throughout the BZ than linearly dispered in-plane phonons. Second, the in-plane reflection symmetry provides a selection rule that limits the scattering phase space (Lindsay et al., 2010). ZA phonon dominated thermal transport is consistent with the observed suppression of the thermal conductivity in supported graphene. When the graphene is in contact with bulk materials the ZA phonons either leak into the surrounding media, are scattered by it, or are dampened by it thereby lowering the thermal conductivity. The quadratic nature of the ZA phonons should not only be a feature of monolayer graphene, but should persist for FLG as well (Lindsay et al., 2011).

The ZA phonons are also believed to limit the potentially divergent thermal conductivity contribution of the in-plane phonons. Klemens showed that the linear in-plane acoustic phonons should contribute a logarithmically divergent thermal conductivity in graphene (Klemens, 2001). This divergence follows from the frequency depen-
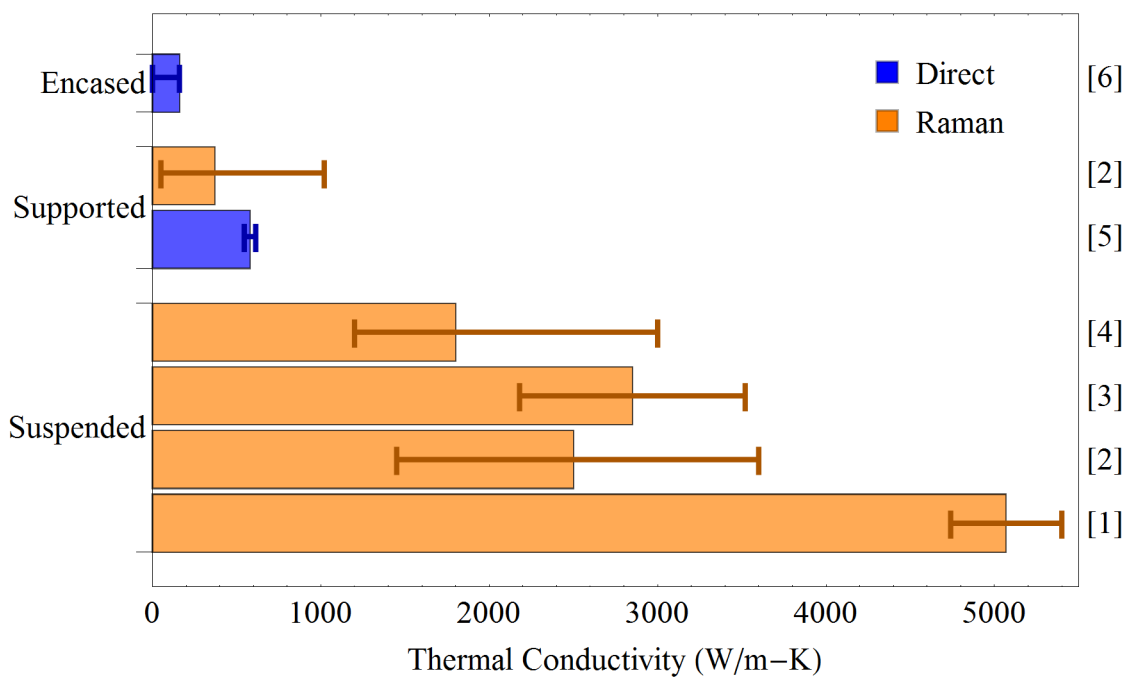
Figure 5.1: Summary of the reported values of the room temperature thermal conductivity of monolayer graphene grouped by the environment of the graphene: Suspended, supported on a bulk substrate, and encased in amorphous SiO_2. The color code indicates whether the measurements were performed using the Raman technique or a direct technique. The numbers on the right indicate the source: [1] is (Balandin et al., 2008), [2] is (Cai et al., 2010), [3] is (Chen et al., 2011), [4] is (Lee et al., 2011), [5] is (Seol et al., 2010), [6] is (Jang et al., 2010). Error bars are taken from the literature.

dence of the terms which make up the thermal conductivity, $\kappa = \frac{1}{3} \int C v_G l(\omega) \rho(\omega) \, d\omega$, where κ is the thermal conductivity, C is the specific heat, v_G is the group velocity of the acoustic phonons, $l(\omega)$ is the scattering length, and $\rho(\omega)$ is the density of states. For a two dimensional phonon gas with linear dispersion, $\rho(\omega) \propto \omega$; while for anharmonic scattering between linear acoustic phonons, $l(\omega) \propto 1/\omega^2$. Hence, in the absence of extrinsic scatterers the integrand scales as $1/\omega$ and κ diverges logarithmically. The logarithmic divergence in ω should translate to a logarithmic divergence in device size (Klemens, 2001). Larger devices should exhibit larger thermal conductivities because they support more of the long wavelength phonons that contribute strongly to the thermal conductivity. To date this logarithmic divergence has not been observed (Chen et al., 2011).

Pereira and coworkers believe that the ZA phonons suppress this divergence. When these ZA phonons are neglected in equilibrium molecular dynamics simulations, the thermal conductivity diverges in agreement with Klemens; when they are included, the thermal conductivity converges to a large, but finite value (Pereira and Donadio, 2013). It is believed that this is due to the ZA phonons near the center of the BZ. With near zero group velocity these phonons cannot enhance thermal conductivity, but, with a large population they can effectively scatter the in-plane phonons and eliminate the divergence. Thus, the ZA phonons are the main contributor to graphene's thermal conductivity only because the low energy ZA phonons suppress the divergent thermal conductivity of the in-plane phonons.

Simulations by both Pereira (Pereira and Donadio, 2013) and coworkers and Bonini and coworkers (Bonini et al., 2012) show that strain could act to liberate the divergent thermal conductivity contribution of the in-plane phonons. By linearizing the ZA phonon modes near the Γ point, strain decreases the density of states of the zero group velocity ZA phonons and limits the scattering of the in-plane phonons.

Uniaxial strain of 2 % should reduce this scattering enough to realize the divergent thermal conductivity of the in-plane phonons (Pereira and Donadio, 2013) while for biaxial strain any amount of strain should be enough (Bonini et al., 2012).

5.3 Tuning the ZA phonon

Although the theory discussed to this point is convincing, it deserves further testing. It was built around only two data points: The high thermal conductivity of suspended graphene and the lower thermal conductivity of supported graphene. Further, the resulting theory relies on the exotic, quadratically dispersed, ZA phonons which have only been measured directly in graphene mechanical resonators. Here we take advantage of the two dimensional nature of graphene which enables additional ways to study the thermal transport.

The ZA phonons can be continuously tuned while the thermal conductivity is measured *in situ* using the device geometry from Chapter 4. The phonons are altered in two ways. First, the strain induced in pressurized graphene sealed microchambers linearizes the ZA phonon dispersion. As discussed in the previous section, this might increase the thermal conductivity by liberating the divergent thermal conductivity of the in-plane phonons (Pereira and Donadio, 2013; Bonini et al., 2012). Second, the gas surrounding the suspended graphene should lower the lifetime of the ZA phonons. This has been observed in graphene mechanical resonators which exhibit decreased quality factors in ambient pressure compared to vacuum (Bunch et al., 2007). Lowering the phonon lifetime should lower their contribution to the thermal conductivity. In this section we describe our efforts to provide deeper insight into the mechanism behind the high thermal conductivity of suspended graphene by measuring the effect of strain and pressure on thermal conductivity.

5.3.1 Thermal measurements

The experimental geometry described in Section 4.2 not only enables the ZA phonons to be tuned, it allows allows the effects of strain and pressure to be decoupled. The phonons are tuned by setting the external pressure, P, to gauge pressures which range from -0.1 MPa of vacuum to 0.69 MPa of overpressure using argon as a pressure transfer medium. Measuring with the external pressure both greater than and less than the pressure inside the microchamber, P_0, isolates strain and pressure effects. Pressure effects should increase monotonically with pressure while strain effects should come to a minimum when $P = P_0$ and the graphene is flattened out. Thus, the symmetry of the observed trends about P_0 allows pressure and strain effects to be decoupled.

The Raman technique described in Section 5.1 is used to measure the thermal conductivity. Linearly polarized, 514.5 nm laser light from an argon ion laser is focused on the center of the microchamber. The focused beam waist, measured the same way as was done in Section 4.1, is 0.66 ± 0.04 nm. The power which reaches the sample is tuned by changing the laser power, not by changing ND filters. This ensures that the centering of the beam is not power dependent. The power which reaches the sample is calculated from the power measured at the exit port of the Renishaw by using the system throughput of 0.67 ± 0.01. The laser stability over the measurement period is 2 %. Raman spectra measured at several incident powers can be used to measure the temperature by monitoring the energy of the measured phonon modes.

The temperature is measured using the heating induced shifts of the G and 2D energies: $\Delta\omega = \chi\Delta T$, where ΔT is the change in temperature and χ represents the temperature dependence arising due to anharmonicities (Bonini et al., 2007). As starting points we use the values measured by Chen *et al.* on suspended CVD

graphene: $\chi_G = -(4.4 \pm 0.3) \times 10^{-2}\ cm^{-1}/K$, $\chi_{2D} = -(7.2 \pm 0.2) \times 10^{-2}\ cm^{-1}/K$ (Chen et al., 2011). Other measurements report lower values of χ_G and χ_{2D} (Calizo et al., 2007), and hence, higher thermal conductivities (Balandin et al., 2008). These values were not used because they were measured on supported graphene where the different thermal expansion coefficients of graphene and its supporting substrate could be more of an issue. In addition to the temperature induced energy shifts, the phonon modes are also influenced by strain, which can cause order of magnitude larger shifts. To isolate the temperature induced energy shift, at each applied pressure two spectra are measured: One at a lower power, P_{lo}, and one at a higher power, P_{hi}. Both measurements have a common strain-induced energy shift which does not influence the energy difference measured between the two powers. The measure temperature, T_M, is related to the energy shift, $\Delta\omega$, by assuming a constant thermal resistance, $R = \frac{\Delta T}{P}$ where P is the absorbed power. The measured temperature is

$$T_M = T_{hi} - T_0 = \frac{\Delta\omega}{\chi}\frac{P_{hi}}{P_{hi} - P_{lo}}\ , \tag{5.1}$$

where T_0 is ambient temperature. The corresponding measured thermal resistance is $R_M = T_M/P_{hi}$. The measured values do not represent the temperature at the center of the microchamber. They are weighted averages over the finite spot of the laser beam.

It should be noted that these temperature dependent phonon energy shifts are due to phonon anharmonicities and, as such, they may have some strain dependence. We are ignoring this possibility here. The Anti-Stokes to Stokes ratio could be used as an alternative, anharmonicicty independent temperature measurement. However, we found that these measurements were not useful as they took too long and were too hard to interpret.

The heat transfer model described in Appendix D is used to extract the thermal parameters from the measured temperatures. The model depends on the thermal conductivities of the suspended graphene, κ_{SS}, and the supported graphene, $\kappa_{SP} = (579 \pm 34)$ W/m-K (Seol et al., 2010), as well as the interface thermal conductivities to the gas, g_G, and to the substrate $g_S = (50 \pm 13)$ MW/m^2-K (Mak et al., 2010). An example temperature distribution predicted by this model is shown in Figure 5.2. As one might expect, the temperature rise is the greatest in the center of the microchamber where the laser is positioned. At the edge of the microchamber the slope is discontinuous due to the change in thermal conductivity. Where the thermal conductivity is lower it takes a larger temperature gradient to conduct the same heat energy. The green shaded region represents the radial envelope of the excitation profile. It illustrates that T_M is not the temperature rise at the center of the hole but is rather an average over a radial window. Appendix D describes how T_M can be used to find the thermal parameters.

The samples described in Table 5.1 were measured by taking Raman spectra with multiple excitation powers across a range of pressures. The number of layers was found using Raman spectroscopy and optical interference, the radius and hole depths were measured using low force contact mode AFM, and the maximum strain was calculated using Hencky's model (Hencky, 1915). Device fabrication was either done using the standard mechanical exfoliation technique or by using a polymer based aligned transfer technique (Goossens, 2013). Pressures were decreased in increments from 0.69 MPa to -0.1 MPa and then increased back to 0.69 in inter-spaced increments to monitor for any hysteretic response. These measurements allowed for the extraction of the pressure dependent measured thermal resistance.
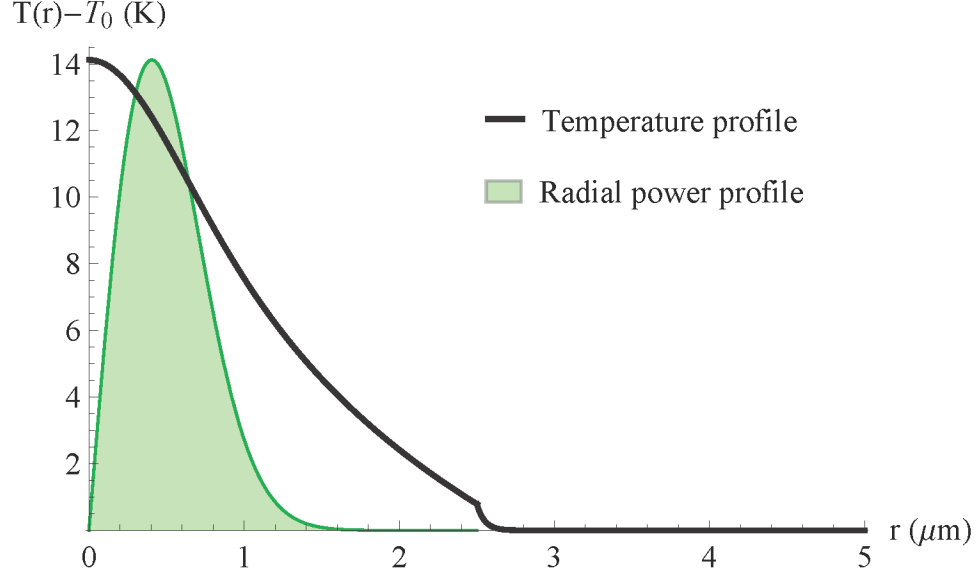
Figure 5.2: Theoretical temperature distribution in a graphene sealed microchamber heated by a centered laser. The black curve shows the temperature increase for a 5 μm diameter microchamber assuming that $\kappa_{SS} = 2000$ W/m-K and $g_G = 0.03$ MW/m^2-K (Chen et al., 2011). The radial profile of the 1.5 mW laser heat source with a 0.66 μm waist is overlaid in green.

Samples	NL	Radius	Depth	ϵ_{max}	Fabrication	Sealed?
FFF	1	(3.09 ± 0.04) μm	> 5 μm	N/A	Transferred	no
SB07-1	1	(2.74 ± 0.08) μm	$\simeq 230$ nm	1.1 %	Exfoliated	yes
SB08-2	2	(1.52 ± 0.07) μm	> 3 μm	0.46 %	Exfoliated	yes
SB03-2	3	(4.99 ± 0.01) μm	> 5 μm	0.77 %	Exfoliated	yes

Table 5.1: Details of the samples used in thermal conductivity measurements. NL refers to the number of layers and ϵ_{max} is the maximum strain.

5.3.2 Data analysis

This section details the analysis done to determine the measured thermal resistances from the Raman spectra.

Peak positions were found by fitting the measured spectra to representative spectral shapes. The G peak was fit to a single Lorentzian for all four samples. Fitting the 2D peak was more complicated because the peak shape depends on the number of layers. For suspended monolayer graphene the 2D peak is best fit by two Lorentzians with equal widths separated by 14 wavenumbers (Berciaud et al., 2013). To limit the number of fitting parameters, the ratio of the peak amplitudes was taken as 3.44, the average of less restricted best fits. For bilayer graphene the 2D peak is best fit by 4 Lorentzians with equal widths (Ferrari et al., 2006; Malard et al., 2007). The fitting parameters were restricted to an amplitude, a width, and a position by setting the separation between peaks and the relative amplitudes between peaks based on the average of less restricted best fits. An example of the best fit to a bilayer spectra is shown in Figure 5.3 showing good agreement between the spectra measured at 0.69 MPa and the fitting function. Since there is no well-excepted form for the trilayer 2D band, the temperatures were only determined from the G band data for sample SB03-2. The extracted peak positions were used to analyze the response of the system to pressure and heating.

Figure 5.4(a) shows the best fit positions of the G and 2D bands as a function of pressure for bilayer sample SB08-2. As described in detail in Chapter 4, the overarching response is governed by the linear dependence of the Raman bands on strain. The strain, in turn, scales roughly as $(P-P_0)^{2/3}$ where P_0 is the pressure inside the microchamber. The data in the Figure is fit by the expected pressure dependence and the extracted value of P_0 is indicated by the black vertical line. Samples SB07-1,
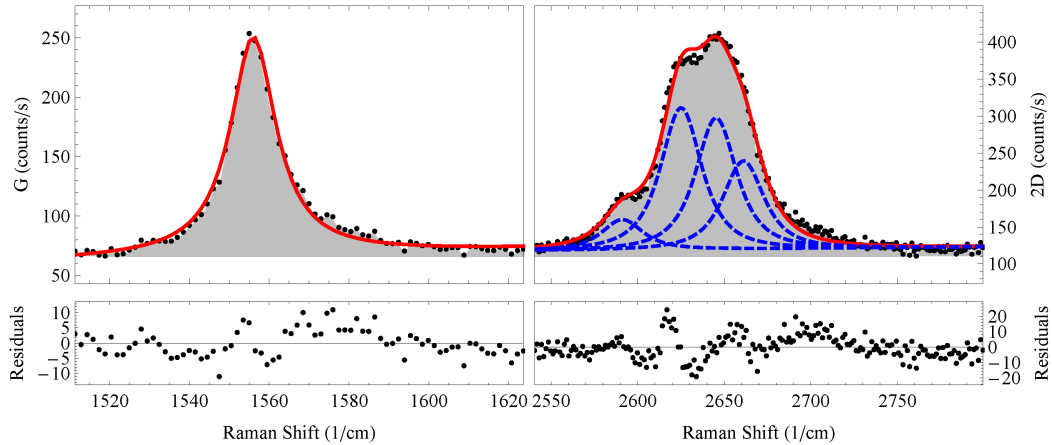
Figure 5.3: A representative fit to the Raman spectra taken at the center of bilayer sample SB08-2 using 2 mW of incident power at 0.69 MPa of gauge pressure. The restricted four Lorentzian fit to the 2D spectra matches the data well.

SB08-2, and SB03-2 all exhibit this type of pressure dependent response. For sample FFF, on the other hand, the Raman peak energies exhibit no measurable pressure dependence indicating that the membrane is leaky as shown in Figure 5.4(b). Thus, this sample is insensitive to strain effects. The effects of laser heating in Figure 5.4 are hidden in the fine structure. Spectra taken at higher laser powers exhibit systematically lower peak positions due to heating.

The use of Equation 5.1 to calculate the temperatures from the peak shifts is complicated by optical interference. As shown in Figure 5.5, the measured temperatures for sample SB07-1 exhibit an oscillatory behavior in pressure that is correlated with similar oscillations in the measured G and 2D integrated areas. This suggests that the observed behavior is driven by optical interference in the excitation beam. As overpressure is applied to the graphene, it is pushed into the microchamber, moving it from a point where the excitation undergoes destructive interference, to a point of constructive interference, and then back to a point of destructive interference. As the
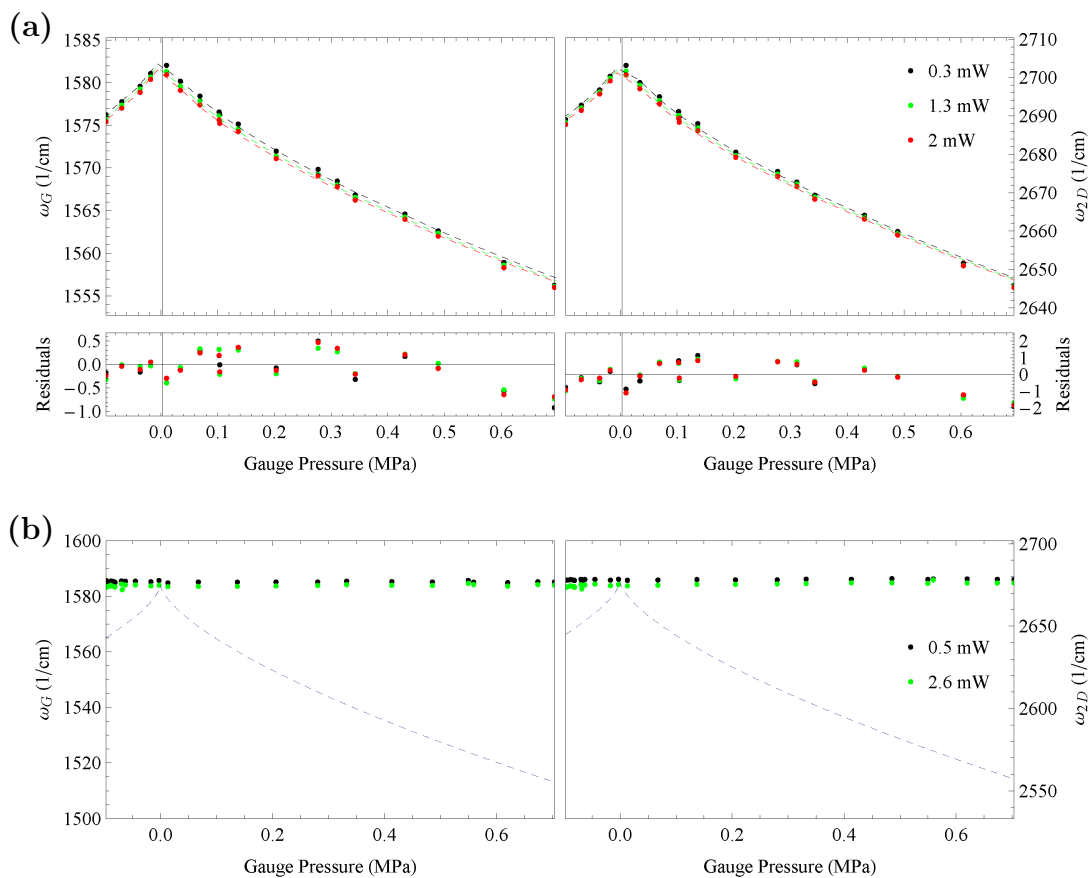
Figure 5.4: The peak positions measured as a function of applied pressure with three different laser excitation powers for (a) the sealed bilayer sample SB08-2 and (b) the leaky monolayer sample FFF. In (a) the peak positions are fit to the expected $(P - P_0)^{2/3}$ behavior and the best fit value for P_0 is indicated by the black vertical line. In (b) the pressure response that a sealed microchamber would have undergone is indicated by the blue dashed line. In both cases increasing laser excitation power systematically red shifts the peak positions.

interference changes, the amount of power heating the graphene changes, and thus, so does the temperature. The integrated areas of the G and 2D peaks also depend on the incident laser power and, thus, the correlation between the oscillations in integrated areas and the oscillations in the measured temperature is a strong indicator of optical interference effects. The interference interpretation is further supported by the agreement between the number of interference minimum and the expected displacement at the center of the graphene. Minimum are expected every half wavelength and from -0.1 MPa to 0.69 MPa, the graphene displaces by 508 nm or roughly one wavelength consistent with the two minimum in Figure 5.5. The interference in SB07-1 is the strongest, but all of the other devices exhibit similar interference phenomena. The Rayleigh range of the focused beam is ~ 2.7 μm indicating that even microchambers with depths of 8 μm might be expected to exhibit weak interference effects. Interestingly, even leaky sample FFF shows very slight signs of interference probably due to the nonlinearity of the pressure deflection curve. In the low pressure regime small pressure changes cause relatively large deflections which could cause interference effects; for FFF, a differential pressure of only 0.001 MPa would cause a deflection of 40 nm. This small deflection generate a small, 0.015 %, strain which would be challenging to detect with Raman peak shifts. To correctly interpret the thermal response of the system, this interference must be accounted for.

The optical interference of the excitation beam can be estimated from the oscillatory behavior of the Raman signal. Raman interference is driven by the product of the optical interference of the incident beam and the outgoing, inelastically scattered light. Approximating the system as a plane wave incident on a perfect mirror, the product of these two terms gives the Raman peak area as $Area = P_i 4 \sin^2(kz) \sin^2(k_R z)$ where z is the distance of the graphene above the mirror, k is the spatial frequency of the laser excitation, k_R is the spatial frequency of the inelastically scattered light, and P_i is the
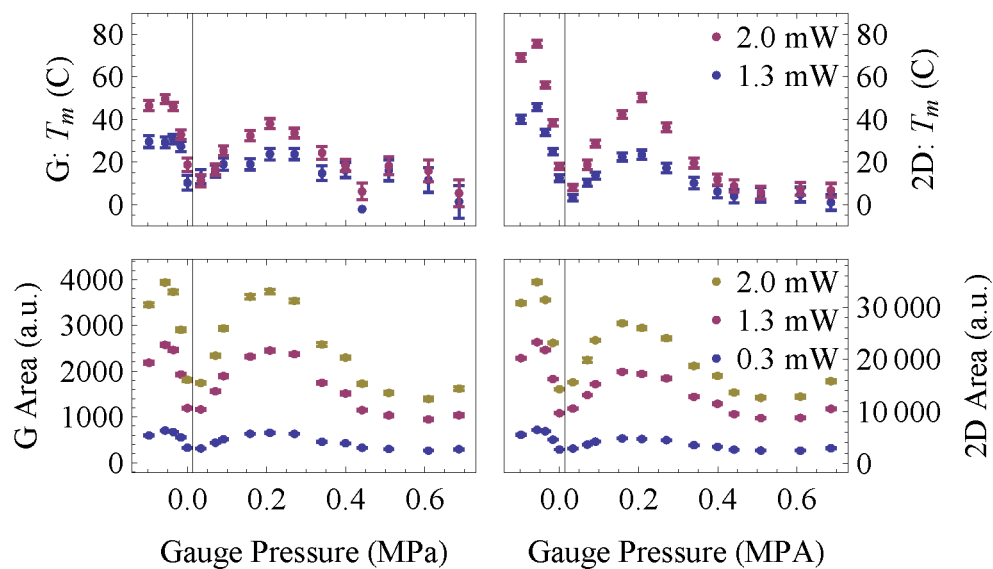
Figure 5.5: A comparison of the temperatures calculated from the shifts of the G peak (top, left) and the shifts of the 2D peak (top, right) with the measured areas of the G peak (bottom, left) and the 2D peak (bottom, right). Measurements were taken on monolayer sealed sample SB07-1. The oscillatory behavior in all four plots suggests that the observed behavior is a result of optical interference.

power of the incident beam. The perfect mirror approximation is reasonable for silicon with light in the visible. Using silicon's optical constants from Palik *et al.* (Palik and Ward, 1991) reproduces the approximate behavior with a negligible 2 % constant offset. The oscillations in the measured temperature, however, is only driven by the interference in the incident beam, $f_{int} = 2\sin^2(kz)$. The fact that the exact depths of the microchambers are not known and that the interference is in a Gaussian beam and not a plane wave makes a direct calculation of the incident power from the oscillations in the Raman areas impractical. Instead, we approximate the interference in the area of the Raman peak as $Area = 4P_i \sin^2(kz)\sin^2(k_R z) \simeq 4P_i \sin^4(kz) = P_i f_{int}^2$ allowing an estimation of the interference in the excitation beam.

In addition to the interference oscillations there is a constant background underlying the G and 2D areas as shown in Figure 5.5. The signal contributing to this offset is believed to be generated by light which is not interfering. This could be a result of a rough silicon back plane or from the divergence of the beam. Thus, the area of the Raman peak can be expressed as the sum of a not-interfering component and an interfering component with relative amplitudes A and $\frac{1}{4}B$

$$Area = P_i\ A + P_i\ \frac{1}{4}B\ f_{int}^2 \rightarrow f_{int} = 2\sqrt{\frac{Area/P_i - A}{B}}\ .$$

$P_i A$ and $P_i(A+B)$ are then the minimum and the maximum measured integrated areas areas, respectively. The factor of $1/4$ is included so that B is the amplitude of the interference oscillation. The intensity of the incident beam is then corrected by dividing by the normalized intensity at the sample: $(A + f_{int}\ B/4)/(A + B/8)$. Using this correction, the thermal resistances can be calculated from the measured temperatures. The resulting R_M should be independent of interference effects up to the approximations used.
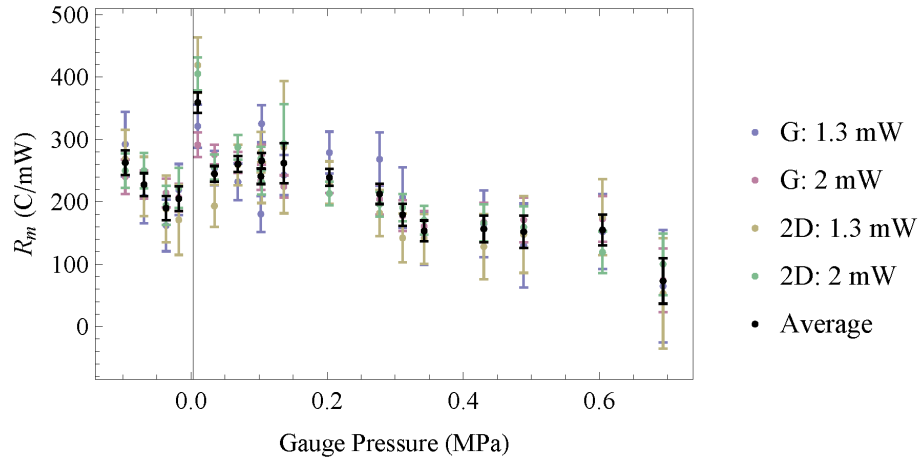
Figure 5.6: The average measured thermal resistance of bilayer sample SB08-2. The four different measurements used to calculate the average are in good agreement. The black vertical line is positioned at P_0.

Accurate determinations of the measured thermal resistances are enabled by redundant measurements. For samples FFF, SB07-1, and SB08-2 both the G and 2D shifts can be used to calculate R_M. The values of χ reported by Chen *et al.* (Chen et al., 2011) provided good agreement between G and 2D data for sample SB08-2. However, for sample FFF, a slight offset in χ_G and χ_{2D} was required to achieve good agreement. The values of χ for the G and 2D peaks needed to be increased and decreased by 0.6×10^{-2} cm^{-1}/K respectively. For sample SB07-1, the G and 2D measurements are presented separately. Samples SB07-1, SB08-2, and SB03-2 were measured at three different powers providing two additional measurements of R_M. Averaging all of the redundant measurements provides higher certainties. Figure 5.6 shows an example of the averaged R_M data. The individual R_M measurements are in good agreement, justifying the averaging.

In summary, the measured thermal resistance is calculated by fitting the measured

spectra, using the heating shifts to determine temperatures, correcting for optical interference, and averaging over redundant measurements. The general trends in the measurements are discussed in the following section.

5.3.3 Discussion

Figure 5.7 shows the thermal resistance measured on the four samples. The thermal resistance of the leaky monolayer (FFF) was roughly a factor of four larger than the sealed bilayer (SB08-2) and the sealed trilayer (SB03-2). This is probably because the holes in the leaky monolayer decrease the thermal conductivity and increase the thermal resistance. However, when its thermal resistance was scaled by a factor of 0.28 the pressure dependent thermal resistance of FFF agreed well with SB08-2 and SB03-2. They all exhibit a decrease in R_M with increased pressure with a dip in thermal resistance near -0.05 MPa. The lack of symmetry about the pressure inside the microchamber ($P_0 \approx 0$) indicates that the trend is unrelated to the strain in the graphene. This is further supported by the agreement between the sealed microchambers which are strained by pressure and the leaky microchambers which are not. The origin of the dip at -0.05 MPa is not understood at this time. The sealed monolayer graphene measurements, on the other hand, do display symmetry about P_0. However, the correlation between these features and the optical interference in Figure 5.5 indicates that these features could be attributed to imperfect interference corrections. In fact, this device should be most sensitive to the approximations made in correcting the optical interference since the sealed monolayer is the most shallow and undergoes the most interference. Thus, for monolayer graphene the observed trend is indecipherable and for bilayer and trilayer graphene in the strain regions measured (see Table 5.1), there is no evidence for strain dependent thermal conductivity. Additionally, no measurements show the significant decrease in R_M at high

pressure which would indicate the predicted strain-induced transition to divergent thermal conductivity (Bonini et al., 2012; Pereira and Donadio, 2013).

The pressure dependent measured thermal resistances seen in the leaky monolayer (FFF), the sealed bilayer (SB08-2), and the sealed trilayer (SB03-2)could originate from thermal conduction to the gas, from viscous damping of the ZA phonons, or from both. To test if the observed behavior can be reasonably attributed only to the thermal conduction the gas, viscous damping was neglected and the interface thermal conductivity to the gas, g_G, was fit to the data following Appendix D. Assuming that $g_G = 0$ W/m^2-K in a vacuum, the in-plane thermal conductivity was extracted from the measurement with the largest R_M measured at vacuum. This gave $\kappa_{SS} = 1070 \pm 120$ W/m-K, $\kappa_{SS} = 1730 \pm 130$ W/m-K, $\kappa_{SS} = 820 \pm 40$ W/m-K for the bilayer, trilayer, and leaky monolayer samples respectively. One sigma confidence intervals were calculated using a Monte-Carlo technique which accounts for all known uncertainties. The results are shown in Figure 5.8

The behavior of the interface thermal conductivity of the leaky monolayer is different than the sealed bilayer and trilayer samples. For pressures greater than ambient pressure, the interface thermal conductivity of the leaky monolayer increases roughly linearly with pressure. This linear trend is expected based on a kinematic model (Chen et al., 2011). At higher pressures there are more atoms in the gas available to conduct heat away from the sample. Additionally, the ambient pressure value of $g_g = 0.06 \pm 0.03$ MW/m^2-K is in fair agreement with the previously measured value for graphene in air of $g_g = 0.029 + 0.051/ - 0.029$ MW/m^2-K (Chen et al., 2011). Thus, for positive applied pressures, the thermal response of the leaky monolayer is consistent with thermal conduction to the gas. The thermal resistance bump near -0.1 MPa comes from the not-yet-understood dip in the thermal resistance near the same pressure. The bilayer and trilayer samples exhibit different behavior. Their interface
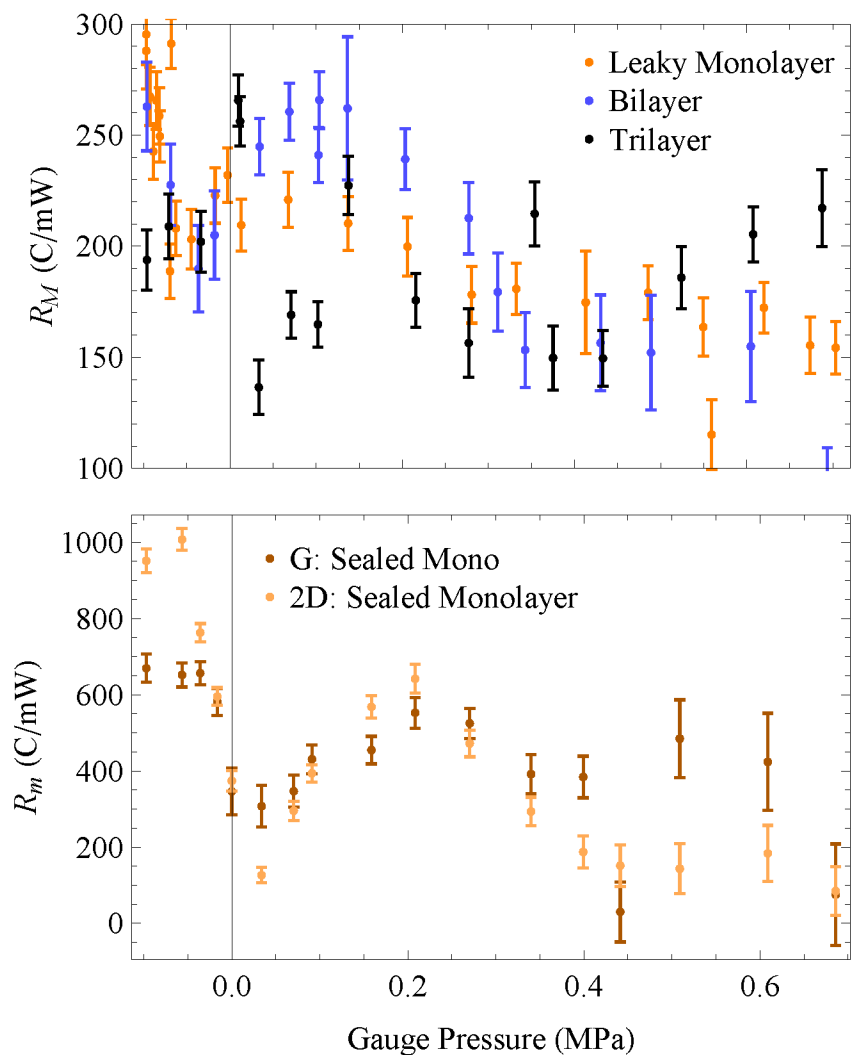
Figure 5.7: Comparison of the pressure dependent measured thermal resistances of sealed monolayer (SB07-1), bilayer (SB08-2), and trilayer (SB03-2) graphene as well as leaky monolayer (FFF) graphene. The thermal resistances of the leaky monolayer was scaled by a factor of 0.28 for easier comparison. Data for the sealed monolayer graphene is plotted separately to better see the trends in the data.
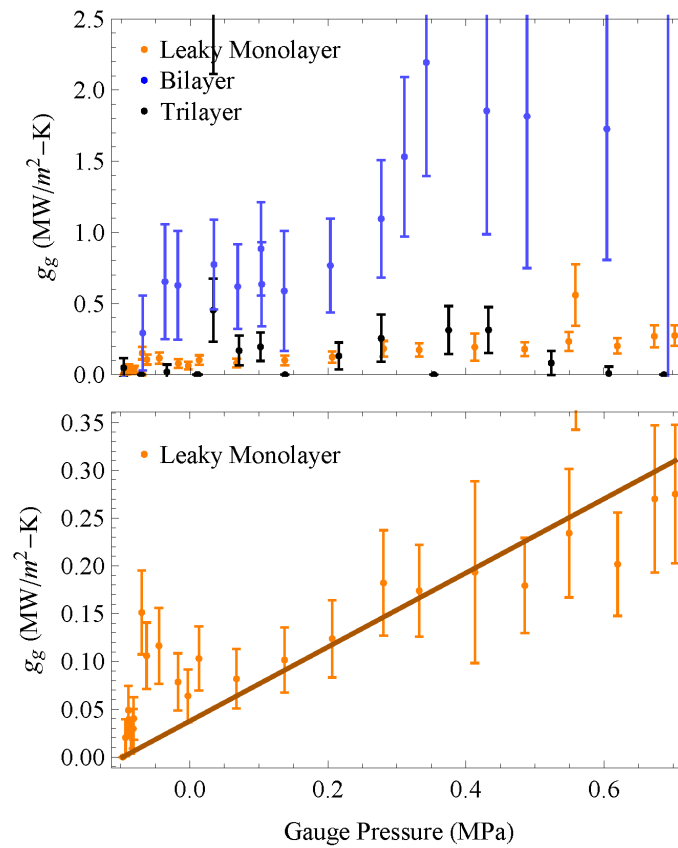
Figure 5.8: Assuming that the in-plane thermal conductivity is constant, the R_M in Figure 5.7 were used to determine the interface thermal conductivity to the gas. The top plot compares the values for a leaky monolayer (FFF), a sealed bilayer (SB08-2), and a sealed trilayer (SB03-2) while the bottom plot shows only the leaky monolayer data fit to a line.

thermal conductivity is higher and behaves less linearly than the leaky monolayer. This is probably due to the gas sealed inside of these microchambers. For low applied gas pressures, the gas in the microchamber conducts much more heat than the gas above the microchamber resulting in a fairly flat pressure response in g_g. For larger pressures, the conduction to the gas above dominates the conduction to the gas below and a stronger pressure response should occur. The flattening out of the pressure response at the highest pressures is not yet understood.

5.3.4 Conclusions

Strain and pressure dependent thermal conductivity measurements were performed on monolayer, bilayer, and trilayer graphene to gain insight into the atypical thermal conductivity in FLG. Strain and pressure are expected to modify the quadratic ZA phonon, believed to be the main contributor to the high thermal conductivity in strained graphene. We found that sealed bilayer and trilayer graphene devices as well as leaky monolayer graphene exhibits measured thermal resistances which decrease with pressure. Heat conduction to the gas, viscous damping of the ZA phonons, or both effects together could cause such a trend. In the case of the leaky monolayer, we showed that the observed thermal resistance is consistent with heat conduction to the gas. The interpretation of the sealed bilayer and trilayer samples, however, was complicated by the gas sealed inside of the microchambers. Measurements of leaky bilayer and leaky trilayer could eliminate this complication in the future. Regretfully, the results for sealed monolayer graphene were indecipherable because of optical interference. In future measurements microchambers should be fabricated much deeper to eliminate these effects.

We did not observe the predicted strain induced transition to divergent thermal conductivity (Bonini et al., 2012; Pereira and Donadio, 2013) in any of our devices.

This might be because we did not reach high enough strains, because the strain distributions which develop in graphene sealed microchambers are not suitable, or possibly because the predictions are incorrect.

Chapter 6

Phonon induced band gap in graphene

Graphene's conspicuous lack of an electrical band gap prevents it from being used in transistor applications which require a large on/off ratio. As such, there has been a large effort to induce an electrical band gap. Groups have generated a 25 meV gap by placing graphene on hexagonal boron nitride breaking the A, B sub-lattice symmetry (Hunt et al., 2013), generated a tunable gap of up to 250 meV by applying an out-of-plane electrical field to bilayer graphene (Zhang et al., 2009), and theorists have predicted that electron confinement in graphene nanoribbons should generate a bulk band gap (Castro Neto et al., 2009). Iadecola and co-workers recently proposed an alternative, dynamic method of gapping graphene (Iadecola et al., 2013a; Iadecola et al., 2013b). They showed that when graphene is pushed out of equilibrium by exciting a particular optical phonon, the electrical band structure exhibits a gap.

In this chapter we consider the effects of these distortions in the frame work of a Peierls transition and discuss the prospects of measuring the induced band gap. This discussion represents the opposite limit of Chapters 3 and 5 where the effect of long wavelength lattice distortions on graphene's electrical and thermal properties were discussed.

6.1 Theory

In this section we briefly discusse Iadecola and coworker's theory of the phonon induced band gap in graphene using the framework of a Peierls transition. Although the real space approach is slightly different, the results are in agreement with Iadecola and coworkers.

When considering how these phonon modes affect the electronic dispersion, we will use the Born-Oppenheimer approximation. According to this approximation, the fast electrons react instantaneously to the slow, phonon induced modifications of the lattice. This allows the modified electronic dispersion to be calculated assuming the lattice is frozen in sequential snapshots. In this section this calculation is done using a tight binding model in the expanded unit cell of the deformed lattice. It is performed in two parts. First, the effects of the change in lattice periodicity are discussed including a discussion of the zone folded electrical dispersion. Second, it is shown that by perturbing the zone folded Hamiltonian, the phonons gap the electronic dispersion.

6.1.1 The Kekulé phonon

The phonon which induces the electrical band gap is the so-called Kekulé phonon (Hou et al., 2007), the highest energy optical phonon at the $\boldsymbol{K}$ point. Displacement vectors describe the eigenmode of this phonon by detailing the displacements of the atoms in the A and B sub-lattices originally at position $\vec{r}_{A,B}$

$$u^{A,B}(\vec{r}_{A,B}, t) = \frac{1}{2} c \, e^{i\vec{r}_{A,B} \cdot \boldsymbol{K}} e^{-i\omega t} \begin{pmatrix} 1 \\ \mp i \end{pmatrix} + \text{c.c.} , \qquad (6.1)$$

where the top sign corresponds to the A sub-lattice and the bottom sign corresponds to the B sub-lattice. Here c is the amplitude, ω is the frequency of the phonon, and t is time. Snapshots showing the time dependence of the resulting lattice distortion are shown in Figure 6.1. The atoms in each sub-lattice rotate around their equilibrium positions without ever returning to their equilibrium position. Atoms in the A sub-lattice are left handed, rotating in the clockwise direction while the atoms in the B sub-lattice are right handed. At $\omega t = \{90°, 210°, 330°\}$ adjacent A and B sub-lattice atoms form well ordered dimers with their nearest neighbors. In the intervening time the system remains partially dimerized. This dimerization is similar to the Peierls distortion in polyacetylene, except that in this two dimensional analog, the system does not gap spontaneously. Instead the phonon must be continuously excited to maintain the gap in graphene.

The time reversed pair of the $\boldsymbol{K}$ Kekulé phonon and the $\boldsymbol{K'}$ Kekulé phonon exhibits a similar distortion with sub-lattices rotating with opposite handedness. The resulting electrical dispersion is the same for either mode so for simplicity we concentrate only on the $\boldsymbol{K}$ phonon. However, if both $\boldsymbol{K}$ and $\boldsymbol{K'}$ modes are excited simultaneously, the opposite circular polarizations sum to linear polarized atomic motion with only temporary dimerization and no sustained band gap. Thus, the experimental realization of this effect requires the exclusive excitation of the $\boldsymbol{K}$, or the $\boldsymbol{K'}$ Kekulé phonon.

6.1.2 Kekulé geometry

The Kekulé distortion causes an expansion of the unit cell, a reduction of the BZ, and a modification of the primitive lattice vectors and reciprocal lattice vectors. When referencing this new geometry back to graphene's intrinsic geometry, the notation previously developed in Chapter 2 is used. The expanded periodicity of the Kekulé
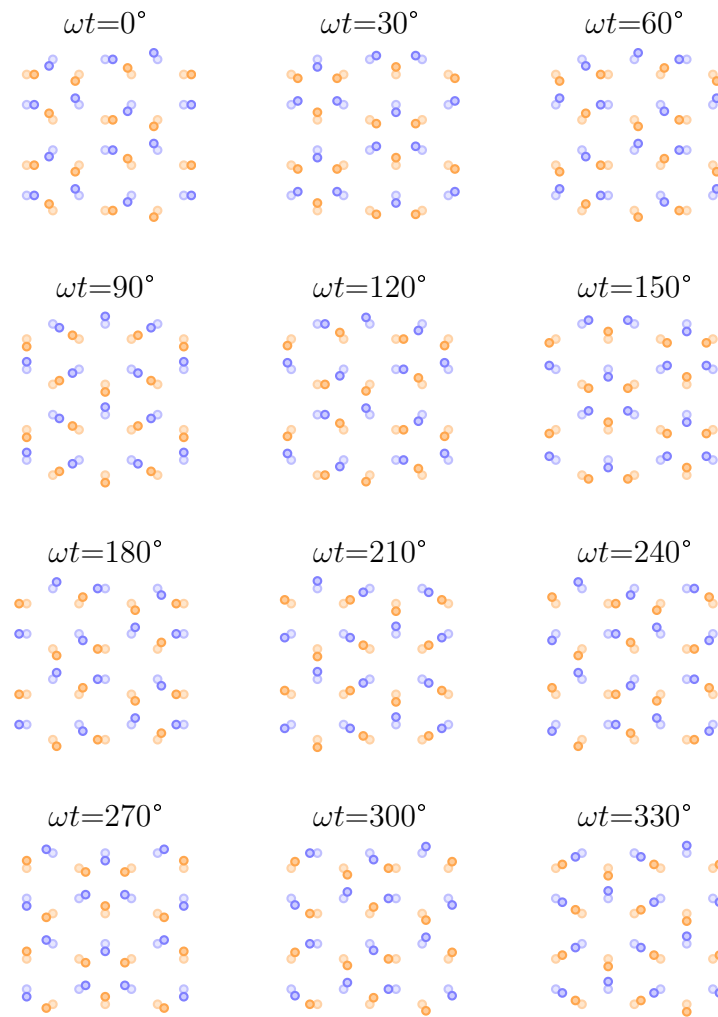
Figure 6.1: Snapshots of the Kekulé phonon mode spanning one period of oscillation. The A sub-lattice is in orange and the B sub-lattice in blue. Faded dots indicating the intrinsic graphene lattice are included for reference.
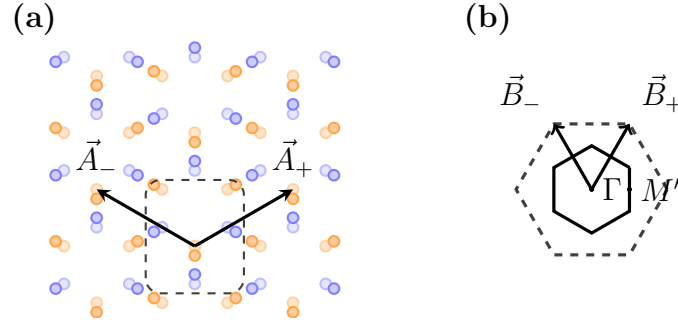
Figure 6.2: The real space (a) and reciprocal space (b) geometry of the Kekulé lattice. (a) shows a snapshot of the atomic positions with the A sub-lattice in orange and the B sub-lattice in blue. For reference, the intrinsic graphene lattice is shown using faded dots. The dashed rectangle outlines the time independent unit cell and the labeled arrows represent the primitive lattice vectors. In (b) the dashed hexagon indicates the BZ of intrinsic graphene while the hexagon with solid lines indicates the shrunken BZ of the Kekulé lattice. The primitive reciprocal lattice vectors are labeled along with select high symmetry points.

lattice is determined by the periodicity of the distortion in Equation 6.1. This term repeats whenever

$$2\pi = \vec{r}_{A,B} \cdot \boldsymbol{K} = (m\vec{a}_+ + n\vec{a}_-) \cdot (\vec{b}_+ - \vec{b}_-)/3 = \frac{2\pi}{3}(m - n) \ ,$$

where m and n are integers. Thus, at any snapshot in time the electrons see the expanded six atom unit cell shown in Figure 6.2. This tripled unit cell is time independent; it never returns to the intrinsic two atom basis.

The primitive lattice vectors of the Kekuleé lattice,

$$\vec{A}_+ = 2\vec{a}_+ - \vec{a}_- = \frac{3a}{2}(+\sqrt{3}, 1)$$
$$\vec{A}_- = 2\vec{a}_- - \vec{a}_+ = \frac{3a}{2}(-\sqrt{3}, 1) ,$$

represent a triangular lattice rotated by 90 degrees and expanded by a factor of $\sqrt{3}$ relative to the intrinsic lattice. This tripling of the area of the unit cell is accompanied by a corresponding decrease in the area of the BZ as shown in Figure 6.2. The primitive reciprocal lattice vectors,

$$\vec{B}_+ = \frac{1}{3}(2\vec{b}_+ + \vec{b}_-) = \frac{2\pi}{3\sqrt{3}a}(+1, \sqrt{3})$$
$$\vec{B}_- = \frac{1}{3}(2\vec{b}_- + \vec{b}_+) = \frac{2\pi}{3\sqrt{3}a}(-1, \sqrt{3}) ,$$

generate a hexagonal BZ rotated 90 degrees with an area shrunk by a factor of three relative to the intrinsic lattice BZ. Three equivalent corners of the BZ are positioned at

$$\frac{2\pi}{9a}(-\sqrt{3}, -1), \quad \frac{2\pi}{9a}(+\sqrt{3}, -1), \quad \text{and} \quad \frac{2\pi}{9a}(0, 2) .$$

Unlike for intrinsic graphene, the interesting physics occurs near the center of the BZ. Hence, the periodicity of the phonon fully describes the geometry of the expanded lattice.

6.1.3 Zone folding

When the BZ is reduced in size, the number of bands in the electronic dispersion is increased. Energy bands outside the new BZ are folded into the new BZ by translation by reciprocal lattice vectors. Since the size of BZ is reduced by a factor of three, there

(a) Zone Fold 1   **(b) Zone Fold 2**
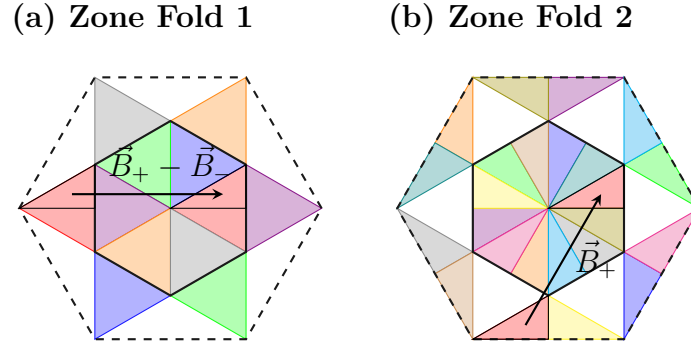
Figure 6.3: The two distinct zone foldings introduced by the Kekulé distortion: Zone fold 1 (a) and zone fold 2 (b). The outer, dashed hexagon is the BZ of intrinsic graphene and the inner hexagon with solid lines is the new BZ of the Kekulé lattice. The symmetry reduced area represented by the black outlined triangle is translated into the new BZ by different reciprocal lattice vectors (labeled) for the two folding schemes.

are two zone folding schemes resulting in six energy bands.

The zone folding schemes shown in Figure 6.3 describe the two distinct ways the symmetry reduced area of the new BZ can be mapped onto via translations of reciprocal lattice vectors. The rest of the BZ can be constructed using symmetry operations on the symmetry reduced area. In both zone folding schemes, the Dirac point is translated from the corner of the old BZ to the zone center of the new BZ making the Γ point the most interesting point in the new BZ. It is also worth noting that the right edge of the symmetry reduced area in zone fold 1 shares its right edge with the symmetry reduced area already inside the new BZ. Also, the top edge of the symmetry reduced area is shared between zone fold 1 and zone fold 2.

The hierarchy of the folded energy bands can be determined by comparing the zone folded areas to the electronic dispersion of intrinsic graphene shown in Figure 2.2.

The lowest and highest energy bands will correspond to the unfolded area because the new BZ occupies the basin in the intrinsic graphene dispersion. Zone fold 1 extends further into the basin of intrinsic graphene's dispersion than zone fold 2 and so gives the second lowest and second highest energy bands. Finally, the zone fold 2 gives the two middle energy bands.

The zone folded electronic dispersion can either be calculated by folding the dispersion calculated in Chapter 2 or by performing a tight binding calculation in the expanded unit cell. Although it is more involved, the tight binding calculation will be done here because it will be needed later. In this scheme, each of the six atoms in the unit cell must have its own raising and lowering operator. To simplify this bookkeeping, the operators will be referenced back to the three two-atom-bases which make up the six-atom Kekulé basis. These two-atom-bases are shown in Figure 6.4. The operators $a_{i,l}$ and $b_{i,l}$ are then the lowering operators for the three A sub-lattice atoms and the three B sub-lattice atoms in the lth Kekulé basis respectively. The index i run over the three two atom bases. In this notation the real space nearest neighbor tight binding Hamiltonian is given by

$$
\begin{aligned}
H = -\sum_l (&t a_{1,l}^\dagger b_{1,l} + t a_{1,l}^\dagger b_{2,l} + t a_{1,l}^\dagger b_{3,l} \\
&+ t a_{2,l}^\dagger b_{1,l\uparrow} + t a_{2,l}^\dagger b_{2,l} + t a_{2,l}^\dagger b_{3,l\rightarrow} \\
&+ t a_{3,l}^\dagger b_{1,l\uparrow} + t a_{3,l}^\dagger b_{2,l\leftarrow} + t a_{3,l}^\dagger b_{3,l} + \text{H.C.}) \ .
\end{aligned}
\tag{6.2}
$$

Later the hopping energies t will be made bond dependent to account for the altered nearest neighbor distances. In the meantime the bond independent hopping energy of intrinsic graphene, t_0, will be used.

Similarly to intrinsic graphene, the individual terms in the sum can be simplified
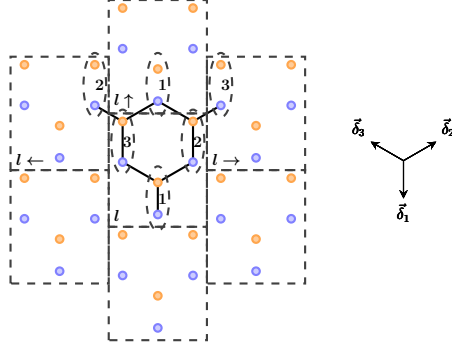
Figure 6.4: The hoppings included in the Hamiltonian connect atoms originally from the A sub-lattice (orange) to atoms originally from the B sub-lattice (blue). They can pass between the labeled intrinsic unit cells (dashed ellipses) and they can also pass between the labeled extended unit cells (dashed rectangles). For reference the directions of the nearest neighbor vectors are included.

by writing the operators in Fourier space,

$$a_{m,l}^\dagger = \frac{1}{\sqrt{N}} \sum_{\vec{k}} e^{i\vec{k}\cdot\vec{R}_l} a_{m,\vec{k}}^\dagger \ , \tag{6.3}$$

where we are expanding about the positions of the Kekulé unit cells. The individual terms are then

$$-t_0 \sum_l a_{m,l}^\dagger b_{m',l'} = -\frac{t_0}{N} \sum_l \sum_{\vec{k},\vec{k}'} a_{m,\vec{k}}^\dagger b_{m',\vec{k}'} e^{i\vec{R}_l\cdot(\vec{k}-\vec{k}')} e^{i(\vec{R}_l-\vec{R}'_l)\cdot\vec{k}'}$$

$$= -t_0 \sum_{\vec{k}} a_{m,\vec{k}}^\dagger b_{m',\vec{k}} \underbrace{e^{i(\vec{R}_l-\vec{R}'_l)\cdot\vec{k}'}}_{s_{l-l'}} \ ,$$

which is only dependent on the l independent distance $l - l' \in \{0, \leftarrow, \uparrow, \rightarrow\}$ between the Kekulé unit cells that are being hopped between.

The Hamiltonian can then be expressed in matrix form as

$$H_0 = -t_0 \sum_{\vec{k}} \psi^\dagger \begin{pmatrix} 0 & 0 & 0 & s_0 & s_0 & s_0 \\ 0 & 0 & 0 & s_\uparrow & s_0 & s_\rightarrow \\ 0 & 0 & 0 & s_\uparrow & s_\leftarrow & s_0 \\ s_0^* & s_\uparrow^* & s_\uparrow^* & 0 & 0 & 0 \\ s_0^* & s_0^* & s_\leftarrow^* & 0 & 0 & 0 \\ s_0^* & s_\rightarrow^* & s_0^* & 0 & 0 & 0 \end{pmatrix} \psi \ , \tag{6.4}$$

where $\psi^\dagger = \left(a_1^\dagger, a_2^\dagger, a_3^\dagger, b_1^\dagger, b_2^\dagger, b_3^\dagger \right)$. The 6X6 Hamiltonian will provide six energy levels as expected.

The resulting electronic dispersion is shown in Figure 6.5. To best show the shapes of the bands, the dispersion is plotted both over the full Kekulé BZ and also over only the symmetry reduced area. The six energy bands are clearly visible with the highest and lowest energy bands appearing as caps. As expected the Dirac point has been shifted to zone center where the four middle bands converge to touch at a single point. In agreement with the zone folding schemes the highest energy band is degenerate with the second highest energy band on the BZ border. Also, the second and third highest energy bands are degenerate along the lines connecting the Γ point to the corner of the BZ. The electronic dispersion calculated with a tight binding model of the expanded unit cell agrees with our zone folding predictions.

6.1.4 Altered hoppings

The excitation of the Kekulé phonon mode does more than just enlarge the unit cell, it also modifies the hopping energies. This is similar to the case of strained graphene where the altered bond lengths caused altered hopping energies and generated new
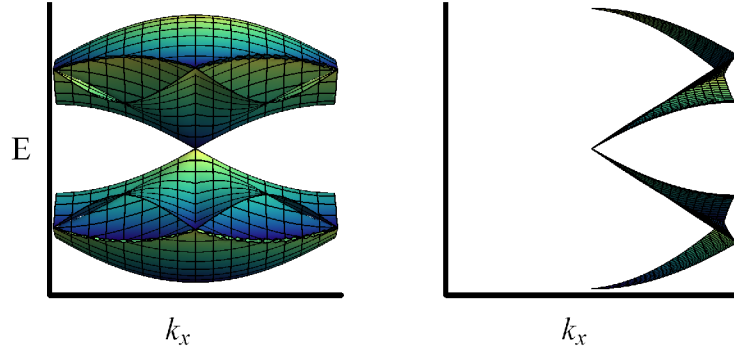
Figure 6.5: Surface plots of the folded electronic dispersion of the Kekulé lattice including all six energy bands. In the left plot the surfaces are plotted for the full Kekulé BZ whereas in the right plot only the symmetry reduced area is plotted. In the symmetry reduced plot, the middle bands split in the k_y direction.

physics. In this case, however, the bond lengths vary with a much higher spatial frequency and the slowly varying approximation described in Appendix B is not applicable. This coupling will generate a band gap at the Γ point of the zone folded dispersion.

Iadecola et $al.$ showed that the bond length alterations generate hopping alterations,

$$\delta t_{m,j} = \frac{1}{3}\Delta(t)e^{i\boldsymbol{K}\cdot\vec{\delta}_j}e^{i\boldsymbol{G}\cdot\vec{r}_m} + \text{c.c.}$$

$$\text{with } \Delta(t) = -i3\beta t_0\frac{c^*}{a}e^{i\omega t} \, , \tag{6.5}$$

which have a spatial frequency component of $\boldsymbol{G} = \boldsymbol{K} - \boldsymbol{K}'$ that couples the Dirac points (Iadecola et al., 2013a). Here $\vec{r}_m$ is the position of the A sub-lattice atom involved in the hopping. Index m indicates which of the three intrinsic unit cells embedded in the enlarged Kekulé unit cell the atom is in. The B sub-lattice atom is

specified through $\vec{\delta}_j$, the unperturbed nearest neighbor vector which connects the A sub-lattice atom to the B sub-lattice atom. Figure 6.4 summarizes these indices. For completeness, the calculation of Equation 6.5 is included in Appendix E. It is worth noting that the Cauchy-Born rule cannot be used here as it was in Section 3.1.2. This is because the iTO phonon causes the atoms in the A and B sub-lattices to rotate in opposite directions, an effect which is not captured in the Cauchy-Born frame work which requires that the sub-lattices act identically.

6.1.5   Tight binding of the expanded Kekulé lattice

The Kekulé mode causes the hopping energies in Equation 6.2 to be bond and time specific. Taking $t = t_0 + \delta t_{m,j}$ with $\delta t_{m,j}$ defined in equation 6.5 breaks Equation 6.2 into two pieces. The first, corresponding to t_0, is just the zone folding Hamiltonian in Equation 6.4. The second is the perturbation which opens the band gap.

Similar to the individual terms in H_0, each term in the perturbed Hamiltonian, H', can be simplified by writing the operators in Fourier using Equation 6.3

$$-\delta t_{m,j} \sum_l a^\dagger_{m,l} b_{m',l'} = -\frac{\delta t_{m,j}}{N} \sum_l \sum_{\vec{k},\vec{k}'} a^\dagger_{m,\vec{k}} b_{m',\vec{k}'} e^{i\vec{R}_l\cdot(\vec{k}-\vec{k}')} e^{i(\vec{R}_l-\vec{R}'_l)\cdot\vec{k}'}$$

$$= -\sum_{\vec{k}} a^\dagger_{m,\vec{k}} b_{m',\vec{k}} \underbrace{\delta t_{m,j} e^{i(\vec{R}_l-\vec{R}'_l)\cdot\vec{k}}}_{g_{m,j,l-l'}} \ .$$

In addition to the l independent distance between involved Kekulé unit cells, each term depends on m which indicates the old, two atom unit cell which the A sub-lattice atom occupies, and j which indicates which $\vec{\delta}_j$ the hopping is along. The associated vectors are $\vec{R}_l - \vec{R}'_l \in \{0, \vec{A}_+, \vec{A}_+ + \vec{A}_-, \vec{A}_-\}$ and $\vec{r}_m \in \{0, \vec{a}_+, \vec{a}_-\}$.

The perturbed Hamiltonian can then be constructed using Figure 6.4,

$$H' = -\frac{1}{3}\sum_{\vec{k}} \psi^\dagger \begin{pmatrix} 0 & 0 & 0 & g_{1,1,0} & g_{1,2,0} & g_{1,3,0} \\ 0 & 0 & 0 & g_{2,3,\uparrow} & g_{2,1,0} & g_{2,2,\rightarrow} \\ 0 & 0 & 0 & g_{3,2,\uparrow} & g_{3,3,\leftarrow} & g_{3,1,0} \\ g^*_{1,1,0} & g^*_{2,3,\uparrow} & g^*_{3,2,\uparrow} & 0 & 0 & 0 \\ g^*_{1,2,0} & g^*_{2,1,0} & g^*_{3,3,\leftarrow} & 0 & 0 & 0 \\ g^*_{1,3,0} & g^*_{2,2,\rightarrow} & g^*_{3,1,0} & 0 & 0 & 0 \end{pmatrix} \psi \ .$$

Using the Born-Oppenheimer approximation the electronic dispersion of the total Hamiltonian, $H = H_0 + H'$, can now be calculated at any snapshot in time. In this approximation it turns out that the dispersion is time independent. Figure 6.6 shows the electronic dispersion along the Γ to M' direction for a lattice distortion of $c^*/a = 1\%$. It is clear that the modified hoppings which couples the $\boldsymbol{K}$ point to the $\boldsymbol{K'}$ point opens a band gap at the charge neutrality point. The gap has a width of $2|\Delta|$ where Δ is given in Equation 6.5. The inner two bands are gapped equally, maintaining there degeneracy at the Γ point.

The generation of the band gap is not an artifact of the Born-Oppenheimer approximation. Iadecola and coworkers solved the time dependent Hamiltonian in the low energy limit by absorbing the time dependence of Δ in a pseudo spin rotation. The resulting Hamiltonian has the same time independent band gap of $2|\Delta|$. The electronic response and system bath coupling are both conserved by this rotation ensuring that the gap could be measured in an electrical transport experiment (Iadecola et al., 2013a). They were additionally able to use this fairly simple system to gain insight into the Floquet formalism used to study more difficult driven solid state systems (Iadecola et al., 2013b).
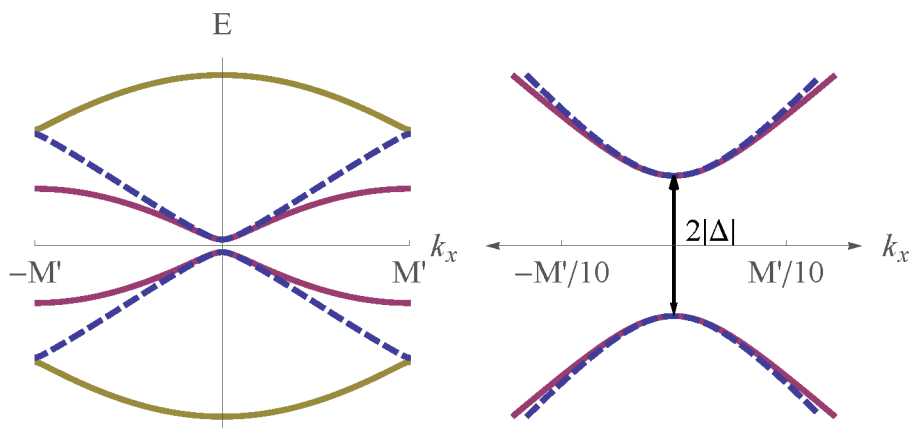
Figure 6.6: The electronic dispersion of the Kekulé lattice along the Γ to M' direction for a lattice distortion of $c^*/a = 1\%$. The plot on the right focuses on the 310 meV energy gap at the Γ point.

The origins of this gapped phase are very similar to the origin of the band gap in polyacetylene. The system is continuously dimerized, necessitating an expanded unit cell. Expanding the unit cell requires a shrinking of the BZ and a zone folding of the dispersion. Finally, the lattice modifications induce couplings which open a band gap. The only difference with polyacetylene is that the gap in graphene does not form spontaneously. Instead, phonons must be continuously created to maintain this gap in the system.

6.2   Measurement prospects

An experimental measurement of the phonon induced band gap has two components: The excitation of the phonon and the measurement of the resulting band gap. The former is the more difficult of the two; the electrical transport measurements described

in Appendix F can be used to measure the resulting band gap. The large momentum and energy associated with the Kekulé phonon makes their excitation using surface accoustic waves, evanescent fields, surface plasmons, or temperature impractical. In this section we discuss the prospects of directly exciting the Kekulé phonon using a neon seeded helium beam.

To determine the feasibility of this measurement we will estimate the expected band gap. The size of the band gap is estimated in three steps. The band gap is related to atomic displacements, the atomic displacements are related to the number of phonons, and the number of phonons is estimated based on the phonon generating neon flux and the phonon persistence time. Based on Equation 6.5, the band gap is given by

$$E_g = 2|\Delta| = 6\beta t_0 \frac{|c|}{a} \approx 50 \ eV \ \frac{|c|}{a} \ ,$$

where $|c|$ is the amplitude of the phonon oscillation. In a semi-classical approximation $|c|$ is related to the number of phonons, n, through

$$N \frac{1}{2} M \omega^2 |c|^2 = n\hbar\omega$$

$$\rightarrow |c| = \sqrt{\frac{2\hbar}{M\omega}} \sqrt{\frac{n}{N}} \approx 0.1 \ \text{Å} \ \sqrt{\frac{n}{N}} \ ,$$

where n is the total number of excited Kekulé phonons in the system, N is the number of unit cells illuminated by the neon seeded helium beam, M is the mass of a carbon atom, and ω is the frequency of the Kekulé phonon. Thus, the band gap is related to the number of phonons by

$$E_g = 6\beta t_0 \sqrt{\frac{2\hbar}{M\omega}} \sqrt{\frac{n}{a^2 N}} \approx 50 \ eV \ 0.1 \ \text{Å} \ \sqrt{\frac{n}{A}} \ .$$

Assuming that the the graphene sample is fully illuminated, $a^2N = A$ is roughly the area of the graphene sheet. Finally, the number of excited phonons can be calculated using the steady state solution to the rate equation

$$\frac{dn}{dt} = f\eta A - \frac{n}{\tau} = 0 \; ,$$

where $f \approx 10^{18} \; atoms/m^2/s$ is the neon flux, $\eta \geq 10^{-2}$ is the phonon scattering efficiency, and τ is the persistence time of the phonon. The persistence time is longer than the phonon lifetime because not all phonon decay channels result in fewer phonons. For instance, if a phonon decays into an electron hole pair, that electron hole pair can recombine and replace the original phonon. The phonon lifetime can, however, be used to estimate a lower bound for the band gap. For a phonon lifetime of 0.2 ps estimated based on the 27 cm^{-1} line width of the Raman 2D feature, the expected band gap is

$$gap \geq 6\beta t_0 \sqrt{\frac{2\hbar}{M\omega}} \sqrt{f\eta\tau} \approx 50 \; eV \; 10^{-11} \; m \; 10 \; \frac{1}{m} \approx 5 \; neV \; .$$

This illustrates the difficulty in creating a sufficient number of phonons to open a measurable band gap. If the persistence time were a factor of 10^{12} longer than the phonon lifetime ($\tau \approx 0.2 \; s$), the system would reach a continuous bandgap of roughly 5 meV measurable at room temperature. This seemingly unending lifetime is not entirely outside the range of possibility. Acoustic phonons have lifetimes on this order. A more detailed calculation of the Kekulé phonon decay channels is necessary for a better estimation of the phonon persistence time and the expected band gap.

In the case of short persistence times it makes sense to think of the system stochastically. A neon atom would hit a 10 μm^2 sample and create a phonon every 10 μs

based on f and η. If $\tau << 10$ μs the system would spend most of its time in its unexcited, ungapped, instrinsic state. Assuming that the coherence length of the phonon covers the whole sample, phonon creation events would cause temporary transitions to a gapped state. For the 10 μm^2 sample with 2×10^8 unit cells, a single phonon excitation would correspond to a band gap of roughly 0.5 meV or 6 Kelvin. Liquid helium temperature electrical transport could be used to measured a gap of this magnitude. However, for a persistence time on the order of picoseconds, the system is only gapped a factor of 10^{-6} of the time. A possible method to overcome this signal to noise issue would be to chop the helium neon excitation beam and lock the electrical transport measurements in to the chopping frequencies.

6.3 Summary

The theory behind the phonon induced band gap was developed in the frame work of the Peierls transition. It was shown that exciting the phonon reduces the size of the BZ and couples the $\boldsymbol{K}$ and $\boldsymbol{K'}$ creating a band gap. The experimental measurement of this exciting physical phenomena is challenging because of the difficulty in exciting a sufficient number of optical phonons.

Chapter 7

Conclusion

This thesis includes a number of new contributions to the field of manipulated graphene. For long wavelength manipulations in the form of strain, new terms in the pseudovector potential were found and new pseudomagnetic field devices were proposed. The method of engineering the strain fields required for pseudomagnetic fields was studied in the context of the sliding friction between graphene and a SiO_2 substrate. This included the discovery of the anomalous, strain dependent, macroscopic sliding friction. Using the same experimental geometry used to study friction, we probed the mechanism behind graphene's very high thermal conductivity. Finally, the prospects of measuring the band gap activated by the phonon induced short wavelength distortions of graphene's lattice were discussed. These studies which ranged from the mechanical, to the optical, and to the thermal properties of graphene demonstrated how graphene's impressive properties can be extended in new and exciting directions by manipulating its lattice.

Appendix A

The first Brillouin zone of strained graphene

In this appendix an approximate analytic expression for the positions of the corners of the BZ of deformed graphene is presented. The BZ can then be constructed by connecting these points. The strain dependence is found by applying a general method for determining the positions of the BZ corners for close to hexaganal lattices:

1. The lattice vectors are used to determine the reciprocal lattice vectors.

2. The combination of reciprocal lattice vectors which give the important points in reciprocal space are determined.

3. The conditions for Bragg refraction will be used to determine the corners of the BZ.

After establishing this general methodology, the explicit strain dependence can easily be determined to first order.

The lattice vectors $\vec{a}_+$ and $\vec{a}_-$ determine the reciprocal lattice vectors through the relationship $\vec{a}_i \cdot \vec{b}_j = 2\pi \delta_{ij}$, where $\vec{b}_j$ are the two reciprocal lattice vectors, i and j are $\in \{+, -\}$, and δ_{ij} is the Kronecker delta function (Kittel, 2005). In two dimensions

this can be cast as a a matrix relationship,

$$
\begin{pmatrix} a_{\pm x} & a_{\pm y} \\ a_{\mp x} & a_{\mp y} \end{pmatrix} \begin{pmatrix} b_{\pm x} \\ b_{\pm y} \end{pmatrix} = \begin{pmatrix} 2\pi \\ 0 \end{pmatrix} ,
\tag{A.1}
$$

which can be easily solved by inverting the matrix. Having determined the form for the reciprocal lattice vectors, the next step is to determine the boundaries of the BZ.

The traditional method of determining the BZ does not lend itself to simple algorithmic implementation. In this method, one draws the perpendicular bisector of each reciprocal lattice vector given by $\vec{G} = n\vec{b}_+ + m\vec{b}_-$ where m and n are integers. The most inner polygon formed by the perpendicular bisectors is then the BZ (Kittel, 2005). The first step to simplify this method is to restrict the number of perpendicular bisectors which are considered. The construction of the BZ using the minimum number of reciprocal lattice vectors is shown for a perfect hexagonal lattice in Figure A.1. This six combinations of reciprocal lattice vectors needed to construct the BZ is relatively robust to distortions of the hexagonal lattice. They determine the BZ for strains as large as 20% armchair uniaxial, 20% armchair uniaxial, or 20% shear strain. The reciprocal lattice vectors themselves are altered by strain but the combinations used to construct the BZ are the same. This was confirmed by comparing the BZ predicted by the method presented here with that calculated using a geometric construction. The phrase "close to hexagonal" lattices is used to refer to those lattice for which the minimal set of reciprocal lattice vectors is given by the combinations shown in Figure A.1. For this discussion, the strained graphene lattice is then a close to hexagonal lattice.
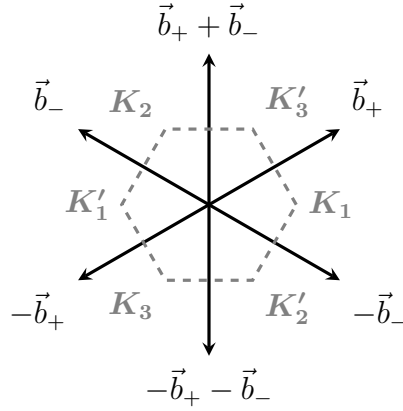
Figure A.1: The construction of the BZ for a hexagonal lattice. The edges of the BZ (dashed, gray) are made up of the perpendicular bisectors of the labeled reciprocal lattice vectors (black, arrows). Close to hexagonal lattices are lattices for which the same set of reciprocal lattice vectors define the BZ.

Having restricted the reciprocal lattice vectors, the corners of the BZ can be constructed from the condition for Bragg reflection. This condition,

$$\vec{k} \cdot \left(\frac{1}{2}\vec{G}\right) = \left(\frac{1}{2}\vec{G}\right)^2 ,$$

defines the wave vectors, $\vec{k}$, which make up the perpendicular bisector of the reciprocal lattice vector (Kittel, 2005). The corners of the BZ can be found by noticing that if the wave vector is on the perpendicular bisector sequential reciprocal lattice vectors in Figure A.1, it is a corner of the BZ. For example, the corner $\boldsymbol{K}_1$ is a perpendicular bisector of both $-\vec{b}_-$ and $\vec{b}_+$. Thus, the corners of the BZ can be calculated analytically by using the matrix identity,

$$\begin{pmatrix} G_{1,x} & G_{1,y} \\ G_{2,x} & G_{2,y} \end{pmatrix} \begin{pmatrix} k_x \\ k_y \end{pmatrix} = \begin{pmatrix} \frac{1}{2}G_1^2 \\ \frac{1}{2}G_2^2 \end{pmatrix} \tag{A.2}$$

where $\vec{G}_1$ and $\vec{G}_2$ are sequential reciprocal lattice vectors from Figure A.1. This matrix identity can be inverted to determine the wave-vector at the corner of the BZ. This completes the general methodology for determining the BZ based on the lattice vectors for close to hexagonal lattices. In summary, the reciprocal lattice vectors are calculated from the lattice vectors using Equation A.1 and then the corners of the BZ can be found using Equation A.2 for the reciprocal lattice vector combination shown in Figure A.1.

The final step is to calculate the positions of the BZ corners using the form of the strained lattice vectors in Equation 3.3. The first order approximation found using Wolfram Mathematica version 9.0 is

$$
\begin{aligned}
\boldsymbol{K}_1 = -\boldsymbol{K}_1' &\simeq \frac{4\pi}{3\sqrt{3}a} \begin{pmatrix} 1 \\ 0 \end{pmatrix} + \frac{4\pi}{3\sqrt{3}a} \begin{pmatrix} -\frac{1}{2}u_{xx} - \frac{1}{2}u_{yy} \\ -\frac{1}{2}u_{yx} - \frac{3}{2}u_{xy} \end{pmatrix} \\
\boldsymbol{K}_2 = -\boldsymbol{K}_2' &\simeq \frac{4\pi}{3\sqrt{3}a} \begin{pmatrix} -\frac{1}{2} \\ \frac{\sqrt{3}}{2} \end{pmatrix} + \frac{4\pi}{3\sqrt{3}a} \begin{pmatrix} u_{xx} - \frac{1}{2}u_{yy} - \frac{\sqrt{3}}{2}u_{yx} \\ -\frac{\sqrt{3}}{2}u_{yy} - \frac{1}{2}u_{yx} \end{pmatrix} \\
\boldsymbol{K}_3 = -\boldsymbol{K}_3' &\simeq \frac{4\pi}{3\sqrt{3}a} \begin{pmatrix} -\frac{1}{2} \\ -\frac{\sqrt{3}}{2} \end{pmatrix} + \frac{4\pi}{3\sqrt{3}a} \begin{pmatrix} u_{xx} - \frac{1}{2}u_{yy} + \frac{\sqrt{3}}{2}u_{yx} \\ \frac{\sqrt{3}}{2}u_{yy} - \frac{1}{2}u_{yx} \end{pmatrix}
\end{aligned}.
$$

The shifts in the corners of the BZ are opposite for time reversal pairs respecting time reversal symmetry. The positions of the corners are determined by the terms of the displacement gradient tensor and not the strain tensor. These approximation were successfully tested against the geometric construction. They are used in Chapter 3 to visualize the distortion of Reciprocal space which accompanies the deformation of the real space lattice. In particular, Figure 3.2 shows the shifts in the corners of the BZ for several deformation geometries.

Appendix B

Slowly varying approximation

The pseudovector potential interpretation of strain developed in Chapter 3 is an approximation to a full rigorous treatment of a non-uniform strain field. In a strict treatment of non-uniform strain the i dependencies of Equation 3.6 cannot be neglected and the transformation into Fourier space is obstructed. Without elimination of the spatial dependence, the Hamiltonian of the full system must be painstakingly solved. In this case, pseudomagnetic field phenomena would be captured by a Landau level quantized density of states. Although rigorous, this method is more arduous and also less conceptually pleasing. In the slowly varying approximation the i dependencies in Equation 3.6 are eliminated. In this approximation the pseudovector potential formalism is valid, providing a qualitative framework for understanding the observed effects. In this Appendix this approximation will be developed and the limits of validity will be discussed.

Remembering that $\boldsymbol{\nabla u}$ is i dependent, the i dependent terms in Equation 3.6 are

$$
\begin{aligned}
H_i &= \sum_i \left(t_0 + \delta t_{i,j}\right) e^{i(\vec{k}-\vec{k}')\cdot\vec{R}_i'} e^{-i\vec{k}'\cdot\vec{\Delta}_{i,j}'} \\
&= \sum_i \left(t_0 + \delta t_{i,j}\right) e^{i(\vec{k}-\vec{k}')\cdot\vec{R}_i'} e^{-i\vec{k}'\cdot(\mathbf{1}+\boldsymbol{\nabla u})\vec{\Delta}_j} \\
&\simeq e^{-i\vec{k}'\cdot\vec{\Delta}_j} \sum_i \left(t_0 + \delta t_{i,j}\right) e^{i(\vec{k}-\vec{k}')\cdot\vec{R}_i'} \left(1 - i\vec{k}'\cdot\boldsymbol{\nabla u}\cdot\vec{\Delta}_j\right) \\
&\simeq e^{-i\vec{k}'\cdot\vec{\Delta}_j} \left\{ t_0 \sum_i e^{i(\vec{k}-\vec{k}')\cdot\vec{R}_i'} - i t_0 \vec{k}' \cdot \sum_i \left(\boldsymbol{\nabla u}\, e^{i(\vec{k}-\vec{k}')\cdot\vec{R}_i'}\right)\cdot\vec{\Delta}_j + \sum_i \delta t_{i,j}\, e^{i(\vec{k}-\vec{k}')\cdot\vec{R}_i'} \right\} \\
&= e^{-i\vec{k}'\cdot\vec{\Delta}_j} \left\{ N t_0 \delta_{\vec{k},\vec{k}'} - i t_0 \vec{k}' \cdot \widetilde{\boldsymbol{\nabla u}}_{\vec{k}-\vec{k}'} \cdot \vec{\Delta}_j + \widetilde{\delta t}_{\vec{k}-\vec{k}'} \right\} \;,
\end{aligned}
$$

where $\widetilde{\boldsymbol{\nabla u}}_{\vec{k}-\vec{k}'}$ and $\widetilde{\delta t}_{\vec{k}-\vec{k}'}$ are the Fourier transforms of $\delta t_{i,j}$ and $\boldsymbol{\nabla u}$ respectively. Only terms first order in products of the small quantities $\boldsymbol{\nabla u}$ and $\delta t_{i,j}$ were kept. All of the i dependence has been absorbed by the Fourier transforms.

Only specific Fourier components yield relevant $\widetilde{\boldsymbol{\nabla u}}_{\vec{k}-\vec{k}'}$ and $\widetilde{\delta t}_{\vec{k}-\vec{k}'}$ when working in the low energy regime. The wave-vectors will again be approximated as $\vec{k} = \boldsymbol{K} + \vec{q}$ and $\vec{k} = \boldsymbol{K}' + \vec{q}$ with the additional small parameter qa, giving

$$
\begin{aligned}
\widetilde{\delta t}_{\vec{k}-\vec{k}'} &= \sum_i \delta t_{i,j} e^{i(\boldsymbol{K}^{(')}+\vec{q}-\boldsymbol{K}^{(')}-\vec{q}')\cdot\vec{R}_i'} \\
&\simeq \sum_i \delta t_{i,j} e^{i(\boldsymbol{K}^{(')}-\boldsymbol{K}^{(')})\cdot\vec{R}_i'} (1 + (\vec{q}-\vec{q}')\cdot\vec{R}_i') \\
&= \sum_i \delta t_{i,j} e^{i(\boldsymbol{K}^{(')}-\boldsymbol{K}^{(')})\cdot\vec{R}_i'} \;,
\end{aligned}
$$

where $\boldsymbol{K}^{(')}$ refers to either $\boldsymbol{K}$ or $\boldsymbol{K}'$ depending on the wave-vector. The low energy approximation for $\widetilde{\boldsymbol{\nabla u}}_{\vec{k}-\vec{k}'}$ is similar. Thus, to first order in the small parameters the only relevant Fourier components are for $\vec{k}-\vec{k}' \in \{0, \boldsymbol{K}-\boldsymbol{K}', \boldsymbol{K}'-\boldsymbol{K}\}$. Interestingly, the high frequency components could act to couple the $\boldsymbol{K}$ and $\boldsymbol{K}'$ points. However,

here we apply the slowly varying approximation for which we eliminate the high frequency components and limit $\vec{k} - \vec{k}' \to 0$, yielding

$$\widetilde{\delta t}_{\vec{k} - \vec{k}'} \simeq N \delta_{\vec{k}, \vec{k}'} (< \delta t_{i,j} >)$$

$$\widetilde{\boldsymbol{\nabla} \boldsymbol{u}}_{\vec{k} - \vec{k}'} \simeq N \delta_{\vec{k}, \vec{k}'} (< \boldsymbol{\nabla} \boldsymbol{u} >) \ .$$

where $< \delta t_{i,j} > = \delta t_j$ and $< \boldsymbol{\nabla} \boldsymbol{u} >$ are the average value over i of $\delta t_{i,j}$ and $\boldsymbol{\nabla} \boldsymbol{u}$ respectively.

Thus, in the slowly varying approximation the i dependence of Equation 3.6 becomes

$$H_i = e^{-i\vec{k}' \cdot \vec{\Delta}_j} \left\{ N \delta_{\vec{k}, \vec{k}'} \left(t_0 + \delta t_j - i t_0 \vec{k}' \cdot \boldsymbol{\nabla} \boldsymbol{u} \cdot \vec{\Delta}_j \right) \right\}$$

which gives the same result as the simple substitutions $\delta t_{i,j} \to \delta t_j = < \delta t_{i,j} >$ and $\boldsymbol{\nabla} \boldsymbol{u}_i \to < \boldsymbol{\nabla} \boldsymbol{u} >$ in Equation 3.6. This approximation required low energies, $qa << 1$, small strains, $\delta t_j << t_0$ and $\boldsymbol{\nabla} \boldsymbol{u} << 1$, and slowly varying strain fields, $\widetilde{\delta t}_{K - K'} = \widetilde{\boldsymbol{\nabla} \boldsymbol{u}}_{K - K'} = 0$. It eliminates the spatial dependence in the Hamiltonian of strained graphene allowing the identification of the pseudovector potential.

Appendix C

Global fitting algorithm

This Appendix is devoted to the method used to extract the fitting parameters from the Raman line scans discussed in Chapter 4. Throughout, fitting parameters refers to the non-linear parameters of interest, namely the dimensionless friction, F, the Grüneisen parameter, γ, and the shear deformation potential, β. The determination of these values is complicated; there is no out of the box technique which can be blindly applied. Additionally it is computationally expensive. The fits including all three fitting parameters took two days to run on 7 processors. Accordingly, this Appendix will endeavor to give enough detail to easily reproduce the fitting algorithm while providing tricks to maximize efficiency in Wolfram Mathematica 8.0 along the way.

Since the functional dependencies of the fitted parameters are very complicated and non-linear, there is no applicable out of the box fitting algorithm. Instead, a brute force algorithm is used. A range of fitting parameters sets, (F, γ, β), are iterated through and for each set the global reduced χ^2,

$$\tilde{\chi}^2 = \frac{1}{D.O.F.} \sum_i \left(\frac{model_i - data_i}{\sigma_i} \right)^2 ,$$

is calculated as a goodness of fit metric. Here, $D.O.F.$ is the degrees of freedom in

the fit equal to the number of fit data points less the number of parameters fit to the data, $model_i - data_i$ is the difference between the modeled and measured values at point i, and σ_i is the measured uncertainty in $data_i$. Most importantly, i includes the data points from *all* of the spectra in the line scan. Instead of fitting each spectra individually, the full line scan is taken into account for a global determination of the fitting parameters. The best fit value is then found by looking for the fitting parameters which yield the smallest $\tilde{\chi}^2$.

The algorithm used to find the best fit is detailed in the flowchart in Figure C.1. Broadly speaking, the algorithm works by looping across a range of fitting parameters and checking how accurately the fitting parameters represent the global line scan spectra. Individual steps are described in the proceeding. Steps with red outlines in the flowchart will be described in the most detail as they are the most difficult.

Load spectra, known parameters

The first step is to load in the measured spectra and the independently determined parameters. The majority of the many free parameters are measured independently. The applied pressure is measured using a digital pressure gauge and recorded as a function of time. Often, the pressure regulator will allow the pressure to decrease by several tenths of a PSI during a measurement. In this case, the average of the pressure over the measurement window is used. The determination of the pressure trapped inside the microchamber as well as the unstrained G band position for the suspended FLG is detailed in Section 4.2.1. The G band width for the suspended graphene is taken from the center of the atmospheric pressure line scan. For supported FLG, the width and position of the unstrained G band is taken from the spectra at the largest radial distance measured during a line scan at either 0.17 MPa or atmospheric
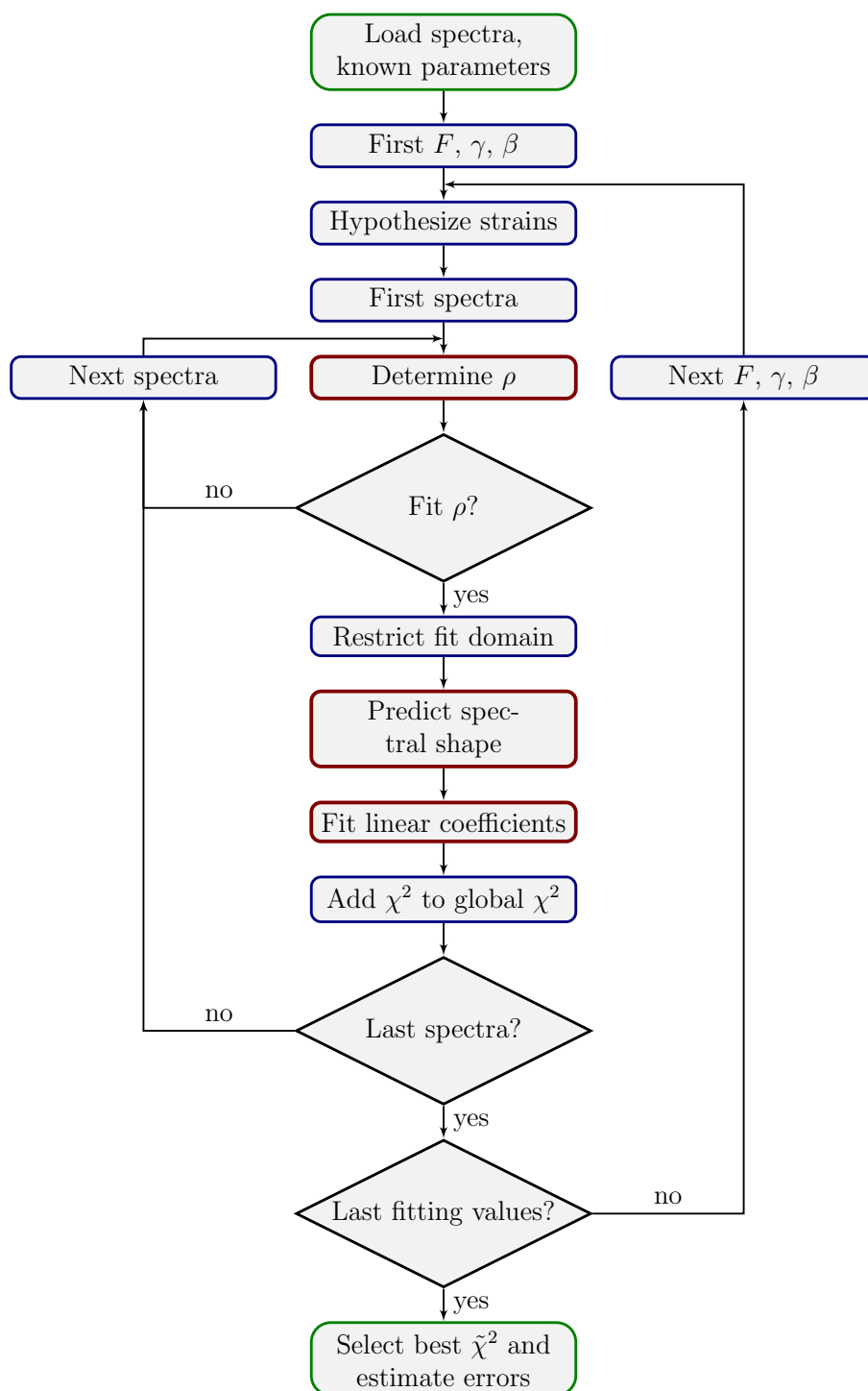
Figure C.1: Flow chart of global fitting algorithm to determine F, γ, β from line scans over pressurized graphene sealed microchambers.

pressure. The number of graphene layers is found using Raman spectroscopy (Ferrari et al., 2006) and optical contrast (Blake et al., 2007; Casiraghi et al., 2007). The measurement of the laser spot size is described in Section 4.1 Microchamber radius is determined from ambient pressure AFM which is analyzed depending on the devices ambient pressure behavior. For those devices that bulge up, the radius is found by fitting an AFM section cut which spans the microchamber center with the lowest order approximation to the Hencky model: A parabola. For those devices which stick to the side walls, the radius is measured manually based on the two dimensional topography. This leaves only the friction, Grüneisen parameter, shear deformation potential, signal intensity, and signal background as unknowns.

First F, γ, β

The outer loop cycles through the range of sampled fitting parameters. A balance must be struck when defining the range of fitting parameters to be tested. Too few fitting parameters increases the chances of missing the global minimum while too many makes the computational load too high. Supplementing this fitting algorithm with a manual fitting technique can build an intuition for the system while also decreasing the chances the global minimum is not found. By guessing individual fitting parameters instead of looping through a range of values, the user can observe how the fitting parameters effect the predicted spectra and $\tilde{\chi}^2$. This intuition gained should assist the user in determining a reasonable range of fitting parameters.

Hypothesize strains

Having selected one set of fitting parameters, the guessed dimensionless friction, F, is used with the known dimensionless loading, q, to generate a hypothetical strain

distribution. This amounts to solving Equations 4.19 for the parameters which determine the shape of the strain distribution. Mathematica's Solve routine can be effectively used for this. When including terms up to tenth order in the strain expansion a solution is found in seconds. The hypothetical strain distribution is defined by the single real solution. The next task is to determine how well the measure spectra agree with this strain distribution.

First spectra

The inner loop cycles through the spectra in the line scan. Although the fitting is global in scope, individual spectra must still be isolated to fit linear coefficients.

Determine ρ

Even though the relative distance the sample is moved between spectra is set experimentally, the absolute position of the individual spectra measured from the center of the microchamber is not necessarily fully determined. This uncertainty could arise due to a slight offset in the beam position relative to the targeted position, from sample drift, or from targeting uncertainty. It can be best overcome using a retroactive determination of the central spectra us single Lorentzian fits to the data. As shown in Figure 4.5 the single Lorentzian fit to the line scan spectra comes to a symmetric minimum. This minimum occurs at point closest to the center of the microchamber where the strains, and thus the down-shifts, are the greatest. Its position can be accurately determined by fitting a similar symmetric function to the single Lorentzian fits such as a Gaussian or a parabola. The dimensionless radius, $\rho = r/R$, of each spectra is then determined by the position of the center of the microchamber, the spacing between spectra, and the radius of the microchamber.

Fit ρ?

Not every spectra in the line scan is included in the fit. For microchambers with radii larger than 1.5 μm, the global $\tilde{\chi}^2$ includes every spectra except for those located less than half the beam waist away from the edge of the microchamber. This is done to avoid the inclusion of the fitting parameters that would need to be added to account the different optical interference conditions for suspended and supported graphene.

When fitting the smaller radius microchambers ($R < 1.5$ μm), the spectra from the suspended graphene are ignored. Figure C.2 shows an example of the resulting best fit. Even though they were not included in the fit, the spectra predicted by the extended Hencky model matches the major feature of the suspended spectra. Spectra from the suspended region ($\rho < 1$) exhibit a high energy shoulder that is not predicted by the extended Hencky model. This feature is observed in each of the three measured graphene sealed microchambers with radius less than 1.5 μm but not for the five larger radius microchambers. This feature is believed to come from airy rings in the focused laser beam. These rings of intensity would contribute signal from lower strain regions giving a distinct higher energy signal. For larger radius microchambers, the laser spot is smaller relative to the microchamber radius and so it samples a more uniform distribution of strains, making an extra contribution from the airy rings unimportant. Complications of fitting these features are avoided by only including the spectra from the supported graphene when fitting.

Restrict fit domain

The numerical integration over the point spread function is the most numerically intensive step in the algorithm and it is linear in the number of frequency points sampled. To hasten this process, many of the measured data points can be eliminated.
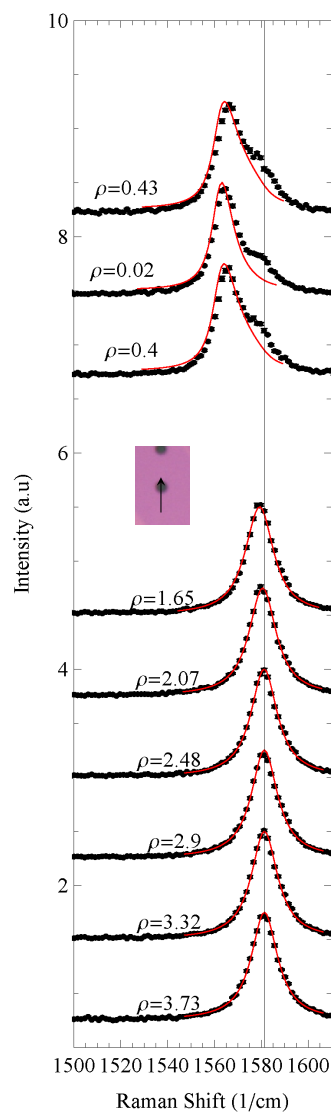
Figure C.2: An example globally fit line scan with radii less than 1.5 microns ($R \sim$ 1.2 μm, bilayer, 0.8 MPa). Spectra taken along the path shown in the inset are arrayed vertically with those spectra within half a beam waist of the microchamber edge omitted. The black vertical line indicates the supported graphene's unstrained G band energy. Plotted in red are global fitting results which include only supported spectra as described in the text.

They are flat background which adds no value to the fit. Since the energy of the features vary by as much as 100 1/cm, a static fitting domain is not ideal. Instead the expendable data points are eliminated using a position dependent fitting domain. The domain boundaries are calculated using the hypothetical energies of the G^- (ω_G^-) and G^+ (ω_G^+) peaks at the position the spectra is taken given the values of γ and β. The fitting domain is taken as $[\omega_G^- - 4\Gamma_{in}, \omega_G^+ + 3\Gamma_{in}]$ where Γ_{in} is the width of the G band for the suspended graphene. The asymmetry of the fitting domain is chosen to better match the fitted features. In this way computation time is decrease without jeopardizing the quality of the fit.

Predict spectral shape

Measured spectra do not represent the signal from a single point. In fact, as shown in Section 4.1 the focused laser excitation has a Gaussian profile with a beam waist of $0.81 \pm .01$ μm. The need to account for the finite excitation spot size is illustrated in Figure C.3 which shows the intensity envelope of the excitation beam overlaid on the strain profile. Even for this large radii microchamber, each spectra represents a continuum of strain states. This section explains how the shape for the current values of the fitting parameters is predicted by integrating over the excitation point spread function. In the next section, this spectral shape will be scaled to best fit the data.

It should be noted that when the suspended graphene is pushed into the microchamber, it is also pushed slightly out of the focal plane. This effect is minimal. The confocal length of a 514 nm laser with a 0.81 μm beam waist is 4 μm, yielding a beam expansion of $< 3\%$ for the < 1 μm graphene deflections encountered in the experiments. This was considered small enough to ignore.

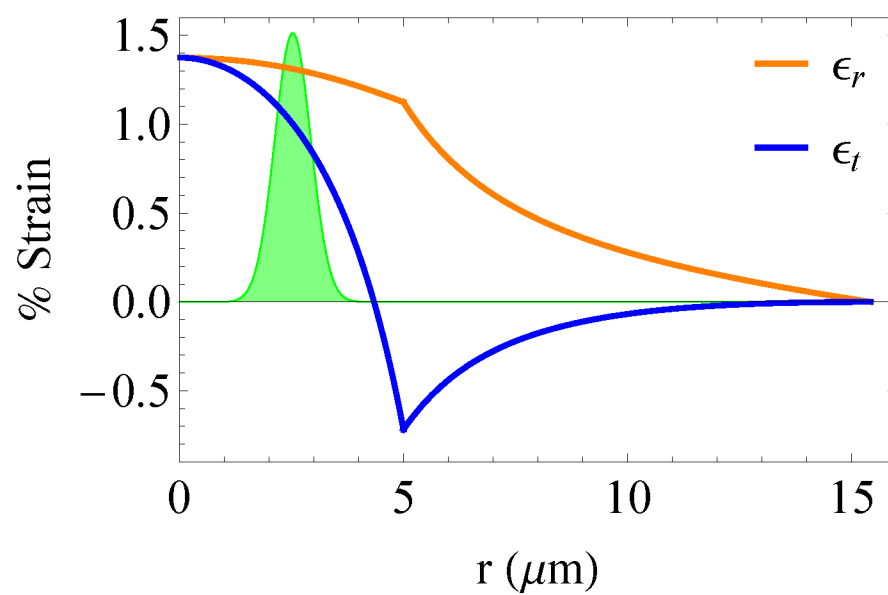The finite spot size is accounted for by integrating over the spectra contributed by

Figure C.3: Laser excitation profile overlaid on the best fit strain distribution for the $\sim 5\ \mu m$ radius monolayer graphene sealed microchamber with 0.80 MPa of applied pressure.

each point weighted by the excitation point spread function. Each point contributes a spectra with two Lorentzian peaks centered at

$$\omega^+(\rho) = \omega_0(\rho) - \omega_0(\rho)\gamma(\epsilon_r(\rho) + \epsilon_t(\rho)) + \frac{1}{2}\beta(\epsilon_r(\rho) - \epsilon_t(\rho))$$

$$\omega^-(\rho) = \omega_0(\rho) - \omega_0(\rho)\gamma(\epsilon_r(\rho) + \epsilon_t(\rho)) - \frac{1}{2}\beta(\epsilon_r(\rho) - \epsilon_t(\rho)) \ .$$

The resulting spatial dependence of the Raman spectra is

$$g(\rho,\omega) = \frac{\left(\frac{1}{2}\Gamma(\rho)\right)^2}{(\omega - \omega^+(\rho))^2 + \left(\frac{1}{2}\Gamma(\rho)\right)^2} + \frac{\left(\frac{1}{2}\Gamma(\rho)\right)^2}{(\omega - \omega^-(\rho))^2 + \left(\frac{1}{2}\Gamma(\rho)\right)^2} \ ,$$

A position dependence is given to $\omega_0(\rho)$ and $\Gamma(\rho)$ because the suspended graphene is in general less doped than supported graphene. This is taken into account by treating $\omega_0(\rho)$ and $\Gamma(\rho)$ as step functions which change value at the edge of the microchamber.

To match the circular symmetry of the strain distribution, the excitation point spread function should be expressed as an envelope function in radial coordinates with the origin at the center of the microchamber. Accounting for the point spread function, the shape of the measured spectra is given by

$$f(\omega,\rho_\star) = \int\int \mathrm{dx} \ \mathrm{dy} \ e^{-\frac{(x-x_\star)^2+y^2}{2\sigma^2}} \ g(\sqrt{x^2+y^2}/R,\omega)$$

$$= e^{-\frac{r_\star^2}{2\sigma^2}} \int \mathrm{dr} \ r \ e^{-\frac{r^2}{2\sigma^2}} g(r/R,\omega) \int \mathrm{d\theta} \ e^{\frac{rr_\star\cos(\theta)}{\sigma^2}}$$

$$= 2\pi R^2 \ e^{-\rho_\star^2/2\bar{\sigma}^2} \int \mathrm{d\rho} \ g(\rho,\omega) \ \rho \ e^{-\rho^2/2\bar{\sigma}^2} \ \mathrm{I}_0\left(\frac{\rho\rho_\star}{\bar{\sigma}^2}\right)$$

$$\propto \frac{1}{Norm(\rho_\star)} \int \mathrm{d\rho} \ g(\rho,\omega) \ P(\rho,\rho_\star) \ ,$$

where $x_\star$, $r_\star$, and $\rho_\star$ are the position of the laser in Cartesian, cylindrical, and normalized cylindrical coordinates respectively, σ, is equal to half the beam waist, $\bar{\sigma} = \sigma/R$,

$I_0(x)$ is the modified Bessel function of the first kind, and $P(\rho, \rho_\star) = \rho \, e^{-\rho^2/2\bar{\sigma}^2} \, I_0 \left(\frac{\rho\rho_\star}{\bar{\sigma}^2} \right)$ is the envelope function. A normalization constant, $Norm(\rho_\star)$, which is close to the maximum value of the envelope function was included to keep the widely varying values of the envelope function in a computationally reasonable range. The maximum of the envelope function is well approximated as

$$
Norm(\rho_\star) = \begin{cases} .03 & , \ \rho_\star < .1 \\ P(\rho_\star, \rho_\star) & , \ \rho_\star \geq .1 \ , \end{cases}
$$

and is independent of ω. Thus, it should be calculated once per spectra as an over head step.

The integral in $f(\omega, \rho_\star)$ can not be solved analytically. The strains fields alone are too complex, let alone the additional complexity added by the Lorentzian functions and the envelope function. Instead, $f(\omega, \rho_\star)$ must be integrated numerically at each frequency. Since the form of the strain distribution are different in the domains $[0, 1]$, $[1, \rho_0]$, $[\rho_0, \mathrm{inf}]$ it might seem simplest to treat $f(\omega, \rho_\star)$ as three distinct numeric integrals. Alternatively, one numerical integral could be used with piecewise functions. The fastest technique in Wolfram Mathematica 8.0, however, is to minimize the number of numeric integrals without introducing piecewise functions. The integral over the second domain can be scaled into the first domain using the change of variables

$\rho' = \frac{\rho - 1}{\rho_0 - 1}$ giving

$$f(\omega, \rho_\star) = \int_0^1 \mathrm{d}\rho \left\{ \underbrace{g(\rho, \omega)P(\rho, \rho_\star)}_{\text{inside}} \right.$$

$$+ \underbrace{(\rho_0 - 1)g(\rho(\rho_0 - 1) + 1, \omega)P(\rho(\rho_0 - 1) + 1, \rho_\star)}_{\text{outside}} \left. \right\}$$

$$+ g(\infty, \omega) \underbrace{\int_{\rho_0}^\infty \mathrm{d}\rho P(\rho, \rho_\star)}_{int3(\rho_\star)} .$$

Similar to $Norm(\rho_\star)$, $int3(\rho_\star)$ is independent of ω and thus needs to be calculated only once for each $\rho_\star$ as an overhead step. In this way three numeric integrals have been combined into two numeric integrals with one of which only calculated once per $\rho_\star$.

Finally, it should be noted that since the numeric integration is the slowest step it should only be calculated once for each ω in the restrict data domain. Everything should then reference back to these values.

Fit linear coefficients

Having established the predicted shape of the spectra given the current values of the fitting parameters, the modeled spectra needs only to be scaled to match the measured spectra for a comparison to be made. The scaled modeled spectra is

$$model(\omega, \rho_0) = Af(\omega, \rho_\star) + b ,$$

where A and b are linear coefficients which correspond to the signal amplitude and the background levels respectively. These will be independently fit to the measured

spectra on a spectra by spectra basis.

Fitting these linear coefficients is much simpler than the non-linear fitting parameters. Press *et al.* provide a simple matrix method to determine these coefficients (Press et al., 2007). It is based on the direct minimization of χ^2 by requiring that $\frac{\partial \chi^2}{\partial A} = \frac{\partial \chi^2}{\partial b} = 0$. This yields the system of equations

$$
\begin{pmatrix} \sum_j \frac{data_j f(\omega_j, \rho_\star)}{\sigma_j^2} \\ \sum_j \frac{data_j}{\sigma_j^2} \end{pmatrix} = \begin{pmatrix} \sum_j \frac{f(\omega_j, \rho_\star)^2}{\sigma_j^2} & \sum_j \frac{f(\omega_j, \rho_\star)}{\sigma_j^2} \\ \sum_j \frac{f(\omega_j, \rho_\star)}{\sigma_j^2} & \sum_j \frac{1}{\sigma_j^2} \end{pmatrix} \begin{pmatrix} A \\ b \end{pmatrix} ,
$$

where j runs over the data points in the restricted domain of the current spectra. Thus, fitting for the linear coefficients requires only the inversion of a 2 by 2 matrix.

More linear coefficients could be included to account for effects like the different signal intensity for suspended and supported graphene or to allow for different signal intensities from the G^+ and G^- peaks. However, there is no way to restrict the above procedure to give only positive values for the linear coefficients. Extra coefficients will often lead to non physical, negative coefficients that make the interpretation of the fit metrics more complicated. Two linear coefficients are enough to capture the complexity of the system while maintaining the simplicity of the fit.

Add χ^2 to global χ^2

Having calculated the best possible fit of the hypothetical spectra to the measured data, the goodness of fit can be quantified using the χ^2 metric. The calculated, not yet reduced by dividing the degrees of freedom, χ^2 of this spectra should be added to the global χ^2 which includes the χ^2 of each spectra in the data set for the current fitting parameters. In the off chance that the current fitting parameters are the best fit, it is also useful to save the linear coefficients so that they will not need to be

redetermined later.

Select best $\tilde{\chi}^2$ and estimate errors

After each spectra in the line scan is considered, the global χ^2 is reduced by dividing by the degrees of freedom. The number of degrees of freedom are equal to the number of fit data points, which was reduced when the fitting domain was restricted, minus the number of fitted parameters, including the 3 fitting parameters and the two linear coefficients per spectra. This global $\tilde{\chi}^2$ should be saved so that the $\tilde{\chi}^2$ space can be visualized and the minimum found. It is useful to keep track of the best $\tilde{\chi}^2$ and the corresponding linear coefficients so that the linear coefficients won't need to be refit afterward.

The sampled fitting parameter with the lowest $\tilde{\chi}^2$ best represent the data. However, these values are not necessarily the best fit. To ensure that these fitting parameters represent a global minimum and not just a local minimum the $\tilde{\chi}^2$ space should be visualized. If only the dimensionless friction was varied, this is done by plotting $\tilde{\chi}^2$ as a function of F. A global minimum indicates a best fit. If all three fitting parameters were varied the four dimensional $\tilde{\chi}^2$ space is more difficult to visualize. One useful way to reduce the dimensionality is to choose the unplotted fitting parameters such that they minimized the $\tilde{\chi}^2$ for the plotted value. In this way, the plotted values represent the best case scenario. Figure C.4 shows a reduced dimensionality $\tilde{\chi}^2$ plot for a three fitting parameter fit. An obvious minimum in the $\tilde{\chi}^2$ near f=0.14 MPa is visible.

The departure from the minimum of $\tilde{\chi}^2$ can be used to estimate uncertainties in the fitting parameters. A very steep $\tilde{\chi}^2$ space corresponds to tightly defined fitting parameters. When viewing the $\tilde{\chi}^2$ space in reduced dimensionality, one needs to be
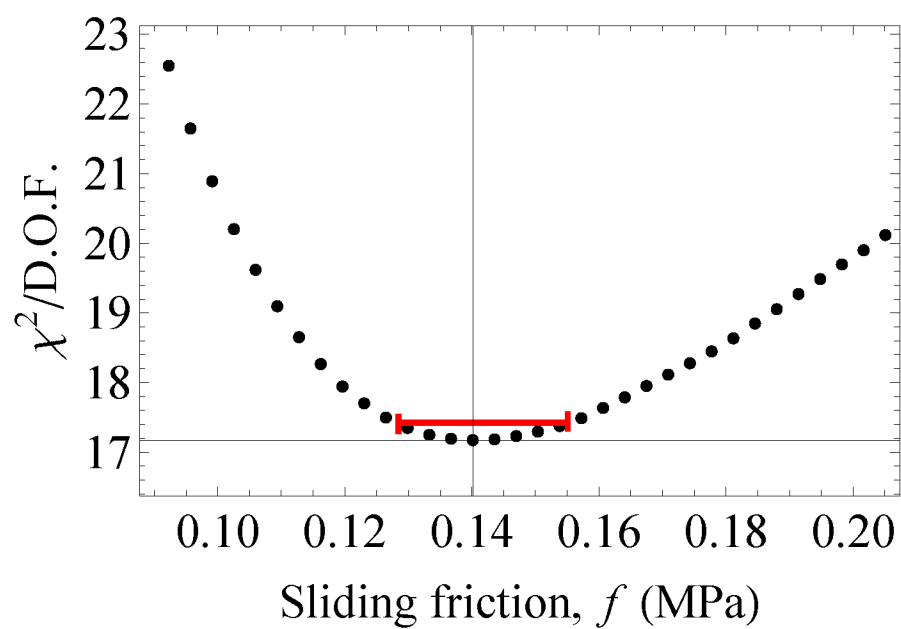
Figure C.4: $\tilde{\chi}^2$ as a function of the dimensionless friction for the $\sim 5~\mu m$ radius monolayer graphene sealed microchamber with 0.80 MPa of applied pressure. For each value of F, the γ and β pair which minimized $\tilde{\chi}^2$ was chosen. The black cross hair sits at the best fit and the red, side ways error bar indicates the uncertainty in the fit based on an increase in $\tilde{\chi}^2$ of 0.25.

careful that the dimensionality is reduced properly. Taking an arbitrary slice in $\tilde{\chi}^2$ space can yield artificially low uncertainties. Errors in the fitted parameters found by using the increase in χ^2 away from its minimum value (Press et al., 2007) are better than one part in one hundred, much smaller than we can claim to have achieved in our experiment. This discrepancy is due to an underestimation of our uncertainties which include only photon counting and ignore effects due to inhomogeneous doping, sample drift, and laser assisted deposition of dirt on the FLG. To better illustrate the relative uncertainties amongst different fitted friction values we use a 0.25 increase of χ^2 per degree of freedom above the best fit value to define confidence intervals. Using this method, the uncertainty in the fitted value in Figure C.4 is indicated by the red horizontal error bar.

Appendix D

Heat transport model

This Appendix gives details on and describes the use of the heat transfer model in Chapter 5. In the first section the heat transfer model first proposed by Cai *et al* is summarized. It predicts the temperature profile which develops in a circular graphene sealed microchamber due to central laser heating (Cai et al., 2010). In the second section an approximation relating the thermal properties to the measured peak shifts is presented. This allows for a fast interpretation of the measured spectra.

D.1   Model derivation

The heat transfer model predicts the temperature profile based on the thermal conductivity of the suspended graphene, κ_{SS}, the thermal conductivity of the supported graphene, κ_{SP}, the interface thermal conductivity between the supported graphene and the underlying SiO$_2$, g_S, the interface thermal conductivity to the gas, g_g, and the laser power which reaches the graphene, P. The solution is determined by solving the steady state heat equation,

$$\vec{\nabla} \cdot \left(\kappa(r) \, \vec{\nabla} T(r) \right) + \dot{Q} = 0 \ ,$$

where $T(r)$ is the temperature distribution, κ is the thermal conductivity, and $\dot{Q}$ is the generated heat flux per unit time. This model is simplified by the concentric circular symmetry of the laser heating source and the circular microchamber. The general solution is found by matching the solution for inside, $r < R$, and outside, $r > R$, the edge of the microchamber with boundary conditions at $r = R$.

Isolating the graphene, the generated heat flux includes the laser heating, the energy lost to the gas, and the energy lost to the supporting substrate. The laser heating is described by

$$\dot{Q}_L = \frac{\alpha P}{t} \frac{1}{2\pi\sigma^2} e^{-r^2/\sigma^2} \, , \tag{D.1}$$

where $\dot{Q}_L$ is the energy from the incident laser, α is the absorption by the graphene, t is the thickness of the graphene, and σ is half the beam waist measured to be 0.66 μm. The beam waist was measured the same way as in is Section 4.1. It is smaller because the test slip adjustment collar was readjusted. The energy lost to the substrate and gas is modeled using Newton's law of cooling

$$\dot{Q}_S = -g_S \frac{1}{t} \left(T(r) - T_0 \right)$$
$$\dot{Q}_g = -g_g \frac{1}{t} \left(T(r) - T_0 \right) \, ,$$

where $\dot{Q}_S$ and $\dot{Q}_g$ are the energy lost to the substrate and to the gas respectively and T_0 is ambient temperature. In the case of the suspended graphene, heat can be lost to both the gas above and below the graphene. This will be differentiated using $g_g^\uparrow$ and $g_g^\downarrow$.

When applying Newton's law of cooling for the heat conduction to the silicon dioxide, we assume the temperature of the SiO_2 is fixed at T_0. To test this assumption

the thermal oxide is treated as a cylindrical shell connected on one side to a heat sync and heated on the other side by a 0.03 mW source. This heating matches a 1.5 mW laser excitation with graphene's 2.3 % absorption. The width of the shell is taken as 200 nm to match the width of the supported graphene that is expected to have elevated temperatures. With an inner radius of 5 μm, a thickness of 300 nm, and a thermal conductivity of 1 W/m-K (Resnick et al., 2002) the temperature is expected to rise by 1.5 K on the top surface of the thermal oxide. This should be treated as an upper bound; the transport in the silicon dioxide would flare outward resulting in a larger conduction cross section. This validates the assumption that the thermal oxide is not significantly heated in our measurements.

The other term in Equation D.1, the thermal conductivity, is assumed to be piecewise uniform

$$\kappa(\vec{r}) = \begin{cases} \kappa_{SS} & , r < R \\ \kappa_{SP} & , r \geq R \end{cases} .$$

This eliminates the spatial dependence of κ in the two regions and simplifies the heat equation in Equation D.1 but still allows for the disparate suspended and supported thermal conductivities observed in the literature. While needed to simplify the problem, this simple form for the thermal conductivity may not be entirely accurate. A strain dependent thermal conductivity would inherit the spatial dependence of the strain field. Since the measurement described here can not provide spatial information to inform a more detailed model, we will assume a uniform κ_{SS} and refer to it as the effective thermal conductivity of the suspended graphene. It acts as a metric which represents the departure of the system from the unstrained case.

Including the generated heat fluxes and the piecewise thermal conductivity in the heat equation, Equation D.1, results in two differential equations that in the

dimensionless variables

$$\theta = \frac{1}{T_a}(T(r) - T_a)$$

$$\rho = \frac{r}{\sqrt{2}\sigma}$$

becomes

$$
\begin{cases}
\nabla^2\theta + \beta e^{-\rho^2} - \gamma\theta = 0 & , \text{ for } \rho < \frac{R}{\sqrt{2}\sigma} \\
\nabla^2\theta - \Gamma\theta = 0 & , \text{ for } \rho \geq \frac{R}{\sqrt{2}\sigma}
\end{cases}
, \tag{D.2}
$$

where

$$\beta = \frac{1}{\pi T_0}\frac{\alpha P}{t\kappa_{SS}}$$

$$\gamma = 2\sigma^2\frac{g_g^\uparrow + g_g^\downarrow}{t\kappa_{SS}}$$

$$\Gamma = 2\sigma^2\frac{g_g^\uparrow + g_S}{t\kappa_{SP}} \ .$$

Together with the boundary conditions

$$\theta(\infty) = 0 \tag{D.3}$$

$$|\theta(0)| < \infty \tag{D.4}$$

$$\theta\left(\frac{R}{\sqrt{2}\sigma}\right)^- = \theta\left(\frac{R}{\sqrt{2}\sigma}\right)^+ \tag{D.5}$$

$$-\kappa_{SS}\left.\frac{d}{d\rho}\theta^-\right)_{r=\frac{R}{\sqrt{2}\sigma}} = -\kappa_{SP}\left.\frac{d}{d\rho}\theta^+\right)_{r=\frac{R}{\sqrt{2}\sigma}} \tag{D.6}$$

this fully defines the problem. The boundary conditions are written by assuming that the temperature profiles are finite, decay asymptotically to ambient temperature, are continuous at the edge of the microchamber, and have continuous heat flux at the edge of the microchamber, respectively. The heat flux, $\vec{\phi}$, is found using Fourier's law

of heat conduction, $\vec{\phi} = -\kappa \vec{\nabla} T(\vec{r})$.

The heat equation for $r \geq R$ has a relatively simple solution. It can be recast in the form of the modified Bessel's equation and after applying the boundary condition in Equation D.3 it has the solution,

$$\theta(\rho) = c_2 K_0(\sqrt{\gamma}\rho), \text{ for } \rho \geq \frac{R}{\sqrt{2}\sigma} \ , \tag{D.7}$$

where c_2 is a integration constant and $K_0(\sqrt{\gamma}\rho)$ is the modified Bessel function of the second kind.

The solution for the suspended graphene is complicated by the incident laser. Using the substitution $x = \sqrt{\gamma}\rho$ the heat equation is cast into a *inhomogeneous* modified Bessel function,

$$\rho^2 \frac{d^2\theta}{dx^2} + x \frac{d\theta}{dx} - x^2\theta = -\frac{\beta}{\gamma} x^2 \ e^{-x^2/\gamma} \ .$$

This differential equation has the general solution

$$\theta(\rho) = c_3 I_0(\sqrt{\gamma}\rho) + c_4 K_0(\sqrt{\gamma}\rho) + \theta_P(\sqrt{\gamma}\rho), \text{ for } \rho \geq \frac{R}{\sqrt{2}\sigma} \ ,$$

where $I_0(\sqrt{\gamma}\rho)$ is the modified Bessel function of the first kind and $\theta_P(\rho)$ is the particular solution to the inhomogeneous differential equation. Using the variation of parameters technique, the particular solution can be written as an integral function,

$$\theta_P(x) = \frac{\beta}{\gamma} \left\{ I_0(x) \int_0^x \frac{K_0(x') \ e^{-x'^2/\gamma}}{-I_0(x')K_1(x') - K_0(x')I_1(x')} dx' \right.$$
$$\left. -K_0(x) \int_0^x \frac{I_0(x') \ e^{-x'^2/\gamma}}{-I_0(x')K_1(x') - K_0(x')I_1(x')} dx' \right\} \ .$$

The boundary condition in Equation D.4 requires that $c_4 = 0$ leaving two integration constants: c_2 and c_3.

These two remaining integration constants are fully determined by the boundary conditions in Equations D.5 and D.6. This results in two equations with two unknowns,

$$
\begin{aligned}
c_2 K_0(\sqrt{\Gamma/2}R/\sigma) =& c_3 I_0(\sqrt{\gamma/2}R/\sigma) + \theta_P(\sqrt{\Gamma/2}R/\sigma) \\
c_2 \kappa_{SP}\sqrt{\Gamma}K_1(\sqrt{\Gamma/2}R/\sigma) =& - \kappa_{SS}\sqrt{\gamma}\left\{ c_3 I_1(\sqrt{\gamma/2}) \right. \\
&+ I_1(x)\frac{\beta}{\gamma}\int_0^x \frac{K_0(x')\ e^{-x'^2/\gamma}}{-I_0(x')K_1(x') - K_0(x')I_1(x')}dx' \\
&\left. -K_1(x)\frac{\beta}{\gamma}\int_0^x \frac{I_0(x')\ e^{-x'^2/\gamma}}{-I_0(x')K_1(x') - K_0(x')I_1(x')}dx' \right\}_{x=\sqrt{\frac{\gamma}{2}}\frac{R}{\sigma}}.
\end{aligned}
$$

$$\text{(D.8)}$$

This fully defines the temperature profile as a function of the thermal parameters κ_{SS}, κ_{SP}, g_g, and g_S as well as the power of the excitation laser at the graphene, the radius of the microchamber, and the beam waist. The temperature at the center of the microchamber, θ_0, is given by c_3. The derived temperature profile is scaled linearly by the power P.

D.2 Relating model to measurements

To extract thermal properties from the Raman measurements, the heat transfer model must be related to the measured spectra. This is complicated by the finite spot size of the measurement as shown in Figure 5.2. This section will derive an approximate relationship between the measurement and the heat transfer model which allows for a simple determination of the thermal properties.

The measure temperature rise, θ_M represents a weighted average of the tempera-

ture profile,

$$\theta_M = \frac{\int_0^\infty \theta(\rho)e^{-\rho^2}\rho \, d\rho}{\int_0^\infty e^{-\rho^2}\rho \, d\rho} \ . \tag{D.9}$$

Using the full heat transfer model derived in the previous section makes the determination of this integral difficult. Instead, an approximate solution for the temperature profile of the suspended graphene in the vicinity of the laser excitation is used. Since the amount of energy lost to the gas across the laser spot is small compared to the heat transferred in plane, the heat transfer to the gas can be ignored when calculating the temperature profile in the vicinity of the laser beam. This can be shown by starting with Equation D.2 and using separation of variables twice,

$$d\left[\rho\frac{d\theta}{d\rho}\right] = -\beta\rho e^{-\rho^2} \, d\rho + \gamma\rho\theta \, d\rho$$

$$\int_{\theta_0}^{\theta(\rho)} d\theta = -\frac{\beta}{2}\int_0^\rho \frac{e^{-\rho'^2}-1}{\rho'}d\rho' + \gamma\int_0^\rho \rho'\left[\int_0^{\rho'}\rho''\theta(\rho'') \, d\rho''\right] d\rho'$$

$$\theta(\rho) = \theta_0 - \frac{\beta}{2}\int_0^\rho \frac{e^{-\rho'^2}-1}{\rho'}d\rho' + \frac{\gamma}{8}\theta_0 + \gamma\int_0^\rho \rho'\left[\int_0^{\rho'}\rho''\Delta\theta(\rho'') \, d\rho''\right] d\rho' \ ,$$

where θ_0 is the temperature at the center of the microchamber and $\Delta\theta(\rho) = \theta(\rho) - \theta_0$. The first two terms have the form of the temperature profile calculated if thermal transport to the gas is ignored(Faugeras et al., 2010), the second term is the first order correction for the gas, and the last term is the higher order correction that will be neglected. The temperature at the center of the microchamber is determined by the full heat transfer model described in the previous section.

This approximation temperature profile has a simpler radial dependence which can be averaged over in closed form. The integral in Equation D.9 now has the simple solution

$$\theta_M \approx \theta_0(1+\frac{\gamma}{4}) - \frac{ln(2)}{4}\beta \ . \tag{D.10}$$

By using this relationship in conjunction with $\theta_0 = c_3$ in Equation D.8 the measured temperature is related to the thermal parameters.

Appendix E

Hopping energies in the Kekulé geometry

In this appendix the hopping energies between nearest neighbors in the Kekulé distorted lattice are calculated. This calculation closely follows the work of Chamon *et al.* (Chamon et al., 2013) in which they cleverly find an expression for the nearest neighbor bond length by working in complex coordinates where vectors are expressed as $a = \vec{a} \cdot \hat{x} + i\vec{a} \cdot \hat{y}$. They then use the change in bond length to determine the change in hopping energy using Equation 3.4

The displacements generated by the iTO phonon at the $\boldsymbol{K}$ point (Equation 6.1) can be rewritten in complex notation as

$$\vec{u}_A(\vec{r}_A, t) = \begin{pmatrix} Re[c\ e^{i\vec{r}_A \cdot \boldsymbol{K}} e^{-i\omega t}] \\ Im[c\ e^{i\vec{r}_A \cdot \boldsymbol{K}} e^{-i\omega t}] \end{pmatrix} \rightarrow u_A(\vec{r}_A, t) = ce^{i\vec{r}_A \cdot \boldsymbol{K}} e^{-i\omega t}$$

$$\vec{u}_B(\vec{r}_B, t) = \begin{pmatrix} Re[c\ e^{i\vec{r}_B \cdot \boldsymbol{K}} e^{-i\omega t}] \\ -Im[c\ e^{i\vec{r}_B \cdot \boldsymbol{K}} e^{-i\omega t}] \end{pmatrix} \rightarrow u_B(\vec{r}_B, t) = c^* e^{-i\vec{r}_B \cdot \boldsymbol{K}} e^{i\omega t} \ .$$

The nearest neighbor vector in the Kekulé lattice connecting an A sub-lattice atom originally at position $\vec{r}$ and a B sub-lattice atom originally at position $\vec{r} + \vec{\delta_j}$ is

$\vec{\delta}'_j(\vec{r}) = \vec{\delta}_j + \vec{u}_B(\vec{r} + \vec{\delta}_j) - \vec{u}_A(\vec{r})$. The magnitude of this vector is approximated as

$$|\vec{\delta}'_j(\vec{r})| = \sqrt{\delta'_j(\vec{r})\ \delta'_j(\vec{r})^*}$$

$$\approx \sqrt{a^2 + \left\{\delta^*_j\left(u_B(\vec{r}+\vec{\delta}_j) - u_A(\vec{r})\right) + \text{c.c.}\right\}}$$

$$\approx a + \frac{1}{2}\frac{1}{a}\left\{\delta^*_j\left(u_B(\vec{r}+\vec{\delta}_j) - u_A(\vec{r})\right) + \text{c.c.}\right\}\ .$$

This can be simplified by using $\vec{\delta}_j = -iaz_j$ where $z_j = e^{i\boldsymbol{K}\cdot\vec{\delta}_j}$ and $z_j^2 = z_j^*$. The relative extension of the nearest neighbor vector is then

$$\frac{|\vec{\delta}'_j(\vec{r})| - a}{a} = \frac{1}{2}\frac{1}{a^2}(iaz_j^*)\left(c^*e^{-i\vec{r}\cdot\boldsymbol{K}}z_j^*e^{i\omega t} - c\ e^{i\vec{r}\cdot\boldsymbol{K}}e^{-i\omega t}\right)$$

$$+ \frac{1}{2}\frac{1}{a^2}(-iaz_j)\left(c\ e^{i\vec{r}\cdot\boldsymbol{K}}z_je^{-i\omega t} - c^*e^{-i\vec{r}\cdot\boldsymbol{K}}e^{i\omega t}\right)$$

$$= i\frac{1}{2a}\left\{(z_j + (z_j^*)^2)c^*e^{-i\vec{r}\cdot\boldsymbol{K}}e^{i\omega t} - (z_j^* + z_j^2)c\ e^{i\vec{r}\cdot\boldsymbol{K}}e^{-i\omega t}\right\}$$

$$= -i\frac{c}{a}z_j^*e^{i\vec{r}\cdot\boldsymbol{K}}e^{-i\omega t} + \text{c.c.}\ .$$

The use of the complex relationship between the δ_j and the z_j was paramount in deriving such a simple relationship.

The term $e^{i\vec{r}\cdot\boldsymbol{K}}$ can be rewritten to have the spatial frequency which connects the inequivalent $\boldsymbol{K}$ points, $\boldsymbol{G} = \boldsymbol{K} - \boldsymbol{K}'$. This can be shown by taking advantage of the fact that $\vec{r}$ is a lattice vector of the old lattice and that

$$\boldsymbol{K} - (\vec{b}_+ - \vec{b}_-) = \boldsymbol{K} - 3\boldsymbol{K} = -2\boldsymbol{K} = -(\boldsymbol{K} - \boldsymbol{K}') = -\boldsymbol{G}\ .$$

Thus, $e^{i\vec{r}\cdot\boldsymbol{K}} = e^{i\vec{r}\cdot(\boldsymbol{K}-\vec{b}_+-\vec{b}_-)} = e^{-i\vec{r}\cdot\boldsymbol{G}}$. In addition to making it clear that the Kekulé mode couples the $\boldsymbol{K}$ points, this also allows for the simplification of $\vec{r}$. The spatial frequency $\boldsymbol{G}$ is a reciprocal lattice vector of the Kekulé lattice equal to $\vec{B}_+ - \vec{B}_-$.

Thus, when specifying $\vec{r} = \vec{R}_l + \vec{r}_m$ there is no need to include $\vec{R}_l$. Instead we only specify $\vec{r}_m$, the position in the Kekulé unit cell of the A sub-lattice atom involved in the hopping.

The change in hopping energy resulting from the change in bond length can then be found using Equation 3.4. The resulting Kekulé altered hopping energies are given by

$$\delta t_{m,j} = \frac{1}{3}\Delta(t)e^{i\boldsymbol{K}\cdot\vec{\delta}_j}e^{i\boldsymbol{G}\cdot\vec{r}_m} + \text{c.c.}$$
$$\text{with } \Delta(t) = -i3\beta t_0\frac{c^*}{a}e^{i\omega t} \ .$$

The interesting effects of these modulated hoppings are discussed in detail in Chapter 6.

Appendix F

Electrical transport experimental design

In situ, four probe, gate dependent electrical transport measurements can be used to measure the phonon induced electrical band gap discussed in Chapter 6. The fingerprint of the phonon induced band gap is transport phenomena which are corrolated with the creation of the Kekulé phonon. In this Appendix gated electrical transport is considered, the expected changes in the electrical transport of gapped graphene is discussed, and finally the measurement of gated electrical transport is described in detail.

F.1 Gate dependent transport

The resistance, R, of a graphene device is related to the two dimensional resistivity, ρ, and the two dimensional conductivity, σ, through

$$\rho = \frac{1}{\sigma} = R\frac{w}{L} \ ,$$

where w is the width and L is the length of the measured graphene strip. To differentiate resistance and resistivity, the units of resistivity are written as $\Omega/\square$. Gate dependent resistance measurements provide information about a graphene device.

Graphene's two dimensional nature makes it simple to continuously modify the
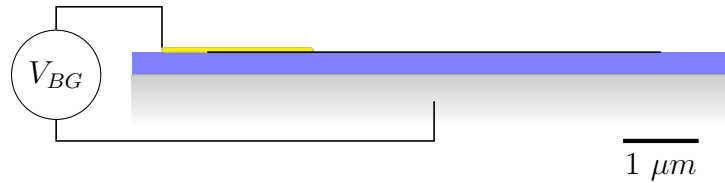
Figure F.1: Side view of a back gated graphene device. The contacted graphene (black line) is on top of 285 nm of thermal oxide (blue) grown on heavily doped silicon (gray). A voltage difference of V_{BG} is placed between the silicon and the graphene to drive charges into the graphene.

Fermi energy using a back gate. Rather than varying the concentration of a dopant as must be done for most three dimensional systems, graphene's Fermi energy can be capacitively tuned with a back gate, as shown schematically in Figure F.1. Together, the silicon back gate and the graphene form a parallel plate capacitor with a plate separation of 285 nm and the dielectric constant of thermal dioxide. Changing the back gate voltage, V_{BG}, adds or removes a charge of $n = CV_{BG}/e$ to the graphene where C is the capacitance and e is the charge of the electron. When V_{BG} is set such that the Fermi energy sits at the charge neutrality point there are the fewest number of charge carriers and thus the highest resistance. This situation doesn't always correspond to $V_{BG} = 0$; every device has a finite number of dopants which shift the Dirac point from zero volts. Tuning the back gate voltage away from the Dirac point adds additional charges and lowers the resistance.

Near the Dirac point in gapless graphene the conductivity is symmetric and nearly linear allowing a field effect mobility, $\frac{d\sigma}{d(ne)}$, to be defined. Even though there are no charge carriers at the Dirac point there is always a residual conductivity, σ_0 (Das Sarma et al., 2011). Further from the Dirac point the conductivity is sub-linear

and is best fit by

$$\frac{1}{\sigma} = \frac{1}{ne\sigma_C + \sigma_0} + \rho_S \, ,$$

where μ_C is the mobility due to long-range Coulomb scattering and ρ_S is from short range scattering (Dean et al., 2010; Das Sarma et al., 2011; Rémi, 2014). Higher quality devices have higher mobilities and Dirac points closer to $V_{BG} = 0$.

For gapless graphene, the Fermi energy can be determined from V_{BG} by matching the integrated density of states (Equation 2.8) to n. Some useful relationships for graphene on 285 nm of thermal oxide are

$$n(cm^{-2}) \sim 7 \times 10^{10} V_{BG}(Volts)$$

$$\mu(meV) \sim 30\sqrt{V_{BG}(Volts)}$$

$$\mu(meV) \sim 1 \times 10^{-7}\sqrt{n(cm^{-2})} \, ,$$

where μ is the Fermi energy.

F.2   Electrical transport fingerprints of the phonon induced band gap

The opening of the band gap should have two fingerprints in electrical transport. First, the resistance at the charge neutrality point should increase. If the capability were available, measuring the temperature dependence of this resistance would give a direct measurement of the size of the band gap. Second, because of the energy required to excite an electron across the band gap, the gate dependent conductivity should exhibit a low conductivity plateau centered on the charge neutrality point. The width of this plateau in volts should correspond to the band gap in electron volts plus any many body effects. The corrolation of these fingerprints with the excitation of the Kekulé phonon would be proof of the phonon induced band gap.

F.3 Measurement of the gate dependent electrical transport

When performing these measurements the goals are to achieve sufficient signal to noise while protecting the nanomaterial from damage. In this Appendix the devices used to measure the transport, the precautions employed to protect the graphene, and the methods of shielding the electronics are described. Because of its importance and because it is so easily forgotten, it should be immediately mentioned that a grounding strap should always be worn when measuring graphene's electrical properties.

A circuit diagram detailing the electronic devices is shown in Figure F.2. A Standford Research SR850 digital lock-in is used to measure the low frequency AC resistance of the graphene device in the four probe, Kelvin sensing geometry. The variable back gate voltage is supplied by a Keithley 2400 source meter (K2400). The breakout box is a custom built passive electronics box that serves several functions. It has two double pull switches, S_1 and S_2, used to ground and protect the sample. It also holds the current limiting $10M\Omega$ resistor. Finally, it breaks the six core, shielded, sample connection wire into six individual BNC terminals. Using short BNC jumpers these terminals are connected to the second row of BNC terminals allowing for a flexible connection between the sample and the source voltage, S, the drain voltage, D, the voltage measurement probes, V_1 and V_2, and the back gate voltage, V_{BG}. All grounds in the system are connected to the SR850 ground. These electronic devices will be described in some detail below.

The low frequency lock-in technique improves on the signal to noise of a DC measurement. However, out of necessity the AC technique is slightly different than the traditional four probe DC resistance measurement. This is because there is no such thing as a constant current AC sources which can be used to pump a contact resistant independent current from source to drain. Instead, the effect of the contact
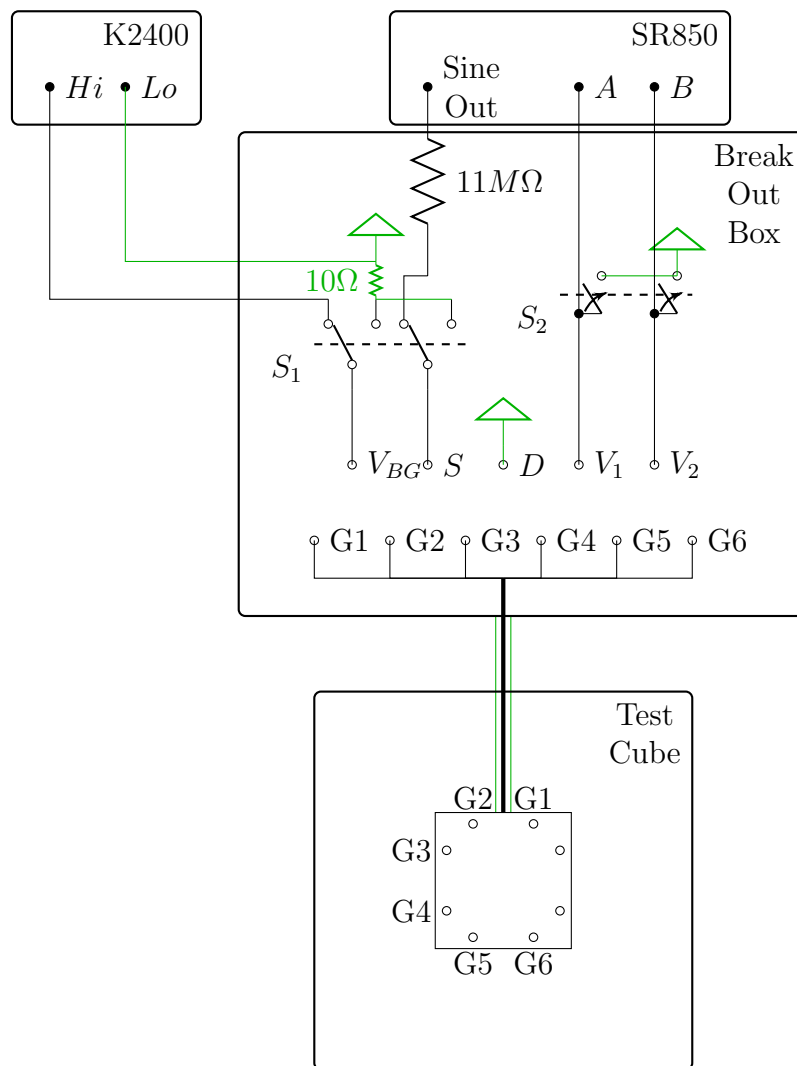
Figure F.2:   Circuit diagram of the electronics for measuring the phonon induced band gap in graphene. The diagram details the internal circuitry of the break out box which interfaces the Standford Research SR850 digital lock-in and the Keithley 2400 source meter with the graphene sample mounted in the test cube. The open V_{BG}, S, D, V_1, and V_2 contacts are bridged to the appropriate $G1 - G6$ contacts using BNC jumpers. Switches S_1 and S_2 are used to ground the sample contacts. The grounds, colored in green, are all referenced to the SR850 ground. Although not shown in the diagram, the core of all BNC cables are grounded on one side.

resistance is minimized using a large resister, $R_L = 11.130 M\Omega$, placed between the SR850 oscillator out and the source terminal as shown in Figure F.3. As long as the contact resistance is much less than R_L, the contact resistance can be ignored and the system can be treated as a voltage divider with the graphene resistance given by

$$R_g = R_L \frac{V_1 - V_2}{V_{AC} - (V_1 - V_2)} \pm R_L \left(\frac{V_{AC}}{(V_{AC} - (V_1 - V_2))^2} \right) \delta(V_1 - V_2) \ ,$$

where $V_{AC} = 1$ is the root mean squared AC voltage amplitude used in experiments and the term after the $\pm$ is the standard error which is proportional to the uncertainty in the measured voltage, $\delta(V_1 - V_2)$, determined by the standard deviation of > 10 sequentially measured values. The accuracy of this formula is limited if the resistance approaches the $10 M\Omega$ input impedance of the lock-in. When $R_g << R_L$ the useful approximation

$$R_g \approx (V_1 - V_2) * 10^4 \frac{\Omega}{mV} \ ,$$

holds. The added resistor is useful for other reasons. It limits the current through the graphene to a safe value of less than $100 nA$. Additionally, the large value of R_L ensures that the 50Ω output impedance of the lock-in is unimportant. The resistor R_L allows us to use lock-in techniques to increase our signal to noise.

To reduce noise in our measurements, we use the lock-in's internal oscillator as both the AC voltage source, V_{AC}, and as the reference to which the voltage measurements are mixed. To limit AC cross talk between lines the source is set to oscillate at the relatively low value of $f = 17 \ Hz$. To best limit any 1/f noise the rule of thumb is to set the time constant of the low pass filter to $\tau = 5\frac{1}{f} \approx 300ms$. However, we use $\tau = 100ms$ because it triples the measurement speed but does not substantially increase the noise. At each back gate voltage we takes 2 seconds worth of data sam-
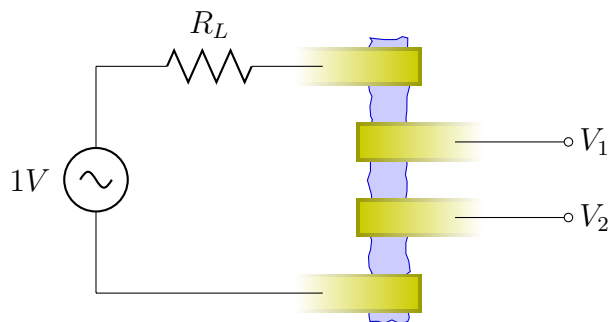
Figure F.3: Simplified circuit diagram of the four probe AC transport measurement.

pled at $f_S = 8Hz <= 1/\tau$ and record the average and standard deviation of these 16 data points. Between back gate voltages we wait for the low pass filter to respond by waiting for 10τ. The back gate capacitor is much faster than the low pass filter, fully charging in micro seconds. Noise is further reduced by measuring with the $60Hz$ and $120Hz$ line filters removed and the synchronous filter turned off. We use the 24 dB/octave low pass filter with a sufficiently large 36 dB dynamic reserve. The voltage is measured between the A and B lock-in terminals with their shells grounded. Using these techniques we achieve a sufficient signal to noise of 2000 to 1 for a resistance of $1k\Omega$.

The K2400 source meter is used as an ambipolar voltage source to control the back gate voltage. During measurement the back gate voltage is set by the Hi terminal. The outputted voltage is referenced to the floating Lo terminal that is in turn tied to ground in the breakout box. To limit electro magnetic interference (EMI) the Hi and Lo terminals are connected to the breakout box via separate BNC cables that have shields grounded on the breakout box side. Instrument noise is minimized by auto ranging the voltage. This keeps the voltage range as low as possible for each step in the back gate sweep. To protect the sample the current compliance is kept low and the software warns the user if it is reached. A value of 10 μA is low enough to

protect the sample but high enough that the current needed to charge the capacitor does not cause a warning. The current compliance being reached is an indicator of a leaky back gate. Finally to avoid SiO_2 breakdown the voltage in volts should be kept below the oxide thickness in nanometers. Applying these settings allows the K2400 to provide a safe and stable back gate voltage.

To protect the sample there are two double pull switches on the break out box which ground the sample. This is useful both when mounting the sample and for putting the system in a safe state during measurement downtime. The first switch, S_1, is a shorting rotary switch (NKK switches model number HS16-5SN-ND) which toggles the back gate and source terminals between measurement and ground modes. In measurement mode the terminals are connected to the measurement instruments while in ground mode the terminals are connected to ground through a 10Ω resistor. To make the transition between measurement and ground modes smoother for the sample, a shorting switch is used so that the second throw is made before the first throw is broken. For additional sample safety, the K2400 voltage and the sine out voltage on the SR850 should be set to zero to minimize the voltage change when switching. The small resistor between switch and ground limits the current flow between instrument and ground during the shorting action of the switch. Without this the small difference between the instrument voltages and ground can cause a large current flow to ground. The second switch, S_2, is a simple double pull single throw switch used to ground the V_1 and V_2 terminals. The A and B terminals on the SR850 are high impedance ($10M\Omega$) terminals and, as such, static charge could build up on these terminals and destroy the sample when it is connected. Closing S_2 grounds the terminals, dissipating any static charge. Used together these switches ground all of the pins on the sample.

Several precautions are made when mounting the sample. As mentioned earlier,

a grounding strap is always worn. During sample transport the pins are embedded in a conducting foam to keep all contacts at the same voltage. The sample is then removed from the foam for mounting in the presence of an ionizing fan. Before the sample is mounted switches S_1 and S_2 are set so that all the contacts are grounded. These precautions protect the sample from damage during mounting.

To limit EMI the shields on all of the BNCs are grounded on one side. They are only grounded on one side so as to avoid ground loops. In a perfect scenario the shield grounds would be isolated from the instrument ground. However, we do not have this capability. To further limit the EMI the length of the BNC cables is minimized. In fact the break out box is connected directly to the SR850. Finally, the metal break out box shields the passive electronics inside.

The measurement of the phonon induced band gap relies on the electronics detailed here. The electronics setup should maximize signal to noise while protecting the fragile graphene.

Bibliography

Ando, T. (2006). Anomaly of optical phonon in monolayer graphene. *Journal of the Physical Society of Japan*, 75(12):124701.

Balandin, A. A., Ghosh, S., Bao, W., Calizo, I., Teweldebrhan, D., Miao, F., and Lau, C. N. (2008). Superior thermal conductivity of single-layer graphene. *Nano Letters*, 8(3):902–907. PMID: 18284217.

Barton, R. A., Ilic, B., van der Zande, A. M., Whitney, W. S., McEuen, P. L., Parpia, J. M., and Craighead, H. G. (2011). High, size-dependent quality factor in an array of graphene mechanical resonators. *Nano Letters*, 11(3):1232–1236.

Bena, C. and Montambaux, G. (2009). Remarks on the tight-binding model of graphene. *New Journal of Physics*, 11(9):095003.

Berciaud, S., Li, X., Htoon, H., Brus, L. E., Doorn, S. K., and Heinz, T. F. (2013). Intrinsic line shape of the raman 2d-mode in freestanding graphene monolayers. *Nano Letters*, 13(8):3517–3523.

Blake, P., Hill, E. W., Neto, A. H. C., Novoselov, K. S., Jiang, D., Yang, R., Booth, T. J., and Geim, A. K. (2007). Making graphene visible. *Applied Physics Letters*, 91(6):063124.

Blakslee, O. L., Proctor, D. G., Seldin, E. J., Spence, G. B., and Weng, T. (1970). Elastic constants of compression-annealed pyrolytic graphite. *Journal of Applied Physics*, 41(8):3373–3382.

Bonaccorso, F., Sun, Z., Hasan, T., and Ferrari, A. (2010). Graphene photonics and optoelectronics. *Nature Photonics*, 4(9):611–622.

Bonini, N., Garg, J., and Marzari, N. (2012). Acoustic phonon lifetimes and thermal transport in free-standing and strained graphene. *Nano Letters*, 12(6):2673–2678.

Bonini, N., Lazzeri, M., Marzari, N., and Mauri, F. (2007). Phonon anharmonicities in graphite and graphene. *Physical Review Letters*, 99:176802.

Bunch, J. and Dunn, M. (2012). Adhesion mechanics of graphene membranes. *Solid State Communications*, 152(15):1359 – 1364. Exploring Graphene, Recent Research Advances.

Bunch, J. S., van der Zande, A. M., Verbridge, S. S., Frank, I. W., Tanenbaum, D. M., Parpia, J. M., Craighead, H. G., and McEuen, P. L. (2007). Electromechanical resonators from graphene sheets. *Science*, 315(5811):490–493.

Bunch, J. S., Verbridge, S. S., Alden, J. S., van der Zande, A. M., Parpia, J. M., Craighead, H. G., and McEuen, P. L. (2008). Impermeable atomic membranes from graphene sheets. *Nano Letters*, 8(8):2458–2462.

Cai, W., Moore, A. L., Zhu, Y., Li, X., Chen, S., Shi, L., and Ruoff, R. S. (2010). Thermal transport in suspended and supported monolayer graphene grown by chemical vapor deposition. *Nano Letters*, 10(5):1645–1651.

Calizo, I., Balandin, A. A., Bao, W., Miao, F., and Lau, C. N. (2007). Temperature dependence of the raman spectra of graphene and graphene multilayers. *Nano Letters*, 7(9):2645–2649.

Casiraghi, C., Hartschuh, A., Lidorikis, E., Qian, H., Harutyunyan, H., Gokus, T., Novoselov, K. S., and Ferrari, A. C. (2007). Rayleigh imaging of graphene and graphene layers. *Nano Letters*, 7(9):2711–2717.

Castro Neto, A. H., Guinea, F., Peres, N. M. R., Novoselov, K. S., and Geim, A. K. (2009). The electronic properties of graphene. *Reviews of Modern Physics*, 81:109–162.

Chamon, C., Hou, C.-Y., Iadecola, T., Jackiw, R., Kusminskiy, S. V., and Pi, S.-Y. (2013). Notes on rotating kekulé masses in graphene. Unpublished Notes.

Chen, C., Rosenblatt, S., Bolotin, K., Kalb, W., Kim, P., Kymissis, I., Stormer, H., Heinz, T., and Hone, J. (2009). Performance of monolayer graphene nanomechanical resonators with electrical readout. *Nature Nanotechnology*, 4(12):861–867.

Chen, S., Moore, A. L., Cai, W., Suk, J. W., An, J., Mishra, C., Amos, C., Magnuson, C. W., Kang, J., Shi, L., and Ruoff, R. S. (2011). Raman measurements of thermal transport in suspended monolayer graphene of variable sizes in vacuum and gaseous environments. *ACS Nano*, 5(1):321–328.

Chen, S., Wu, Q., Mishra, C., Kang, J., Zhang, H., Cho, K., Cai, W., Balandin, A. A., and Ruoff, R. S. (2012). Thermal conductivity of isotopically modified graphene. *Nature Materials*, 11(3):203–207.

Cheng, Y. C., Zhu, Z. Y., Huang, G. S., and Schwingenschlögl, U. (2011). Grüneisen parameter of the g mode of strained monolayer graphene. *Physical Review B*, 83:115449.

Choi, S.-M., Jhi, S.-H., and Son, Y.-W. (2010). Effects of strain on electronic properties of graphene. *Physical Review B*, 81:081407.

Clark, S., Jeon, K.-J., Chen, J.-Y., and Yoo, C.-S. (2013). Few-layer graphene under high pressure: Raman and x-ray diffraction studies. *Solid State Communications*, 154(0):15 – 18.

Cullen, W. G., Yamamoto, M., Burson, K. M., Chen, J. H., Jang, C., Li, L., Fuhrer, M. S., and Williams, E. D. (2010). High-fidelity conformation of graphene to sio$_2$ topographic features. *Physical Review Letters*, 105:215504.

Das Sarma, S., Adam, S., Hwang, E. H., and Rossi, E. (2011). Electronic transport in two-dimensional graphene. *Reviews of Modern Physics*, 83:407–470.

de Juan, F., Mañes, J. L., and Vozmediano, M. A. H. (2013). Gauge fields from strain in graphene. *Physical Review B*, 87:165131.

Dean, C., Young, A., Meric, I., Lee, C., Wang, L., Sorgenfrei, S., Watanabe, K., Taniguchi, T., Kim, P., Shepard, K., et al. (2010). Boron nitride substrates for high-quality graphene electronics. *Nature Nanotechnology*, 5(10):722–726.

Deng, Z., Smolyanitsky, A., Li, Q., Feng, X., and Cannara, R. (2012). Adhesion-dependent negative friction coefficient on chemically modified graphite at the nanoscale. *Nature Materials*, 11(12):1032–1037.

Dienwiebel, M., Verhoeven, G. S., Pradeep, N., Frenken, J. W. M., Heimberg, J. A., and Zandbergen, H. W. (2004). Superlubricity of graphite. *Physical Review Letters*, 92:126101.

Ding, F., Ji, H., Chen, Y., Herklotz, A., Dorr, K., Mei, Y., Rastelli, A., and Schmidt, O. G. (2010). Stretchable graphene: A close look at fundamental parameters through biaxial straining. *Nano Letters*, 10(9):3453–3458.

Everitt, K. F. and Skinner, J. L. (1999). Vibrational energy relaxation of oxygen in liquid mixtures with argon. *The Journal of Chemical Physics*, 110(9):4467–4470.

Faugeras, C., Amado, M., Kossacki, P., Orlita, M., Kühne, M., Nicolet, A. A. L., Latyshev, Y. I., and Potemski, M. (2011). Magneto-raman scattering of graphene on graphite: Electronic and phonon excitations. *Physical Review Letters*, 107:036807.

Faugeras, C., Amado, M., Kossacki, P., Orlita, M., Sprinkle, M., Berger, C., de Heer, W. A., and Potemski, M. (2009). Tuning the electron-phonon coupling in multi-layer graphene with magnetic fields. *Physical Review Letters*, 103:186803.

Faugeras, C., Faugeras, B., Orlita, M., Potemski, M., Nair, R. R., and Geim, A. K. (2010). Thermal conductivity of graphene in corbino membrane geometry. *ACS Nano*, 4(4):1889–1892. PMID: 20218666.

Ferrari, A. C., Meyer, J. C., Scardaci, V., Casiraghi, C., Lazzeri, M., Mauri, F., Piscanec, S., Jiang, D., Novoselov, K. S., Roth, S., and Geim, A. K. (2006). Raman spectrum of graphene and graphene layers. *Physical Review Letters*, 97:187401.

Fichter, W. (1997). Some solutions for the large deflections of uniformly loaded circular membranes. *NASA Technical Paper*, 3658.

Filleter, T. and Bennewitz, R. (2010). Structural and frictional properties of graphene films on sic(0001) studied by atomic force microscopy. *Physical Review B*, 81:155412.

Filleter, T., McChesney, J. L., Bostwick, A., Rotenberg, E., Emtsev, K. V., Seyller, T., Horn, K., and Bennewitz, R. (2009). Friction and dissipation in epitaxial graphene films. *Physical Review Letters*, 102:086102.

Fogler, M. M., Guinea, F., and Katsnelson, M. I. (2008). Pseudomagnetic fields and ballistic transport in a suspended graphene sheet. *Physical Review Letters*, 101:226804.

Frank, O., Tsoukleri, G., Parthenios, J., Papagelis, K., Riaz, I., Jalil, R., Novoselov, K. S., and Galiotis, C. (2010). Compression behavior of single-layer graphenes. *ACS Nano*, 4(6):3131–3138.

Ghosh, S., Bao, W., Nika, D. L., Subrina, S., Pokatilov, E. P., Lau, C. N., and Balandin, A. A. (2010). Dimensional crossover of thermal transport in few-layer graphene. *Nature Materials*, 9(7):555–558.

Goerbig, M. O. (2011). Electronic properties of graphene in a strong magnetic field. *Reviews of Modern Physics*, 83:1193–1243.

Gomes, K. K., Mar, W., Ko, W., Guinea, F., and Manoharan, H. C. (2012). Designer dirac fermions and topological phases in molecular graphene. *Nature*, 483(7389):306–310.

Goossens, A. M. (2013). *Confinement of charge carriers in bilayer graphene*. PhD thesis, Delft University of Technology.

Gottfried, K. and Yan, T.-M. (2003). *Quantum Mechanics: Fundamentals*. Springer, 2nd edition.

Guinea, F., Katsnelson, M. I., and Geim, A. K. (2010). Energy gaps and a zero-field quantum hall effect in graphene by strain engineering. *Nature Physics*, 6:30–33.

Hasegawa, Y., Konno, R., Nakano, H., and Kohmoto, M. (2006). Zero modes of tight-binding electrons on the honeycomb lattice. *Physical Review B*, 74:033413.

Hencky, H. (1915). On the stress state in circular plates with vanishing bending stiffness. *Zeitschrift für Mathematik und Physik*, 63(3):311–317.

Hou, C.-Y., Chamon, C., and Mudry, C. (2007). Electron fractionalization in two-dimensional graphenelike structures. *Physical Review Letters*, 98:186809.

Huang, M., Yan, H., Chen, C., Song, D., Heinz, T. F., and Hone, J. (2009). Phonon softening and crystallographic orientation of strained graphene studied by raman spectroscopy. *Proceedings of the National Academy of Sciences*, 106(18):7304–7308.

Hughes, T. J. R. (1987). *The Finite Element Method: Linear Static and Dynamic Finite Element Analysis.* Prentice-Hall.

Humphrey, W., Dalke, A., and Schulten, K. (1996). Vmd: Visual molecular dynamics. *Journal of Molecular Graphics*, 14(1):33 – 38.

Hunt, B., Sanchez-Yamagishi, J. D., Young, A. F., Yankowitz, M., LeRoy, B. J., Watanabe, K., Taniguchi, T., Moon, P., Koshino, M., Jarillo-Herrero, P., and Ashoori, R. C. (2013). Massive dirac fermions and hofstadter butterfly in a van der waals heterostructure. *Science*, 340(6139):1427–1430.

Iadecola, T., Campbell, D., Chamon, C., Hou, C.-Y., Jackiw, R., Pi, S-Y., and Kusminskiy, S. V. (2013a). Materials design from nonequilibrium steady states: Driven graphene as a tunable semiconductor with topological properties. *Physical Review Letters*, 110:176603.

Iadecola, T., Chamon, C., Jackiw, R., and Pi, S.-Y. (2013b). Generalized energy and time-translation invariance in a driven dissipative system. *Physical Review B*, 88:104302.

ichi Sasaki, K., Kawazoe, Y., and Saito, R. (2005). Local energy gap in deformed carbon nanotubes. *Progress of Theoretical Physics*, 113(3):463–480.

Jang, W., Chen, Z., Bao, W., Lau, C. N., and Dames, C. (2010). Thickness-dependent thermal conductivity of encased graphene and ultrathin graphite. *Nano Letters*, 10(10):3909–3913.

Jie, W., Hui, Y. Y., Zhang, Y., Lau, S. P., and Hao, J. (2013). Effects of controllable biaxial strain on the raman spectra of monolayer graphene prepared by chemical vapor deposition. *Applied Physics Letters*, 102(22):223112.

Kim, K.-J., Blanter, Y. M., and Ahn, K.-H. (2011). Interplay between real and pseudomagnetic field in graphene with strain. *Physical Review B*, 84:081401.

Kim, S. Y. and Park, H. S. (2009). Multilayer friction and attachment effects on energy dissipation in graphene nanoresonators. *Applied Physics Letters*, 94(10):101918.

Kim, Y., Poumirol, J. M., Lombardo, A., Kalugin, N. G., Georgiou, T., Kim, Y. J., Novoselov, K. S., Ferrari, A. C., Kono, J., Kashuba, O., Fal'ko, V. I., and Smirnov, D. (2013). Measurement of filling-factor-dependent magnetophonon resonances in graphene using raman spectroscopy. *Physical Review Letters*, 110:227402.

Kitt, A. L., Pereira, V. M., Swan, A. K., and Goldberg, B. B. (2012). Lattice-corrected strain-induced vector potentials in graphene. *Physical Review B*, 85:115432.

Kitt, A. L., Pereira, V. M., Swan, A. K., and Goldberg, B. B. (2013a). Erratum: Lattice-corrected strain-induced vector potentials in graphene [phys. rev. b 85, 115432 (2012)]. *Physical Review B*, 87:159909.

Kitt, A. L., Qi, Z., Rémi, S., Park, H. S., Swan, A. K., and Goldberg, B. B. (2013b). How graphene slides: Measurement and theory of strain-dependent frictional forces between graphene and sio2. *Nano Letters*, 13(6):2605–2610.

Kittel, C. (2005). *Introduction to Solid State Physics*. John Wiley and Sons, Inc, 8th edition.

Klemens, P. (2001). Theory of thermal conduction in thin ceramic films. *International Journal of Thermophysics*, 22(1):265–275.

Koenig, S., Boddeti, N., Dunn, M., and Bunch, J. (2011). Ultrastrong adhesion of graphene membranes. *Nature Nanotechnology*, 6(9):543–546.

Krim, J. (1996). Atomic-scale origins of friction. *Langmuir*, 12(19):4564–4566.

Lammps (2012).

Landau, L. and Lifshitz, E. (1986). *Theory of Elasticity*. Butterworth Heinemann, Oxford, 3rd edition.

Lee, C., Li, Q., Kalb, W., Liu, X.-Z., Berger, H., Carpick, R. W., and Hone, J. (2010). Frictional characteristics of atomically thin sheets. *Science*, 328(5974):76–80.

Lee, C., Wei, X., Kysar, J. W., and Hone, J. (2008). Measurement of the elastic properties and intrinsic strength of monolayer graphene. *Science*, 321(5887):385–388.

Lee, J.-U., Yoon, D., and Cheong, H. (2012). Estimation of youngs modulus of graphene by raman spectroscopy. *Nano Letters*, 12(9):4444–4448.

Lee, J.-U., Yoon, D., Kim, H., Lee, S. W., and Cheong, H. (2011). Thermal conductivity of suspended pristine graphene measured by raman spectroscopy. *Physical Review B*, 83:081419.

Levy, N., Burke, S. A., Meaker, K. L., Panlasigui, M., Zettl, A., Guinea, F., Neto, A. H. C., and Crommie, M. F. (2010). Strain-induced pseudomagnetic fields greater than 300 tesla in graphene nanobubbles. *Science*, 329(5991):544–547.

Li, A. H.-T., Chao, S. D., and Chang, C.-C. (2010a). Determination of a silane intermolecular force field potential model from an *ab initio* calculation. *Physical Review A*, 82:062520.

Li, Q., Lee, C., Carpick, R. W., and Hone, J. (2010b). Substrate effect on thickness-dependent friction on graphene. *Physica Status Solidi (b)*, 247(11-12):2909–2914.

Lindsay, L., Broido, D. A., and Mingo, N. (2010). Flexural phonons and thermal transport in graphene. *Physical Review B*, 82:115427.

Lindsay, L., Broido, D. A., and Mingo, N. (2011). Flexural phonons and thermal transport in multilayer graphene and graphite. *Physical Review B*, 83:235428.

Lui, C., Liu, L., Mak, K., Flynn, G., and Heinz, T. (2009). Ultraflat graphene. *Nature*, 462(7271):339–341.

Mañes, J. L. (2007). Symmetry-based approach to electron-phonon interactions in graphene. *Physical Review B*, 76:045430.

Mak, K. F., Lui, C. H., and Heinz, T. F. (2010). Measurement of the thermal conductance of the graphene/sio2 interface. *Applied Physics Letters*, 97(22):–.

Malard, L. M., Nilsson, J., Elias, D. C., Brant, J. C., Plentz, F., Alves, E. S., Castro Neto, A. H., and Pimenta, M. A. (2007). Probing the electronic structure of bilayer graphene by raman scattering. *Physical Review B*, 76:201401.

May, J. W. (1969). Platinum surface {LEED} rings. *Surface Science*, 17(1):267 – 270.

Meinel, A. B. and Meinel, M. P. (2000). Inflatable membrane mirrors for optical passband imagery. *Optical Engineering*, 39(2):541–550.

Metzger, C., Rémi, S., Liu, M., Kusminskiy, S. V., Castro Neto, A. H., Swan, A. K., and Goldberg, B. B. (2010). Biaxial strain in graphene adhered to shallow depressions. *Nano Letters*, 10(1):6–10.

Milaninia, K. M., Baldo, M. A., Reina, A., and Kong, J. (2009). All graphene electromechanical switch fabricated by chemical vapor deposition. *Applied Physics Letters*, 95(18):183105.

Mohiuddin, T. M. G., Lombardo, A., Nair, R. R., Bonetti, A., Savini, G., Jalil, R., Bonini, N., Basko, D. M., Galiotis, C., Marzari, N., Novoselov, K. S., Geim, A. K., and Ferrari, A. C. (2009). Uniaxial strain in graphene by raman spectroscopy: g peak splitting, grüneisen parameters, and sample orientation. *Physical Review B*, 79:205433.

Ni, Z. H., Yu, T., Lu, Y. H., Wang, Y. Y., Feng, Y. P., and Shen, Z. X. (2008). Uniaxial strain on graphene: Raman spectroscopy study and band-gap opening. *ACS Nano*, 2(11):2301–2305.

Nicolle, J., Machon, D., Poncharal, P., Pierre-Louis, O., and San-Miguel, A. (2011). Pressure-mediated doping in graphene. *Nano Letters*, 11(9):3564–3568.

Novoselov, K., Geim, A. K., Morozov, S., Jiang, D., Grigorieva, M. K. I., Dubonos, S., and Firsov, A. (2005). Two-dimensional gas of massless dirac fermions in graphene. *Nature*, 438(7065):197–200.

Novoselov, K. S., Geim, A. K., Morozov, S. V., Jiang, D., Zhang, Y., Dubonos, S. V., Grigorieva, I. V., and Firsov, A. A. (2004). Electric field effect in atomically thin carbon films. *Science*, 306(5696):666–669.

Ong, Z.-Y. and Pop, E. (2010). Molecular dynamics simulation of thermal boundary conductance between carbon nanotubes and sio$_2$. *Physical Review B*, 81:155408.

Palik, E. and Ward, L. (1991). Handbook of optical constants of solids ii. *Elsevier Science*, 2:519–529.

Palik, E. D. (1985). *Handbook of Optical Constants of Solids*. Academic Press, Orlando, Florida.

Pellegrino, F. M. D., Angilella, G. G. N., and Pucci, R. (2010). Strain effect on the optical conductivity of graphene. *Physical Review B*, 81:035411.

Pereira, L. F. C. and Donadio, D. (2013). Divergence of the thermal conductivity in uniaxially strained graphene. *Physical Review B*, 87:125424.

Pereira, V. M. and Castro Neto, A. H. (2009). Strain engineering of graphene's electronic structure. *Physical Review Letters*, 103:046801.

Pereira, V. M., Castro Neto, A. H., and Peres, N. M. R. (2009). Tight-binding approach to uniaxial strain in graphene. *Physical Review B*, 80:045401.

Pereira, V. M., Ribeiro, R. M., Peres, N. M. R., and Neto, A. H. C. (2010). Optical properties of strained graphene. *Europhysics Letters*, 92(6):67001.

Plimpton, S. (1995). Fast parallel algorithms for short-range molecular dynamics. *Journal of Computational Physics*, 117(1):1 – 19.

Press, W. H., Teukolsky, S. A., Vetterling, W. T., and Flannery, B. P. (2007). *Numerical Recipes 3rd Edition: The Art of Scientific Computing.* Cambridge University Press, Cambridge.

Proctor, J. E., Gregoryanz, E., Novoselov, K. S., Lotya, M., Coleman, J. N., and Halsall, M. P. (2009). High-pressure raman spectroscopy of graphene. *Physical Review B*, 80:073408.

Pumarol, M. E., Rosamond, M. C., Tovee, P., Petty, M. C., Zeze, D. A., Falko, V., and Kolosov, O. V. (2012). Direct nanoscale imaging of ballistic and diffusive thermal transport in graphene nanostructures. *Nano Letters*, 12(6):2906–2911.

Qi, Z., Zhao, F., Zhou, X., Sun, Z., Park, H. S., and Wu, H. (2010). A molecular simulation analysis of producing monatomic carbon chains by stretching ultranarrow graphene nanoribbons. *Nanotechnology*, 21(26):265702.

Rémi, S. (2014). *Measurement and control of electron phonon interactions in graphene.* PhD thesis, Boston University.

Resnick, R., Halliday, D., and Krane, K. (2002). *Physics.* John Wiley & Sons, inc., New York, 5 edition.

Ribeiro, R. M., Pereira, V. M., Peres, N. M. R., Briddon, P. R., and Neto, A. H. C. (2009). Strained graphene: tight-binding and density functional calculations. *New Journal of Physics*, 11(11):115002.

Rytkonen, A., Valkealahti, S., and Manninen, M. (1998). Phase diagram of argon clusters. *The Journal of Chemical Physics*, 108(14):5826–5833.

Semenoff, G. W. (1984). Condensed-matter simulation of a three-dimensional anomaly. *Physical Review Letters*, 53:2449–2452.

Seol, J. H., Jo, I., Moore, A. L., Lindsay, L., Aitken, Z. H., Pettes, M. T., Li, X., Yao, Z., Huang, R., Broido, D., Mingo, N., Ruoff, R. S., and Shi, L. (2010). Two-dimensional phonon transport in supported graphene. *Science*, 328(5975):213–216.

Sloan, J. V., Sanjuan, A. A. P., Wang, Z., Horvath, C., and Barraza-Lopez, S. (2013). Strain gauge fields for rippled graphene membranes under central mechanical load: An approach beyond first-order continuum elasticity. *Physical Review B*, 87:155436.

Stolyarova, E., Rim, K. T., Ryu, S., Maultzsch, J., Kim, P., Brus, L. E., Heinz, T. F., Hybertsen, M. S., and Flynn, G. W. (2007). High-resolution scanning tunneling microscopy imaging of mesoscopic graphene sheets on an insulating surface. *Proceedings of the National Academy of Sciences*, 104(22):9209–9212.

Stuart, S. J., Tutein, A. B., and Harrison, J. A. (2000). A reactive potential for hydrocarbons with intermolecular interactions. *The Journal of Chemical Physics*, 112(14):6472–6486.

Tersoff, J. (1988). New empirical approach for the structure and energy of covalent systems. *Physical Review B*, 37:6991–7000.

Thomsen, C., Reich, S., and Ordejón, P. (2002). *Ab initio* determination of the phonon deformation potentials of graphene. *Physical Review B*, 65:073403.

Timoshenko, S. P. and Woinowsky-Krieger, S. (1959). *Theory of Plates and Shells*. McGraw-Hill Book Company, inc, 3rd edition.

Tsoukleri, G., Parthenios, J., Papagelis, K., Jalil, R., Ferrari, A. C., Geim, A. K., Novoselov, K. S., and Galiotis, C. (2009). Subjecting a graphene monolayer to tension and compression. *Small*, 5(21):2397–2402.

Tuinstra, F. and Koenig, J. L. (1970). Raman spectrum of graphite. *The Journal of Chemical Physics*, 53(3):1126–1130.

Tuzun, R. E., Noid, D. W., Sumpter, B. G., and Merkle, R. C. (1996). Dynamics of fluid flow inside carbon nanotubes. *Nanotechnology*, 7(3):241.

Vozmediano, M., Katsnelson, M., and Guinea, F. (2010). Gauge fields in graphene. *Physics Reports*, 496(45):109 – 148.

Wallace, P. R. (1947). The band theory of graphite. *Physical Review*, 71:622–634.

Web of Sciecne (2013). Web of knowledge.

Yan, H., Sun, Y., He, L., Nie, J.-C., and Chan, M. H. W. (2012). Observation of landau-level-like quantization at 77 k along a strained-induced graphene ridge. *Physical Review B*, 85:035422.

Yeh, N.-C., Teague, M.-L., Yeom, S., Standley, B., Wu, R.-P., Boyd, D., and Bockrath, M. (2011). Strain-induced pseudo-magnetic fields and charging effects on cvd-grown graphene. *Surface Science*, 605(1718):1649 – 1656. ¡ce:title¿Graphene Surfaces and Interfaces¡/ce:title¿.

Yoon, D., Son, Y.-W., and Cheong, H. (2011). Strain-dependent splitting of the double-resonance raman scattering band in graphene. *Physical Review Letters*, 106:155502.

Young, A. F. and Kim, P. (2009). Quantum interference and klein tunnelling in graphene heterojunctions. *Nature Physics*, 5(3):222–226.

Yu, T., Ni, Z., Du, C., You, Y., Wang, Y., and Shen, Z. (2008). Raman mapping investigation of graphene on transparent flexible substrate: The strain effect. *The Journal of Physical Chemistry C*, 112(33):12602–12605.

Zabel, J., Nair, R. R., Ott, A., Georgiou, T., Geim, A. K., Novoselov, K. S., and Casiraghi, C. (2012). Raman spectroscopy of graphene and bilayer under biaxial strain: Bubbles and balloons. *Nano Letters*, 12(2):617–621.

Zhang, J., Lu, W., Tour, J. M., and Lou, J. (2012). Nanoscale frictional characteristics of graphene nanoribbons. *Applied Physics Letters*, 101(12):123104.

Zhang, Y., Tan, Y.-W., Stormer, H. L., and Kim, P. (2005). Experimental observation of the quantum hall effect and berry's phase in graphene. *Nature*, 438(7065):201–204.

Zhang, Y., Tang, T.-T., Girit, C., Hao, Z., Martin, M. C., Zettl, A., Crommie, M. F., Shen, Y. R., and Wang, F. (2009). Direct observation of a widely tunable bandgap in bilayer graphene. *Nature*, 459(7248):820–823.

Zhang, Y. and Wang, W. (2011). Analytical model of electrostatic actuators for micro gas pumps. *Microsystem Technologies*, 17:1683–1696.

Zhao, H. and Aluru, N. R. (2010). Temperature and strain-rate dependent fracture strength of graphene. *Journal of Applied Physics*, 108(6):064321.

Zimmerman, J. A., Bammann, D. J., and Gao, H. (2009). Deformation gradients for continuum mechanical analysis of atomistic simulations. *International Journal of Solids and Structures*, 46(2):238 – 253.

Zomer, P. J., Dash, S. P., Tombros, N., and van Wees, B. J. (2011). A transfer technique for high mobility graphene devices on commercially available hexagonal boron nitride. *Applied Physics Letters*, 99(23):232104.

Curriculum Vitae

Alexander Kitt

Department of Physics   (585) 737-3493

Boston University   alexander.kitt@gmail.com

590 Commonwealth Avenue

Boston, MA 02215

Education:

Boston University, Boston MA   2008-2014

PhD in Physics 1/2014

Advisors: Bennett B Goldberg and Anna Swan

Thesis: Manipulating graphene's lattice to create pseudovector potentials, discover anomalous friction, and measure strain dependent thermal conductivity

SUNY at Buffalo, Buffalo NY   2004-2008

B.S. in Physics, B.A. in Mathematics, Minor in Philosophy of Science

Honors Scholar, Renaissance Scholar, *summa cum laude*

Skills:

Experimental Techniques:

Raman Spectroscopy, Electrical transport, AFM, SEM, Photolithography, RIE, DRIE, E-beam and thermal evaporation, Ellipsometry, Thermal oxide growth

Programming Languages/Software:

Matlab, Mathematica, IDL, C++, Python, Labview, Comsol Multiphysics FEA, CAD

Lab/Hardware skills:

Microscope fabrication and optical design, Laser alignment, Vacuum equipment, Machining

Experience:

Boston University: Graphene   2009-2014

Experiment: First measurement of graphene's anomalous macroscopic sliding friction.

Theory: Derived corrections to the strain-induced pseudovector potential in graphene.

Apparatus design: Integrated an electrical transport assay into a UHV Helium scattering facility, designed and built both a high pressure Raman microscope and a low pressure CVD furnace.

Device: Demonstrated proof of concept for graphene based threshold pressure sensor for remote oil well application.

Mentoring: Mentored 4 undergraduate students.

Undergraduate Thesis: Astro-physics Simulations   2007-2008

To give insight into early galaxy formation, wrote a scalable program to simulate an interacting luminous and dark matter gas.

University of Rochester: Infrared Astronomy   Summer 2006 and 2008

Found preliminary evidence of extremely small silicates in the interstellar medium.

University of Colorado at Boulder   Summer 2007

Tested alternate methods for graphene exfoliation.

Publications:

AL Kitt, Z Qi, S Rèmi, H.S. Park, A.K. Swan, BB Goldberg
"How graphene slides: Measurement and theory of strain-dependent frictional forces between graphene and SiO_2"
Nano Letters **13** 2605 (2013)

AL Kitt, V.M. Pereira, A.K. Swan, BB Goldberg
"Lattice-corrected strain-induced vector potentials in graphene"
Physical Review B **85** 115432 (2012)

J.W. Suk, AL Kitt, C.W. Magnuson, Y. Hao, S. Ahmed, J. An, A.K. Swan, BB Goldberg, R.S. Ruoff
"Transfer of CVD-Grown Monolayer Graphene onto Arbitrary Substrates"
ACS Nano **5** 6916 (2011)

Presentations:

"Graphene's anomalous strain dependent sliding friction"
Colloquium at SUNY Buffalo   2/2014

"Graphene's anomalous strain dependent sliding friction"
Seminar at the University of Rochester   12/2013

"Graphene slides over the substrate when you pull it: Direct measurement, theory and frictional forces"
Talk at American Physical Society March Meeting   3/2013

"How graphene slides: Measurement and theory of frictional forces between graphene and SiO_2"
Talk at Boston Area Carbon Nanoscience   3/2013

"The correct solution for (in plane) strain-induced pseudo vector potentials in graphene"
Talk at American Physical Society March Meeting   3/2012

"Corrections to pseudo vector potentials and their effect on pseudo magnetic fields"
Talk at Boston Area Carbon Nanoscience   2/2012

"Complete solution for strain-induced pseudo vector potentials in graphene"
Poster at Materials Research Society Fall Meeting   12/2011

"Variable strain in graphene sealed microchambers studied with Raman spectroscopy"
Talk at American Physical Society March Meeting   3/2011

"Raman spectroscopy of suspended mono and bilayer graphene"
Talk at American Physical Society March Meeting   3/2010